A System of Mapping Historical Wildfire Events

in the Boreal Forest using Polarimetric Radar

By

Geordie Hobart

A Thesis submitted in Partial Fulfillment of a
of the Requirements for the Degree of
MASTER OF SCIENCE
in the Department of Computer Science

A System of Mapping Historical Wildfire Events

in the Boreal Forest using Polarimetric Radar

By

Geordie Hobart

BEng, University of Victoria 2004

Supervisory Committee

Dr. David G. Goodenough, (Department of Computer Science)
Supervisor

Dr. Wendy Myrvold, (Department of Computer Science)
Co-Supervisor

Dr. K. Olaf Niemann, (Department of Geography)
Outside Member

Supervisory Committee

Dr. David G. Goodenough, (Department of Computer Science)
Supervisor

Dr. Wendy Myrvold, (Department of Computer Science)
Co-Supervisor

Dr. K. Olaf Niemann, (Department of Geography)
Outside Member

Abstract

The boreal forest covers 11% of the earth's land surface and contains 37 percent of the planet's terrestrial carbon, which is more than the combined total of both the tropical and the temperate forests [1]. This estimate translates to 703 Pg of carbon with the vast majority contained within the organic soils and peat layers [2-4]. The western-north American boreal forest is a fire ecosystem [2, 5-7] where fires typically occur every 50 to 200 years [8, 9], allowing vast quantities of carbon to re-enter the atmosphere. Understanding and estimating past fire history and the related changes in carbon budget [3, 4, 7, 10] in this biome is of significant importance for climate researchers as they attempt to model for future changes in the planet's climate [2, 4, 11-14].

Many techniques are available to remotely sense wildfires - using optical, thermal and passive microwave remote sensors - during and immediately after an event - although resolution and availability of images due to cloud cover can make these techniques operationally challenging. Radar remote sensing can provide a complement to these optical and passive microwave

techniques, since radar is not affected by cloud cover and solar illumination levels. The Advanced Land Observatory Satellite (ALOS) operates a phased array L band synthetic aperture radar (PALSAR) and Canada's Radarsat-2 contains a C-Band (SAR) instrument. These radar satellites can be used to detect information about the boreal forest environment including the effects of wildfire. Polarimetric radar is an emerging technology whose full potential is still being actively explored and discovered. More specifically, this research is ground-breaking since very little work has been performed investigating the relationship between polarimetric radar data and historical boreal wildfire events. This area of investigation is a complex marriage of forestry, geospatial information and radar engineering that requires an extensive array of data sets to facilitate analysis.

This research has demonstrated that both PALSAR L-Band and Canada's Radarsat-2 C-Band full polarimetric radars can be used to detect and classify wildfire scars within individual images. The boreal forest is a dynamic ecosystem where both the level of burn severity and the subsequent regeneration of the forest is affected by many factors that can vary widely across small distances. This work contributes to the understanding of the relationships between remotely sensed quad-pol radar signals and both the boreal ecosystem and how wildfire interacts in this environment.

Table of Contents

Supervisory Committee ii
Abstract iii
Table of Contents v
List of Figures ix
List of Tables xi
Glossary xii
Acknowledgments xv
Dedication xvi
1.0 Introduction 1
2.0 Study Area and Data Sets 8
2.1 Polarimetric Data Sets 9
2.2 Federal, Provincial, and Territorial GIS Fire Data Sets 10
2.3 NFDB National Fire Database 11
2.4 Landsat 4, Landsat 5 and Landsat 7Optical Imagery and Burn Indexes 11
2. 5 Parks Canada Ground Survey Data for Wood Buffalo National Park 12
2.6 NTDB Digital Elevation Model 13
3.0 Methods and Analysis Theory 14
3.1 Radar Introduction 14
3.2 Radar Polarimetry 16
3.2.1 Poincare sphere 20
3.2.2 Stokes Vector g 21
3.3 Full Polarimetric Radar Characterizations 22
3.3.1 Sinclair Scattering Matrix 22
3.3.2 Mueller matrix 23
3.3.3 Kennaugh matrix 24
3.3.4 Relationship between the Mueller and Sinclair Matrix 25
3.3.5 Scattering Target Vectors 25
3.3.5.1 Lexicographic Vector Representation of Scattering 26
3.3.5.2 Pauli Vector Representation of Scattering 26
3.3.6 The Covariance Matrix C 27
3.3.7 Coherency Matrix T 28

3.3.8 Other Representations of the Coherency and Covariance Matrices 28
3.3.9 SPAN of SAR Data 29
3.4 Pre-processing and Transformations of PolSAR Radar Data 30
3.4.1 Faraday Rotation 30
3.4.2 Terrain Induced Orientation Angle Correction 31
3.4.3 Speckle Filtering 33
3.4.4 Multi-look Average Processing 33
3.4.5 Boxcar Speckle Filter 34
3.4.6 Enhanced Lee Speckle Filter 34
3.4.7 Noise Coherence Averaging 34
3.4.8 Decompositions 35
3.4.9 Eigen-based decompositions 37
3.4.9.1 Entropy (H) Decomposition Parameter 39
3.4.9.2 Alpha (α) Parameter 39
3.4.9.3 Anisotropy 40
3.4.9.4 Single (and Double) Bounce eigenvalue Relative Difference (SERD and DERD) 40
3.4.9.5 Shannon Entropy 41
3.4.9.6 Polarization Fraction 41
3.4.9.7 Polarization Asymmetry 41
3.4.9.8 Radar Vegetation Index 42
3.4.9.9 Pseudo Probabilities (P_1, P_2, P_3) 42
3.4.9.10 Pedestal Height 42
3.4.9.11 Beta (β), Delta ($\boldsymbol{\delta}$), Gamma($\boldsymbol{\gamma}$) 42
3.4.9.11 Epsilon (ε) and Nu ($\boldsymbol{\nu}$) Decomposition Parameters 43
3.4.9.12 Combinations of Entropy(H) and Anisotropy(A) 44
3.4.9.13 Luneburg Anisotropy 45
3.5 Geolocation and Orthorectification 45
3.6 Visualizations 47
3.6.1 Alpha, Entropy, Lambda as Hue, Saturation, and Value 47
3.6.2 Pauli Visualization 47
3.6.3 Freeman-Durden Image Visualization 48
3.6.4 Entropy-Alpha Plane 48
4.0 Computer Systems, Data Flow and Software Environment 50

4.1 Introduction 50
4.2 Software 51
4.3 Image Acquisition Process 56
4.4 PALSAR Pre-processing 58
4.5 Sample Selection 61
4.6 Analysis, Classification, and Modeling Methodology 63
5 Methodology and Analysis Results 67
5.1 PALSAR Scene Acquisition 67
5.1.1 Weather conditions for PALSAR Scene Acquisitions 69
5.1.2 Terrestrial Ecoregions and Ecozones for PALSAR Scene Acquisitions 71
5.2 Analysis 72
5.2.1 Observed Composite Burn Index and PALSAR Decomposition Parameters 72
5.2.2 Temporal Stability between Acquisition Dates 75
5.2.3 Entropy/Alpha and Entropy/Anisotropy graphs of selected Forest types in PALSAR Quad-pol Image June 6, 2009 76
5.2.2 PALSAR Quad-pol Image March 25, 2009 78
5.2.3 PALSAR Quad-pol Image May 15, 2009 – South 80
5.2.4 PALSAR Quad-pol Image May 15, 2009 – North 82
5.2.5 PALSAR Quad-pol Image June 8, 2009 84
5.2.6 Summary analysis of the Selected PALSAR images 85
5.3 Parametric and Non-parametric Classifications 86
5.3.1 June 6, 2009 PALSAR Classification Results 88
5.3.2 June 8, 2009 PALSAR Classification Results 91
5.3.3 May 15, 2009 South PALSAR Classification Results 93
5.3.4 May 15, 2009 North PALSAR Classification Results 95
5.3.5 May 15, 2009 North PALSAR Classification Results Using An Expanded Set of Input Parameters 96
5.3.6 May 15, 2009 South PALSAR Classification Results Using An Expanded Set of Input Parameters 98
5.4 Radarsat-2 C-Band For Wildfire Detection 100
5.4.1 Temporal Analysis over the 2006 Keg River Wildfire 100
5.4.2 Parametric Classification of Radarsat-2 for 2002 Keg River Wildfire 102
6 Discussion and Conclusion 105
7 Future Work 109

8 References 111

Appendix A. CBI Fire Survey Worksheet 119

Appendix B. Radar_correction.m 120

Appendix C. do_dnbr_ca.pro 126

Appendix D. build_burn_mask.pro 129

Appendix E. Environment Canada Weather Data from Nearby Stations 132

Appendix F. Results of linear regression for various Polarimetric SAR parameters versus field measured Composite Burn Index (CBI) 134

Appendix G. Temporal comparison of Overlapping PALSAR decomposition parameters between June 8 and April 6 images acquired in 2009. 137

Appendix H. Maximum Likelihood Classification results for June 6, 2009 PALSAR image. 141

Appendix I. LOGIT Classification results for June 6, 2009 PALSAR image. 143

Appendix J. MLC and LOGIT results for June 8, 2009 PALSAR image. 145

Appendix K. MLC and LOGIT results for May 15, 2009 South PALSAR image 149

Appendix L. MLC and LOGIT results for May 15, 2009 North PALSAR image 152

Appendix M. PALSAR May15 North Classification Results for 4 Fire Classes 156

Appendix N. PALSAR May15 North Classification Results for 2 Fire Classes with Additional Input Channels 159

Appendix O. PALSAR May15 North Classification Results for 3 Fire Classes with Additional Input Channels 162

Appendix P. PALSAR May 15 South Classification Results for 4 Fire Classes 164

Appendix Q. Radarsat-2 Sept. 22 Classification Results 168

List of Figures

Figure 1 - Canadian boreal forest extent overlaid on 2009 Landsat 5/7 composite image. 1

Figure 2 - Boreal wildfires greater than 200 ha between 2000 and 2011..... 2

Figure 3 - Comparative images for 2002 Keg River Fir. A) RGB (Bands 543)2002 Landsat image immediately after fire, B) dNBR image generated from 2 Landsat images pre and post fire, C) Alpha, Entropy, Lambda 2009 PALSAR decomposition as Hue, Saturation ,Value image, and D) 2009 RGB (Bands 543) Landsat image with fire scar barely visible 6 years after the event. 4

Figure 4 - PAULI decomposition of C-Band Polarimetric radar collected over Hinton Alberta with crescent shaped 50 year old fire scar visible on the right hand side of the image..... 5

Figure 5 - Study Area centered on Chinchaga wildfire with PALSAR image footprints..... 8

Figure 6 - Example of chirped radar pulse where both the phase and amplitude vary with time 15

Figure 7 - Linear polarized electromagnetic plane wave and reference frame basis 17

Figure 8 - Geometry of an incident electromagnetic wave and the resultant scattered wave after encountering a target[42](p46)..... 18

Figure 9 - Example of polar co-ordinate system for vector r 19

Figure 10 - Poincare sphere for visualization of polarized electromagnetic waves. 20

Figure 11 - PALSAR Blue Sheep Creek Alpha, Entropy, Lambda2&3 HSV decomposition image that has been geolocated on left while the image on the right displays the same image with a red shadow /layover mask in overlaid. All of the data under the mask must be excluded from analyses. 46

Figure 12 - Entropy-Alpha Plane Graph of Mature Forest. Each of 8 feasible regions in the plane represent a different type of scattering target allowing for a physical interpretation of the target's physical characteristics. 48

Figure 13 - Radar Image Acquisition Process 57

Figure 14 - Sample Point Selection..... 62

Figure 15 - Geolocated PALSAR Alpha, Entropy, Alpha HSV image acquired on May 15, 2009. The image has been generated using a Hue, Saturation, Value colour mapping respectively to Entropy, Alpha(1) and Lambda 2 plus 3 decomposition parameters of the Cloude-Pottier Entropy –Alpha decomposition. Sample points used for analysis are denoted in red. Alberta fire polygons are overlaid on the image. 64

The Figure 16 - Analysis Phase Process Steps 65

Figure 17 - Classification Process Flow to Create Fire Scar Map..... 66

Figure 18 - PALSAR study images – The numbers complement the ID values from Table 7. The closest weather stations to the acquired scenes are also noted in this figure. 69

Figure 19 - PALSAR study images – The numbers compliment the ID values from Table 4. The closest weather stations to the acquired scenes are also noted in this figure. 70

Figure 20 - Three main Ecozones within the study area. The Ecozones are denoted by the red borders. 71

Figure 21 - Hue Saturation Value (HSV) image of Alpha, Entropy, Lambda2&3 (AHL) decomposition image of PALSAR June, 5, 2009 over Wood Buffalo National Park with sample plots from field measurements with accompanying images 74

Figure 22 - Landsat optical image immediately after 2006 BC Wildfire G80381. Entropy-Anisotropy, and Entropy-Alpha diagrams of 2006 BC Wildfire G80381 and surrounding forested and harvested areas. The scale for H and A is zero to one and zero to ninety degrees for alpha.77

Figure 23 - HSV of Alpha, Entropy and Lambda of PALSAR image for March 25, 2009 79

Figure 24 - HSV- Alpha, Entropy, Lambda PALSAR decomposition image acquired May 15, 2009 with Sample plots 81

Figure 25 - HSV- Alpha, Entropy, Lambda PALSAR decomposition image acquired May 15, 2009 with Sample plots 83

Figure 26 - HSV Alpha, Entropy Lambda Image of PALSAR June 8th, 2009 acquistion 84

Figure 27 - Maximum Likelihood Classification results of June 6, 2009 PALSAR image. Optical image on the left for reference and the classification image on the right 88

Figure 28 - LOGIT classification of Alpha entropy and the radar vegetation index for the June 6, 2009 PALSAR image 90

Figure 29 - MLC result for Alpha, Entropy, RVI, and Luneburg Anisotropy for June 8th PALSAR Image 92

Figure 30 - LOGIT result with Alpha, Entropy, Luneburg Anisotropy for June 8 PALSAR image ... 93

Figure 31 - Landsat BAP and MLC result of PALSAR May 15 south Image using Alpha, Entropy, and RVI 94

Figure 32 - MLC results for Alpha, Pedestal Height, Polarization Fraction, and RCS Max for 4 Different Wildfire Events for May 15th North PALSAR image 97

Figure 33 - MLC results for Alpha, Pedestal Height, Polarization Fraction, and RCS Max for 4 Different Wildfire Events for May 15th South PALSAR image 99

Figure 34 - 2013 Temporal Series of Radarsat-2 images over the 2006 Keg River Fire. All images were created as HSV of Alpha, Entropy, Lambda decompositions. 101

Figure 35 - Graphs of Temporal variation of Radarsat six images for Anisotropy, Entropy, and Alpha for sample area within the Keg River wildfire and nearby Forest 101

Figure 36 - September 22, 2013 RS2 MLC image and confusion Matrix using Alpha, Entropy, Luneburg Anisotropy, and Lambda2+3 input channels 103

List of Tables

Table 1 - Summary of the most common radar microwave bands and their physical characteristics..... 10

Table 2 - Summary of Interpreted dNBR values..... 12

Table 3 - Stokes parameters.. I stands for the real valued measured intensity of the signal. The degrees stated in the I() function represent the orientation of the antenna. RCP and LCP stand for right and left circular polarization. The phase constant δ is equal to δ_x - δ_y 21

Table 4 - Stokes vector and polarization states..... 22

Table 5 - Maximum values for Faraday Rotation Angles for various wavelengths under peak TEC conditions..... 30

Table 6 - Relationship between scattering mechanism and eigenvector decompositions..... 44

Table 7 - PALSAR Image Summary..... 68

Table 8 - Results of Linear Analysis of decomposition Parameters for March 25, 2009 PALSAR quad-pol image..... 78

Table 9 - Linear regression results for May 15, 2009 PALSAR image 80

Table 10 - R^2 results of linear regression analysis over the Northern May 15, 2009 PALSAR image 82

Table 11 - R^2 results from linear regression of Decomposition parameters of PALSAR June 8th image. 85

Table 12 - Linear Regression R^2 results of combined analysis of four PALSAR images examining 13 different wildfire events over 70 years. 86

Table 13 - Correlation between extracted decomposition parameters for 18 fire events over the 70-year span. 87

Table 14 - Confusion Matrix Four Maximum Likelihood Classification of June 6 PALSAR image using Alpha, Entropy, Radar Vegetation Index and Luneburg Anisotropy..... 89

Table 15 - Confusion Matrix for MLC classification using Alpha, Entropy, and RVI for May 15 set of PALSAR image..... 95

Table 16 - $\sigma_0$statistics for temporal Radarsat-2 images..... 102

Table 17 - Comparison of Classification Results Between September 22 and June 18 2013 Radatsat-2 images..... 104

Glossary

Anisotropy – property describing directionally dependent scattering.

Azimuth - The azimuth is defined as the along track dimension of the radar system.

Backward Scattering Alignment –A right handed coordinate system where the Z axis pointing towards the target. By IEEE convention this is the alignment of choice for monostatic systems.

Bistatic system – a radar system where two separate antennas are used for transmit and receive.

Decomposition - a technique to extract physical target information of the the averaged dominant scattering mechanism from either the three by three coherency matix or the four by four meuller matrix of scattering data

DEM – Digital Elevation Model **.**

Error of commission – a classification error where a pixel is incorrectly classified (a false positive) – values below the diagonal in a confusion matrix.

Error of omission – a classification error where a pixel is not correctly classified (a false negative) – values above the diagonal in a confusion matrix.

Forward Scattering Alignment –A right handed coordinate system where the Z axis is pointing towards the receiver. This alignment is useful for bistatic radar systems .

Faraday rotation – the rotational effect caused as a radar signal passes through the ionosphere.

Fuel loads – The amount of accumulated biomass in the forest that is available as fuel for a wildfire.

Hermitian Matrix – A square matrix with complex values where the matrix is equal to its own conjugate transpose.

Satellite Image – An individual image of a scene (location) acquired by a spacecraft.

Isotropy – property describing identical scattering in all directions.

Left handed coordinate system - a coordinate system defined using the left hand where the thumb points in the positive Z axis direction and the fingers curl from the positive X axis to the positive Y axis.

Look Angle – the angle at which a radar system looks at the surface of the earth. The angle is considered steep in the near range (close to nadir) and is shallow in the far range.

Looks – individual looks as groups of signal samples in a SAR processor that splits the full synthetic aperture into several sub-apertures, each representing an independent look of the identical scene.

Monostatic system - a radar system where a single antenna is used to transmit and receive.

Multilook Radar Data – the incoherent summing of single look complex data that produces an image with less speckle and decreased resolution.

Nadir- the direction pointing directly below a satellite towards earth.

Orthorectification – the process of geometrically correcting the pixels of an image to a map projection with an uniform scale

Polarization orientation – The orientation angle of an electromagnetic wave's lines of electric flux

Positive Semi-definite Matrix – A matrix where all the eigenvalues are greater than or equal to zero.

Range - The radar range is defined as direction perpendicular to the direction of travel.

Rank of Matrix – largest number of linearly independent column or row vectors of a matrix.

Right-Handed Coordinate System – The coordinate system defined using the right hand where the thumb points in the positive Z axis direction and the fingers curl from the positive X axis to the positive Y axis.

Radar Cross Section – A ratio of the amount of energy retransmitted by a target verses the amount reaching the target.

Radar Vegetation Index – is a eigenvalue derived index that correlates the amount of vegetation or biomass with a range of values [0 , 4/3].

Scene – a predetermined geographic set of co-ordinates that correspond to the location of a satellite image which is dictated by the orbital characteristics. One can have multiple individual images of different dates of a single scene (location).

Sigma naught (Σ_0) – the amount of energy in deciBels received by the instrument divided by the amount of energy transmitted.

Single Look Complex – A format of deliverd radar data where the SAR processor has split the synthetic aperature radar into sub-aperatures, with each providing a look of the same scene. This product provides the highest possible resolution but is prone to speckle noise.

Site Index – A factor that describes the productivity of a forest area that encompasses soil type, nutrient availability, moisture availability, climate, and topography.

Slant range – the distance from the radar system to the point on the ground.

Span – total received scattered power, which is equal to the sum of the absolute value of square of all the elements of the S matrix.

Swath Width - The swath width is the range length of the area of illumination.

TEC – Total electron content of the Ionosphere which is responsible for the Faraday rotation of radar signals that pass through it.

Trace – equivalent to the span.

Acknowledgments

The author would like to acknowledge the following groups for their support of this work. Dr. David G. Goodenough for his guidance and patience in the course of this work. Japanese Space Agency (JAXA) and the Alaska Satellite Facility (ASF) for their assistance in scheduling and acquiring PALSAR L-band radar data over the study areas. The Canadian Space agency (CSA) and , Macdonald Dettwiler and Associates Corporation (MDA) for providing the Radarsat-2 C- band radar data. The European Space Agency (ESA) for the POLSARPRO software tool kit without which this work would not have been possible. Wendy Myrvold for her patience, guidance, support and understanding through this process. Ashlin Richardson for his expertise in understanding and evaluating the mathematical and statistical techniques of both the radar processing techniques, and the subsequent classification and modelling process. Hao Chen for his knowledge, time and system support. Nick Soverel of UBC and Darrell Zell of Parks Canada for their CBI ground survey data.

Dedication

The author would like to dedicate this work to his family who without whose patience and support this work would not have been possible. In particular, my mother, June Hobart whose steadfast belief in the importance of education, ultimately provided the inspiration for this project.

1.0 Introduction

The boreal forest covers 11% of the Earth's land surface - 1.4 billion hectares (ha) - and contains 37% of the planet's terrestrial carbon reservoir, which is more than the combined total of both the tropical and temperate forests [1, 4]. This estimate translates to 703 Petagrams (Pg) of carbon with the vast majority contained within organic soils, and peat. Much of this carbon has been sequestered, until now, within the peat bogs and permafrost layers for millennia [2, 3, 9, 11].

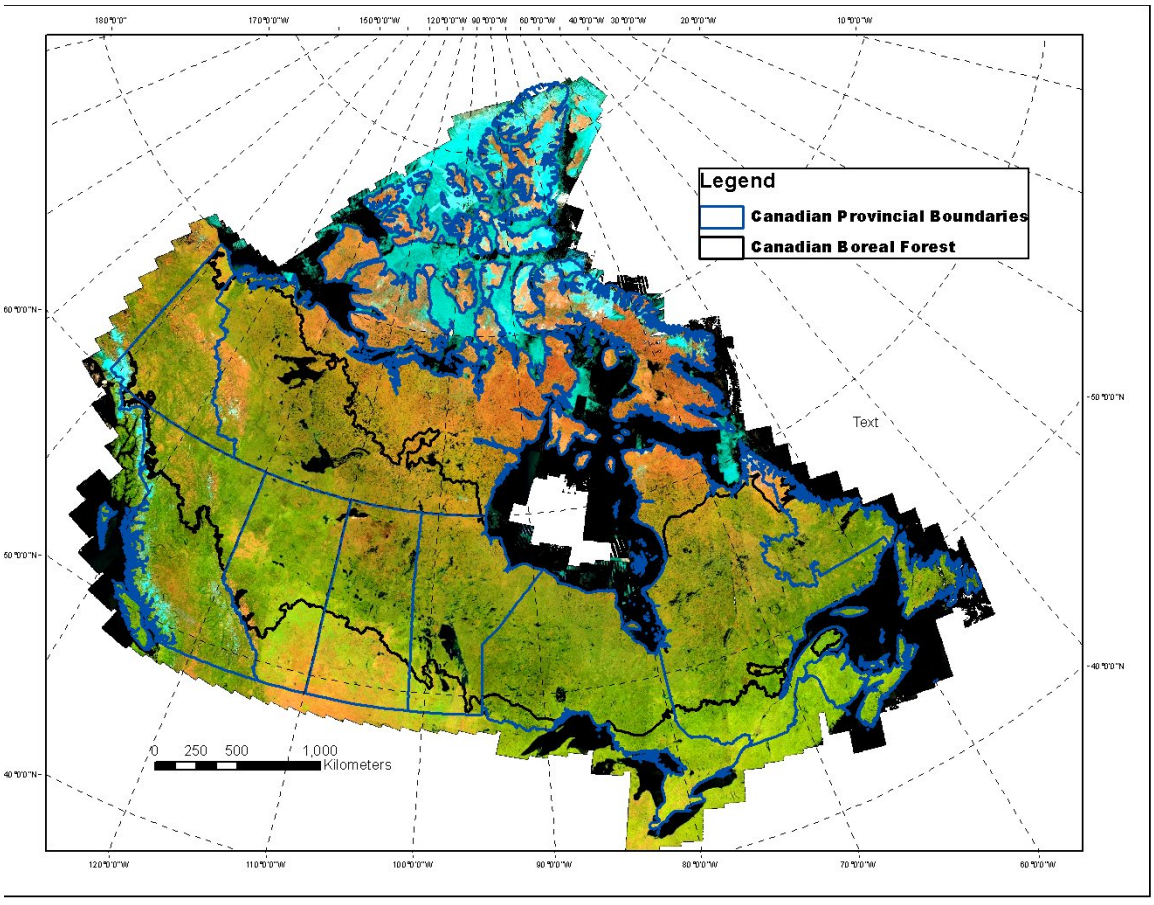

Figure 1 **- Canadian boreal forest extent overlaid on 2009 Landsat 5/7 composite image.**

The western North American boreal forest is a wildfire ecosystem [2, 5-7, 15] where fires typically occur every 50 to 200 years [8, 9] allowing vast quantities of carbon to re-enter the

atmosphere. Understanding and estimating past fire history and the related changes in the carbon budget [3, 4, 7, 10, 16-18] in this biome is of significant importance for climate researchers as they attempt to model and predict future changes in the planet's climate [2, 4, 11-14]. Moreover, in this crucially important ecosystem, public and private forest resource managers have an interest in past fire history to predict fuel loads [19] and to develop management strategies [10, 20, 21] to adapt to a changing climate [4, 22].

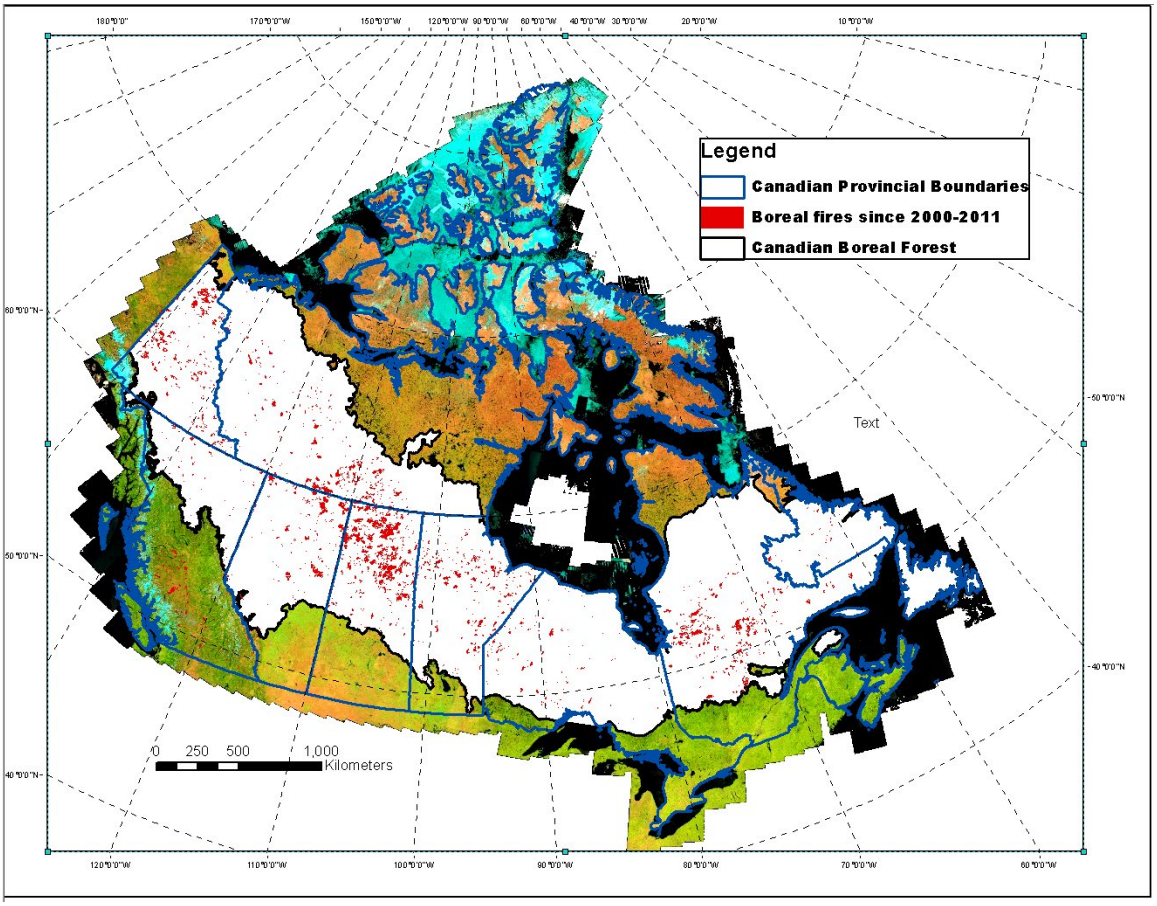

Figure 2 - Boreal wildfires greater than 200 ha between 2000 and 2011

The documented effects of climate change in the northern latitudes includes an increase in summer temperature and a decrease in moisture availability over the past fifty years [7, 22-24] which has created a positive feedback mechanism [3, 11-13, 15] within the boreal ecosystem

between wildfires and climate change [3]. In the past 20 years, the area burned by wildfires has increased by 100 percent in the North American boreal forest and surface air temperatures have increased by 0.3^{o}C each decade [3]. Wildfire is a dynamic process, which can vary greatly in intensity and its effects on the landscape [7, 8, 21, 25]. Canadian boreal wildfires burn between 1 and 4 million ha of forest each year releasing an average of 27 Teragrams (Tg) of carbon directly into the atmosphere [15]. Post fire decomposition may well equal the direct releases and it can take between 10 and 30 years for the net carbon flux of the forest to return to pre-fire levels [15]. Intense wildfire events can burn not only the above ground vegetation, but also the protective layer of peat which acts as an insulator for the sequestered carbon of the permafrost layers [8, 22]. The loss of the insulating peat layer has a major impact on the soil temperature and hence amount of carbon that is released from the permafrost layers for between 10 and 50 years after the original fire event [8].

Many techniques are available to remotely sense wildfires during and immediately after an event. Real time detection is done operationally with Moderate Resolution Imaging Spectroradiometer (MODIS) data but the resolution is low (500m to 1km) and the results can be biased by cloud cover and thus neglect low intensity fires [4]. The Advanced Very High Resolution Radiometer (AVHRR) [2, 4, 6, 26], and Advanced Space Borne Thermal Emission and Reflection Radiometer (ASTER) have also been used to map forest fires but again the resolution is quite low [6]. Optical systems such as Landsat can be used to map recent forest fires and estimate burn severity using the Normalized Burn Ratio (NBR) [27, 28] or by differencing the Normalized Difference Vegetation Index (NDVI) calculated from pre- and post-fire images to create a differenced Normalized Burn Ratio (dNBR) [25, 29-32]. While useful, this technique can be operationally challenging to obtain two quality images at the correct time intervals due to

environmental conditions and solar illumination angles in northern latitudes [25]. Synthetic aperture radar (SAR) systems, which are sensitive to moisture differences and structural changes in the forest, have been used to map fire scars for up 13 years after an event with the C-Band European Remote Sensing Satellite (ERS-1) [2, 11] and both the Canadian C-Band Radarsat-1 [2, 33], Radarsat-2 [34]and Japan's Advanced Land Observing Satellite (ALOS) L-Band Phased Array Synthetic Aperture Radar (PALSAR) [16, 34].

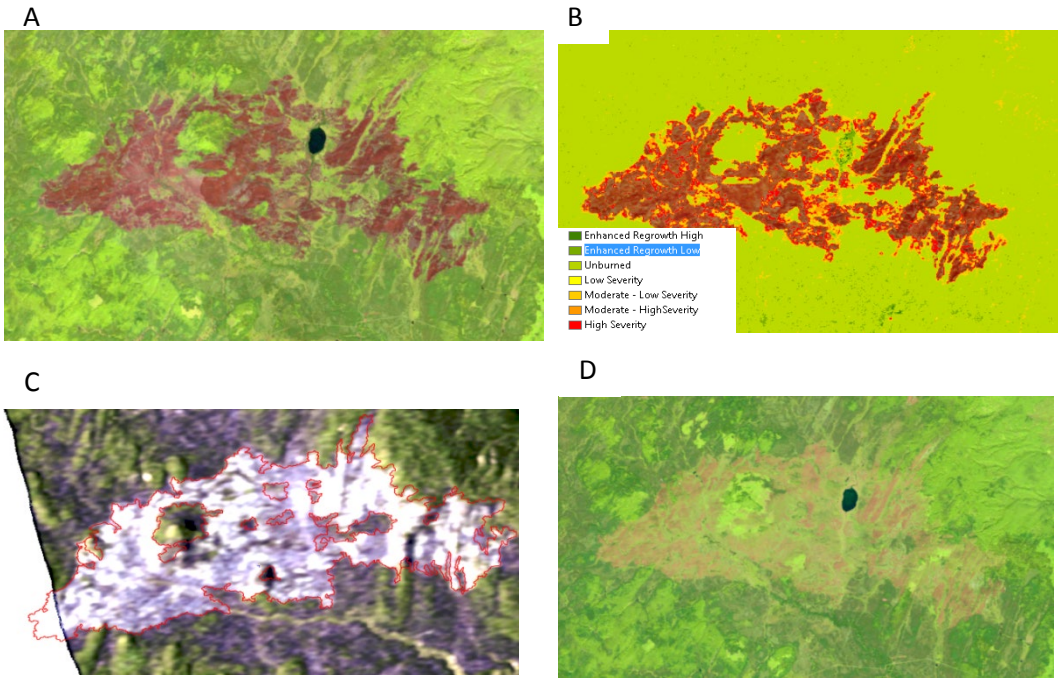

Figure 3 - Comparative images for 2002 Keg River Fir. A) RGB (Bands 543)2002 Landsat image immediately after fire, B) dNBR image generated from 2 Landsat images pre and post fire, C) Alpha, Entropy, Lambda 2009 PALSAR decomposition as Hue, Saturation ,Value image, and D) 2009 RGB (Bands 543) Landsat image with fire scar barely visible 6 years after the event.

Polarimetric synthetic aperture radar (PolSAR) is a relatively new tool available to remote sensing scientists. Preliminary analysis suggests that Polarimetric radar can be useful for detecting historical fire scars in the boreal forest [35]. L-Band full polarimetric radar possesses characteristics, which make it well suited to assist in this challenge. First its relatively long

wavelength ” approximately 23.6 cm with a center frequency of 1270 MHz [36] “ allows it to penetrate the structure of the forest and provide more information than C-Band Radarsat-2.

Canada’s Radarsat2 has a shorter wavelength of 5.6 cm with a center frequency of 5.3 GHz [37] which penetrates far less into the structure of the forest [38], p.340], but can still be useful as we shall demonstrate. Research performed by the Advanced Forest Technologies (AFT) group at the Pacific Forestry Centre of the Canadian Forest Service (CFS), under the direction of Dr. David Goodenough, using C-Band Polarimetric radar with a six meter resolution Airborne

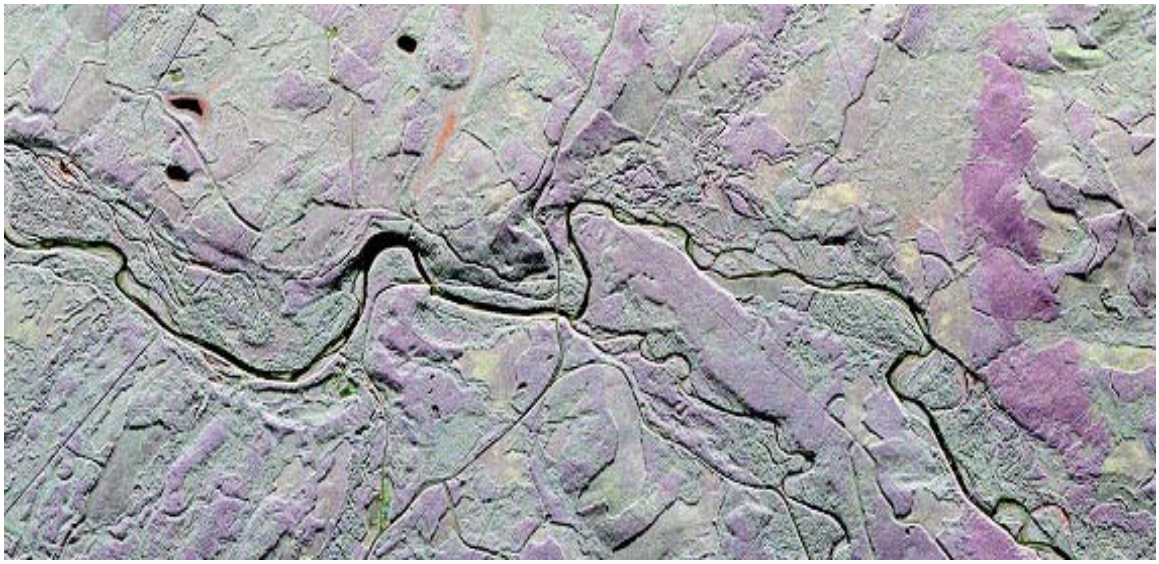

Figure 4 - PAULI decomposition of C-Band Polarimetric radar collected over Hinton Alberta with crescent shaped 50 year old fire scar visible on the right hand side of the image

Synthetic Aperture Radar (ASAR) data collected in 2004 demonstrated the ability to detect 50 year old fire scars over Hinton in the southern foothills of Alberta [39].

Active radar systems, unlike passive optical satellite systems, allow data to be collected in all seasons, day, night and in cloudy weather conditions [38], p.5]. Being able to detect and inventory past fire events in an accurate and efficient manner would be valuable information for

resource managers and carbon and climate scientists. The research questions of this thesis centers on:

1) How can we extract historical fire scar information from polarimetric SAR?
2) Can polarimetric SAR be used to detect and date historical wildfire events in the boreal forest of western North America?
3) Can polarimetric SAR be used to assess the severity of past wildfire events on the boreal landscape with particular attention to the area burned?

Work thus far using Japan's ALOS Phased Array type L-band Synthetic Aperture Radar (PALSAR)and Radarsat-2 data sets has yielded strong linear correlations between various L Band and C Band polarimetric decomposition parameters and the year in which a boreal fire event occurred in an area of northern Canada bordering the provinces of British Columbia and Alberta [16]. While these correlations are promising, the inversion of this simple linear model reveals that the variation within the measured parameters of a single known fire event can often span several decades This research will provide new insights into the potential of full polarimetric radar's ability to derive important information about the fire history of the boreal forest.

Interrogating radar images to detect historic fire scars is a highly involved process that requires a vast array of data sets which we shall introduce in the next chapter. Furthermore, the multistage process of constructing radar products ready for analysis is not static. Many choices can be made that affect the information content of the final product. To elucidate these choices, chapter three will provide a background in radar physics that will provide the mathematical foundation required to appreciate the decisions that were made at each stage of the processing and analysis. Chapter four will describe the computing infrastructure and the process chain used. Chapter five will provide both a description of the various experiments performed and a summary of the results with this extensive set of radar data. Chapter six will

discuss the final conclusions of this project and address the previously stated research questions. Finally chapter seven will recommend some possible dirrections for further research in this area.

2.0 Study Area and Data Sets

Polarimetric radar is an emerging technology whose full potential is still being actively explored and discovered. This research is ground-breaking since very little work has been performed investigating polarimetric radar for historical boreal wildfire information. This area of investigation is a complex marriage of forestry, geospatial information and radar engineering that requires an extensive array of data sets to facilitate analysis. This chapter will introduce all the various data sets that were necessary for this project.

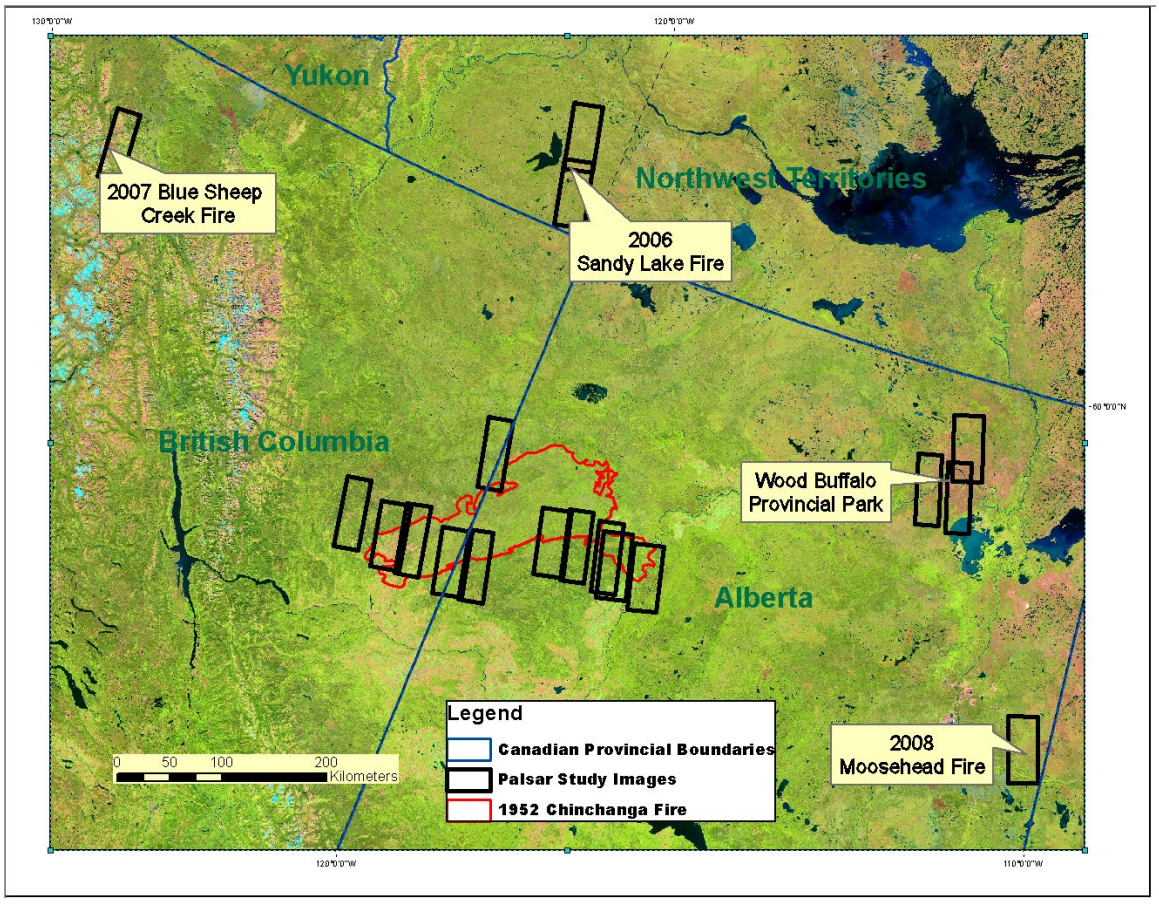

Figure 5 - Study Area centered on Chinchaga wildfire with PALSAR image footprints

The primary study area selected for this project is a subarea in the northern portion of the Canadian province of Alberta bordering British Columbia, Saskatchewan and the Northwest

Territories. This area is centered on the Chinchaga fire of 1950 (a major wildfire event located in this area) which burned 1.5 million hectares over a five-month period. This area was selected due to the high density and frequency of wildfires in this area and the availability of historic wildfire information available from the government of Alberta.

The study area was expanded to include several more recent fires, which aided in the analysis phase of this project. These recent fires included the 2007 Blue Sheep Creek fire in northern British Columbia (BC), the Moosehead fire of northeastern Alberta in 2008, and the 2006 Sandy Lake fire of the Northwest Territories. Ancillary datasets generated from extensive fieldwork by Parks Canada in the Wood Buffalo National Park and UBC master's student Nick Sorvino in the Sandy Lake fires were of particular interest in exploring the connection between observed fire severity on the ground using the US Forest Services Composite Burn Index (CBI) and the polarimetric radar signatures.

2.1 Polarimetric Data Sets

This work focuses on full polarimetric radar data of the C-Band Radarsat-2 and the L-Band PolSAR satellite radar platforms. Table 1 presents a condensed summary of the most commonly used microwave radar bands and their physical characteristics. The size of a radar signal's wavelength determines the minimum size of an object that can scatter the electromagnetic energy back to the antenna.

This project examined 18 full polarimetric PALSAR L-Band and 6 Radarsat-2 C-Band images over the broader study area. The PALSAR images were acquired between the fall of 2007 and spring of 2009. Other 2009 PALSAR images were acquired over the 2007 Moose Head fire, the 2008

Table 1 - Summary of the most common radar microwave bands and their physical characteristics.

Band Name	Frequency Range	Wavelength range
P Band	< 300Mhz	> 1 m
L Band	1-2 GHz	15-30 cm
S Band	2-4 GHz	7.5-15 cm
C Band	4 -8 GHz	3.75-7.5 cm
X Band	8-12	2.5-3.75 cm
K, K_a, K_u Bands	12-40 GHz	0.75 -2.5 cm

Blue Sheep Creek fire, the 2006 Sandy Lake fire, and multiple fires over Wood Buffalo Provincial Park. The Radarsat -2 C Band full polarimetric images were all obtained over the 2002 Keg River Fire within the eastern section of the 1952 Chinchaga fire event in northern Alberta. All six of the Radarsat-2 images were obtained over the 2002 Keg River fire over the course of a single growing season providing a unique opportunity to explore the seasonal variation of radar responses for boreal wildfire scars.

2.2 Federal, Provincial, and Territorial GIS Fire Data Sets

British Columbia, Alberta and the Northwest Territories governments all maintain GIS wildfire databases. These data consist of polygons with attributes describing ignition sources, ignition dates, hectares burned, and other relevant statistics. These data were used to identify fire scars and assist in the analysis of radar signatures with respect to ignition dates. While these data sets were useful, they do not always accurately capture the exact boundaries of fire events, which can be complex due to the existence of unburned “islands” and further they do not account for the level of burn severity with a fire event.

2.3 NFDB National Fire Database

The Canadian National Fire Database (NFDB) records all wildfires larger than 200 ha that occur in designated forested areas [6, 15]. This database is maintained by the Canadian Forest Service(CFS) using data provided by provincial, territorial and federal agencies which includes spatial information of areas burned and attribution such as ignition date and source, and suppression actions [15]. The database is reasonably accurate for all large fires that occurred since 1959 and efforts have been made to include historical wildfire events that occurred prior to this time [15]. The data were collected using a wide variety of tools and techniques including ground surveys and both airborne and satellite optical data [15]. The previously stated issues of accuracy apply to the NFDB since most of the information originated with the data sets of Section 2.2.

2.4 Landsat 4, Landsat 5 and Landsat 7Optical Imagery and Burn Indexes

Landsat 4,5 and 7 are optical multispectral satellites with a spatial resolution of 30 m operated by the U.S. National Aeronautics and Space Administration (NASA) and the U. S. Geological Survey (USGS). Since the beginning of 2009, the Landsat archive has been freely available for download. The Forest Geomatics Group of the Canadian Forest Service has been involved in generating rule based composite images for all Canada to take advantage of all this freely available public data [40]. A series of over 85,000 images have been acquired for the years 1984 through 2012 and Best Available Pixel (BAP) composites were generated for each year based on a target date of August 1. For areas of interest, a Normalized Burn Ratio (NBR) was calculated for each year. A normalized burn ratio is calculated using this formula

$$NBR = \frac{(R_4 - R_7)}{(R_4 + R_7)} \qquad (1)$$

where R_i refers to the reflectance and the subscript refers to the i^{th} spectral band of the Landsat sensor. Band four is the red band (wavelength bandwidth of 0.631-0.692 μm) and band seven is the Short Wave Infrared (SWIR) (wavelength bandwidth of 2.064 -2.345 μm). A differenced Normalized Burn Ratio (dNBR) was generated by differencing 2 sequential years NBR values (one pre and one post fire) as follows:

$$dNBR = NBR_{prefire} - NBR_{postfire}\,. \qquad (2)$$

The values of the dNBR can be interpreted using Table 2.

Table 2 - Summary of Interpreted dNBR values

Severity Level	dNBR Value Range
Enhanced Regrowth High	-500 to -251
Enhanced Regrowth Low	-250 to -101
Unburned	-100 to 99
Low severity	100 to 269
Moderate – Low Severity	270-439
Moderate – High Severity	440 to 659
High Severity	660 to 1300

Best Available Pixel (BAP) [40] composites were used to determine land cover and burn indexes were calculated to aid in the selection of sample points within the study areas.

2. 5 Parks Canada Ground Survey Data for Wood Buffalo National Park

Parks Canada has been accumulating ground reference data of wildfire burn severity known as the composite burn index (CBI) for several years. These data provided a unique opportunity to explore the possible connection between the observed variability within radar signatures and the burn severity of a wildfire event. The vast majority of these data were collected within the

boundaries of Wood Buffalo National Park. The composite burn index stratifies the landscape into 5 categories:

4) Substrates,
5) Herbs and low shrubs (<1m),
6) Tall Shrubs and trees (1-5 m),
7) Intermediate trees (sub-canopy), and
8) Big trees (Upper canopy, dominant trees).

A field surveyor then attempts to quantify the level of severity of the wildfire event with a value of 1 to 5 for each of the landscape strata. An example of a CBI field survey data sheet is included in Appendix A.

2.6 NTDB Digital Elevation Model

The Canadian Digital Elevation Data (CDED) were obtained at a scale of 1:50,000 from the Canadian Government's GeoBase web portal [41]. These data sets were required to transform these radar images from slant range into a geo-referenced format. These data were downloaded as National Topographic System (NTS) individual map sheets and then fused together as required to create a complete DEM coverage for each radar image.

3.0 Methods and Analysis Theory

Full-polarimetric radar imaging analysis is a nascent area of research that has an extremely complex multistage process depending on the choices made at each stage. To appreciate the process nuances, it is highly valuable to have knowledge of the underlying physics and engineering choices made to produce these images. Furthermore, to completely understand and appreciate the processing paths that are chosen one must understand mathematical theories and principles that underpin the basics of radar engineering. This chapter, first, will introduce the reader to the basic physical notations and then explore the various processing options and products available at the various stages. It should be emphasized, that several pseudo-equivalent electromagnetic signal representations will be presented each with their own unique characteristics. For example the Stokes vector is an instantaneous real valued measurement whereas the representation of a signal on the Poincare sphere is a continuous value in time recorded in spherical coordinates.

3.1 Radar Introduction

Radar is defined as Radio Detection and Ranging of microwave electromagnetic radiation. In its simplest form, a radar system emits an electromagnetic pulse and any reflected energy from a target is measured for both direction and elapsed time from transmission to determine the distance (range) from the time element which combined with the measured direction element allows the system to ascertain the reflected source's position relative to the system [42, 43], p. 341]. Modern radar systems use several techniques to improve the information content of the imagery produced. The exact processing techniques required to generate an image from the raw received radar signal are well beyond the scope of this project, but an introduction to some of the fundamental concepts is a valuable exercise.

Synthetic Aperture Radar (SAR) leverages the relative motion of a radar system's antenna with respect to the target to achieve a finer azimuth resolution [38], p. 9,[42], p. 340]. This is accomplished by utilizing Doppler beam sharpening of the radar signal [38, 42]. A transmitted radar signal expands as it moves away from the receiver illuminating a large area orthogonal to the direction of travel. Thus a given target area generates a series of reflected signals as the platform moves past it. By using the Doppler shift these signals can be combined to enhance the information within the target area. [38, 42]. A phased array antenna consists of an array of spatially distributed antennas which can achieve the same result as a SAR system [43]. Another enhancement technique of modern radar systems is to emit a longer radar pulse as a "chirp" in

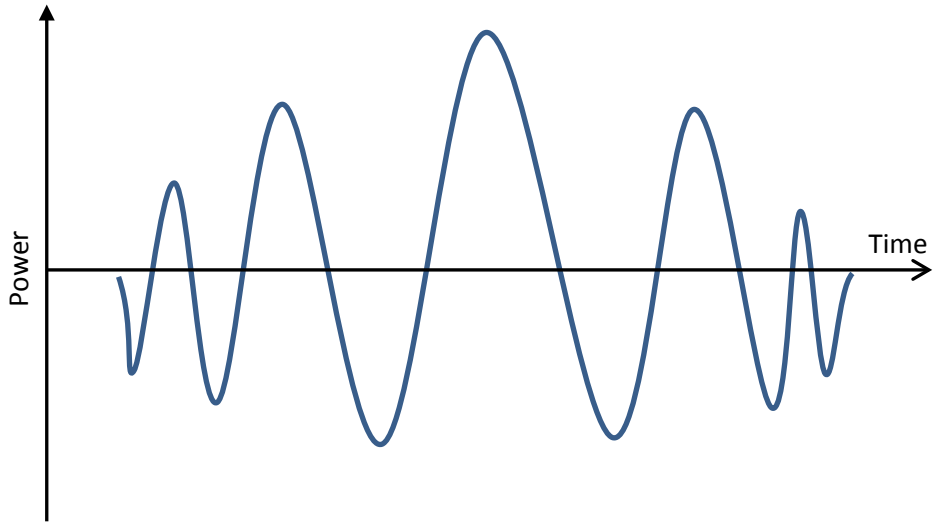

Figure 6 - Example of chirped radar pulse where both the phase and amplitude vary with time

which the frequency and amplitude are shifted [38]. Generally a longer radar pulse improves the amount of energy reflected back to the system at the expense of range resolution. The chirped signal has the benefits of 1) increasing the signal to noise ratio (SNR), 2) improving the range

resolution by compressing the signal in the time domain using a Fourier transformation and 3) it consumes less power than simply using a longer pulse [38].

It should be noted that modern satellite radar systems are known as side-looking. That is, they transmit their beam at an oblique angle perpendicular to the direction of travel [38]. The radar range is defined as direction perpendicular to the direction of travel. The azimuth is defined as the along track dimension of the radar system. The swath width is the range length of the area of illumination [38]. Generally, most radar images are delivered from the satellite provider in single look complex format and in a slant range basis coordinate system which is not a standard geographic basis. A complex transformation is required to generate a geo-located image from this slant range product.

Polarimetric radar data refers to the transmission of polarized or linearly oriented electromagnetic waves [43]. The linear aspect of these systems' signals provides the opportunity to analyze radar signals using classic algebraic techniques to derive far more information than was previously possible from earlier radar systems [38].

3.2 Radar Polarimetry

Polarimetry is defined as the measurement and analysis of polarized electromagnetic waves [42]. Electromagnetic waves have both an electric field component and an orthogonal magnetic field component [42]. This dissertation will focus solely on polarized electrical fields generated and received by a radar system and will not specifically address the magnetic nature of these systems.

When an electrical plane wave strikes a target, a current is induced within that object that is related to the object's dielectric properties and its orientation with respect to the original signal [42]. This reactionary current in turn produces a reflected electrical plane wave which carries both information from the original signal and the properties of the irradiated target. This process is referred to as scattering [42]. Radar polarimetry for this thesis refers specifically to the transmission and reception of linearly polarized microwave signals which possess both a phase, amplitude, and an orientation in space [42]. The linear orientation allows for the definition of a three dimensional basis transverse to the direction of propagation which can be used to describe the properties of the electromagnetic wave. This basis can provide a frame of reference to observe and interpret the scattered wave with respect to the properties of the target [42].

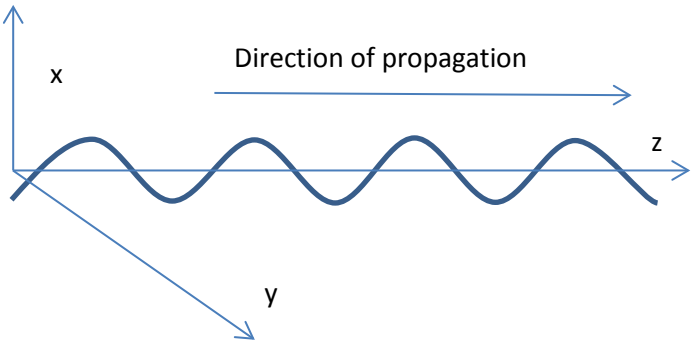

Figure 7 - Linear polarized electromagnetic plane wave and reference frame basis

Polarized microwave radiation can be described as an electromagnetic plane wave whose properties can be described by any orthogonal basis defined to be transverse to the direction of propagation [38].

The generalized equation describing the electric field properties of a linearly polarized wave travelling along an arbitrary defined axis z can be described by this equation [42]:

$$E_{Incident} = \begin{bmatrix} 1 \\ 1 \\ 0 \end{bmatrix} E e^{-i\omega t} = E(\sin(\omega t + \delta_x) + i * \cos(\omega t + \delta_y)) \quad (3)$$

where E is the amplitude of the electric field and **ω** is the angular frequency of the electromagnetic wave and δ is the phase constant. When an electromagnetic wave encounters

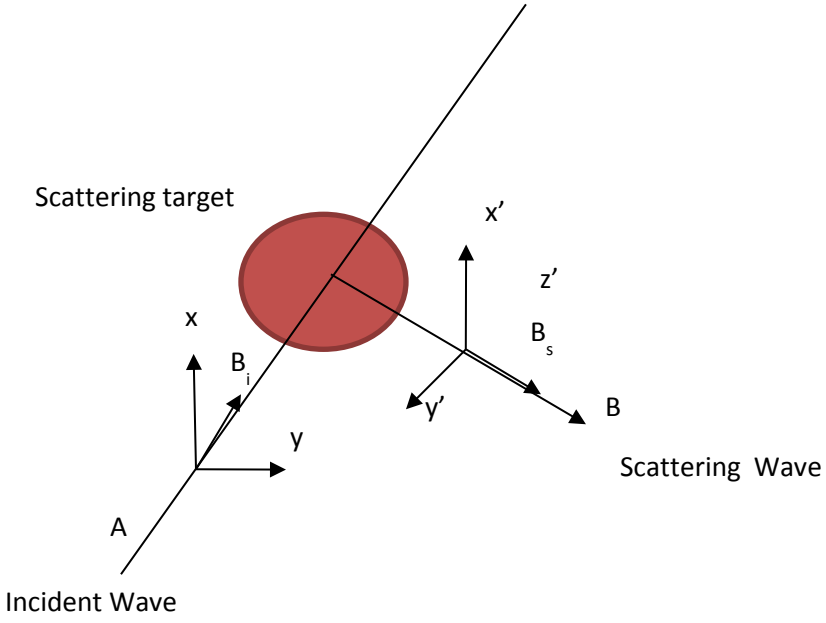

Figure 8 - Geometry of an incident electromagnetic wave and the resultant scattered wave after encountering a target[42](p46)

an object it induces a current within the object which retransmits the wave energy, some of which is directed back at the source antenna [42]. The resultant wave will be deflected from its original linear orientation based on the structural and dielectric properties of the target encountered [38]. The scattered wave $\overrightarrow{E_{sctr}}$ obeys the equation:

$$\overrightarrow{E_{sctr}} = \begin{bmatrix} E_x \\ E_y \\ 0 \end{bmatrix} e^{-i\omega t} = \begin{bmatrix} \overrightarrow{E_x}\sin((\omega t + \delta_x) + i * \cos(\omega t + \delta_x)) \\ \overrightarrow{E_y}\sin((\omega t + \delta_y) + i * \cos(\omega t + \delta_y)) \\ 0 \end{bmatrix} \quad (4)$$

where $\overrightarrow{E_x}$ and $\overrightarrow{E_y}$ are the respective x and y maximum amplitude components of the scattered

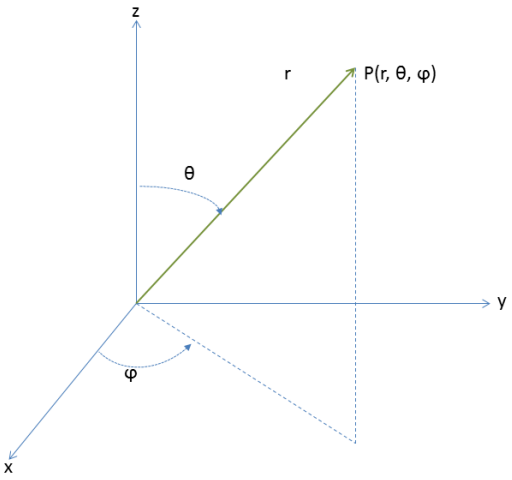

Figure 9 - Example of polar co-ordinate system for vector r

wave [38]. The matrix form of the equation 4 is referred to as the Jones Vector [38].

It should be emphasized that orthogonal X-Y basis can be defined arbitrarily in any number of ways as long as the direction of propagation is orthogonal to this basis. This dimensional freedom allows for any number of transformations to be applied [38].

For convenience a back scattering alignment (BSA) where the basis is defined with respect to the incident wave source is employed. This simplifies the analysis since the source and receiving

antenna are co-aligned [38]]. Due to the 4-dimensional nature in space and time, electromagnetic waves can also be described in terms of spherical coordinates [38].

3.2.1 Poincare sphere

Any vector can be described as a function of its radius r, the angle θ with respect to the x axis and angle φ with respect to the z axis and time t. The Poincare sphere is a graphical formulation based on the spherical coordinates that allows for the graphical representation of polarized electromagnetic waves [42]. The premise that any electromagnetic wave can be traced on this sphere allows for simple visualization of the various states of polarized electromagnetic radiation.

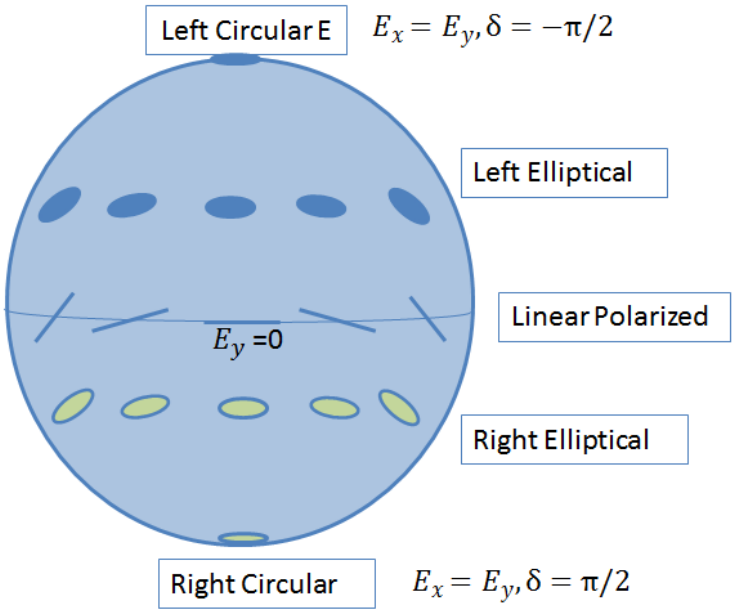

Figure 10 - Poincare sphere for visualization of polarized electromagnetic waves.

This model allows for a direct visualization of how an electromagnetic wave moves through space. We are primarily concerned with linearly polarized waves which are always located on the equator of the sphere. Horizontal polarized waves lie flat on the equator while vertically polarized waves are orthogonal to the equator on the opposite (antipodal) side of the sphere [42].

3.2.2 Stokes Vector g

Polarized electromagnetic waves can also be described in terms of the four real Stokes Parameters [42]. These parameters can be combined to create the Stokes Vector given by the equation:

$$g = [I \quad Q \quad U \quad V]^T. \quad (5)$$

The value of the individual parameters is measured intensity at the following points on the Poincare sphere. The Stokes parameters have unique definitions that describe their relationship to polarizations visualized on the Poincare sphere as shown in Tables 3 and 4 [38].

Table 3 - Stokes parameters.. I stands for the real valued measured intensity of the signal. The degrees stated in the I() function represent the orientation of the antenna. RCP and LCP stand for right and left circular polarization. The phase constant δ is equal to δ_x - δ_y

I	$E_x^2+E_y^2$	Intensity
Q	$E_x^2-E_y^2$	I(0°) – I(90°)
U	$2E_xE_y\cos(\delta)$	I(45°) – I(135°)
V	$2E_xE_y\sin(\delta)$	I(RCP) – I(LCP)

Table 4 - Stokes vector and polarization states

Equation Definition	Horizontal Polarization	Vertical Polarization	+45° Polarization	-45° Polarization	Right Circular Polarization	Left Circular Polarization
$\vec{g} = \begin{bmatrix} I \\ Q \\ U \\ V \end{bmatrix}$	$\vec{g} = \begin{bmatrix} 1 \\ 1 \\ 0 \\ 0 \end{bmatrix}$	$\vec{g} = \begin{bmatrix} 1 \\ -1 \\ 0 \\ 0 \end{bmatrix}$	$\vec{g} = \begin{bmatrix} 1 \\ 0 \\ 1 \\ 0 \end{bmatrix}$	$\vec{g} = \begin{bmatrix} 1 \\ 0 \\ -1 \\ 0 \end{bmatrix}$	$\vec{g} = \begin{bmatrix} 1 \\ 0 \\ 0 \\ 1 \end{bmatrix}$	$\vec{g} = \begin{bmatrix} 1 \\ 0 \\ 0 \\ -1 \end{bmatrix}$

3.3 Full Polarimetric Radar Characterizations

Most modern polarimetric radar systems have many different modes of operation. These systems can vary the look angle of the system as well as the polarization orientation of the transmitted signal [38]. Quad-pol or full polarimetric mode refers to the transmission of alternately polarized horizontal (H) and vertical (V) signals which are reflected off a target and then both signals are received on both the horizontal and vertical antennas. This configuration produces four complex channels of data which are labeled HH, HV, VH, and VV where the first letter describes the transmit polarization and the second letter indicates the receive polarization. The quad-pol mode provides the most robust scattering information at the cost of spatial resolution since the pulse repetition frequency (PRT) must be decreased to accommodate two different polarization transmit/receive cycles [44].

3.3.1 Sinclair Scattering Matrix

The transmit and receive signals of a radar system can be represented in a format known as the Sinclair scattering matrix [38]:

$$S_2 = \begin{bmatrix} S_{HH} S_{HV} \\ S_{VH} S_{VV} \end{bmatrix} = \begin{bmatrix} S_{11} S_{12} \\ S_{21} S_{22} \end{bmatrix}. \qquad (6)$$

The subscripts in this equation represent the transmit and receive polarizations respectively for each channel of the radar system where H (or 1) represents the horizontal polarization and V (or 2) represents the vertical polarization. Each complex channel contains amplitude and relative phase information. Each received signal carries information in both the total power returned but also the signal's relative phase with respect to the transmitted phase for each of four complex data channels.

The co-pol channels are defined as S_{HH} and S_{VV} whereas the cross-pol channels are the S_{HV} and S_{VH} elements. By convention a coordinate system basis is defined such that for the transmit $\vec{S}_{inc}$ the cross pol channels are zero [42].

3.3.2 Mueller matrix

In the case of a single coherent target, both the polarized source $\vec{g}_{inc}$ and the scattered $\vec{g}_{sc}$ wave can be measured in terms of the Stokes vectors. There must exist a real 4 by 4 matrix to perform a transform between the two vectors in the forward scattering alignment. This is known as the Mueller [M] matrix and is defined by [42]:

$$\vec{g}_{sc} = \mathrm{M}\vec{g}_{inc} = \begin{bmatrix} M_{11} & M_{12} & M_{13} & M_{14} \\ M_{21} & M_{22} & M_{23} & M_{24} \\ M_{31} & M_{32} & M_{33} & M_{34} \\ M_{41} & M_{42} & M_{43} & M_{44} \end{bmatrix} \begin{bmatrix} I \\ Q \\ U \\ V \end{bmatrix}. \qquad (7)$$

This representation is useful as it defines the scattering matrix solely in terms of power and eliminates the need to consider phase in the analysis. This relation is only valid in the case of single scattering target. In the case of ' *n* ' independent scattering objects, the scattered wave would be a superposition of all the independent distributed targets' induced waves with independent amplitude and phase:

$$\vec{g}_{sc} = \sum_{i=1}^{n} \vec{g}_{sc_i} = \left(\sum_{i=1}^{n} M_i \right) \overrightarrow{g_{inc}} \quad . \qquad (8)$$

3.3.3 Kennaugh matrix

The Kennaugh matrix [K] is identical to the Mueller matrix except that it is defined in terms of the backscattering alignment (BSA). Both the Mueller and Kennaugh matrices can also be defined using the Kronecker tensor matrix product [38].

$$\mathrm{K} = \mathrm{A}^{*}(\mathrm{S} \otimes \mathrm{S}^{*})\mathrm{A}^{-1} \qquad (9)$$

where

$$\mathrm{S} \otimes \mathrm{S}^{*} = \begin{bmatrix} \mathrm{S_{HH}S}^{*} & \mathrm{S_{VH}S}^{*} \\ \mathrm{S_{HV}S}^{*} & \mathrm{S_{VV}S}^{*} \end{bmatrix} \qquad (10)$$

and

$$\mathrm{A} = \begin{bmatrix} 1 & 0 & 0 & 1 \\ 1 & 0 & 0 & -1 \\ 0 & 1 & 1 & 0 \\ 0 & \mathrm{i} & -\mathrm{i} & 0 \end{bmatrix}. \qquad (11)$$

3.3.4 Relationship between the Mueller and Sinclair Matrix

The previously introduced four by four real valued Mueller matrix can be generated from the Sinclair matrix using the following set of equations:

$M_{11}= ¼(S_{HH}S_{HH}^*+ S_{HV}S_{HV}^*+ S_{VH}S_{VH}^*+ S_{VV}S_{VV}^*)$, (12)

$M_{12}= ¼(S_{HH}S_{HH}^*- S_{HV}S_{HV}^*+ S_{VH}S_{VH}^*- S_{VV}S_{VV}^*)$, (13)

$M_{13}= ½ (Re(S_{HH}^*S_{HV}) + Re(S_{VV}S_{VH}^*))$, (14)

$M_{14}= ½ (Im(S_{HH}^*S_{HV}) + Im(S_{VV}S_{VH}^*))$, (15)

$M_{21`}= ¼(S_{HH}S_{HH}^*- S_{HV}S_{HV}^*+ S_{VH}S_{VH}^*- S_{VV}S_{VV}^*)$, (16)

$M_{22}= ¼(S_{HH}S_{HH}^*- S_{HV}S_{HV}^*- S_{VH}S_{VH}^*+ S_{VV}S_{VV}^*)$, (17)

$M_{23}= ½ (Re(S_{HH}^*S_{HV}) - Re(S_{VV}S_{VH}^*))$, (18)

$M_{24}= ½ (Im(S_{HH}^*S_{HV}) - Im(S_{VV}S_{VH}^*))$, (19)

$M_{31} = ½ (Re(S_{HH}^*S_{HV}) + Re(S_{VV}S_{VH}^*))$, (20)

$M_{32} = ½ (Re(S_{HH}^*S_{HV}) - Re(S_{VV}S_{VH}^*))$, (21)

$M_{33} = ½ (Re(S_{HV}^*S_{VH}) + Re(S_{HH}^*S_{VV}))$, (22)

$M_{34}= ½ (Im(S_{HH}^*S_{HV}) - Im(S_{HV}^*S_{VH}))$, (23)

$M_{41}= ½ (Im(S_{HH}^*S_{HV}) + Im(S_{VV}S_{VH}^*))$, (24)

$M_{42}= ½ (Im(S_{HH}^*S_{HV}) + Im(S_{VV}S_{VH}^*))$, (25)

$M_{43}= ½ (Im(S_{HH}^*S_{VV}) + Im(S_{HV}^*S_{VH}))$, and (26)

$M_{44} = ½ (Re(S_{HV}^*S_{VH}) - Re(S_{HH}^*S_{VV}))$. (27)

3.3.5 Scattering Target Vectors

To extract the physical information from the Sinclair matrix S it is desirable to construct a linear vector by employing a complex basis of 2 by 2 matrices [38]. The Lexicographic basis and Pauli matrices are both commonly used and will be described in detail in the following sections.

3.3.5.1 Lexicographic Vector Representation of Scattering

The Lexicographic basis is defined as [38]:

$$\Psi_L = \left\{2\begin{bmatrix}1 & 0\\ 0 & 0\end{bmatrix}\ \ 2\begin{bmatrix}0 & 1\\ 0 & 0\end{bmatrix}\ \ 2\begin{bmatrix}0 & 0\\ 1 & 0\end{bmatrix}\ 2\begin{bmatrix}0 & 0\\ 0 & 1\end{bmatrix}\right\}. \quad (28)$$

Hence, the scattering Lexicographic feature vector becomes [38]:

$$\Omega = [S_{HH}\quad S_{HV}\quad S_{VH}\quad S_{VV}]^T\ . \quad (29)$$

Since we will be dealing with the monostatic case we can assume the vector reciprocity theorem holds, thus the back scattering alignment of the scattering matrix [S] must be symmetric such that $S_{HV} = S_{HV}$ and the vector can be simplified [38]:

$$\Omega = \left[S_{HH}\quad \sqrt{2}S_{HV}\quad S_{VV}\right]^T. \quad (30)$$

3.3.5.2 Pauli Vector Representation of Scattering

The Pauli matrix is another useful representation of the scattering matrix for single-look complex data [45]. It is generated by transforming the scattering matrix S and then applying the Pauli spin matrix basis set Ψ_p where

$$\Psi_p = \left\{\sqrt{2}\begin{bmatrix}1 & 0\\ 0 & 1\end{bmatrix}\ \ \sqrt{2}\begin{bmatrix}1 & 0\\ 0 & -1\end{bmatrix}\ \ \sqrt{2}\begin{bmatrix}0 & 1\\ 1 & 0\end{bmatrix}\ \sqrt{2}\begin{bmatrix}0 & -1\\ 1 & 0\end{bmatrix}\right\} = [S_a\ S_b\ S_c S_{\ d}]. \quad (31)$$

Similarly, reciprocity dictates that the fourth element S_d can be neglected. The scattering matrix can be expressed as:

$$S = \begin{bmatrix}S_{HH} & S_{VH}\\ S_{HV} & S_{VV}\end{bmatrix} = \alpha S_a + \beta S_b + \gamma S_c \quad (32)$$

where

$\alpha = \frac{S_{HH}+S_{VV}}{\sqrt{2}}$, (33)

$\beta = \frac{S_{HH}-S_{VV}}{\sqrt{2}}$ ' and (34)

$\gamma = \sqrt{2}\, S_{HV}$. (35)

Thus the Pauli basis vectorization of the scattering matrix S can be expressed [38]:

$$k = \frac{1}{\sqrt{2}}\begin{bmatrix} S_{HH} + S_{VV} \\ S_{HH} - S_{VV} \\ 2S_{Hv} \end{bmatrix} . \quad (36)$$

The Pauli representation has many useful interpretations and is the basis of some of the more common transformation and decomposition techniques used to analyze polarimetric data. The elements in the Pauli representation can be interpreted as single or odd bounce(S_a), double or even bounce (S_b), and volume scattering (S_c) such as one would encounter in the forest canopy. This symmetry also guarantees that any rotation through an angle θ will be the same for both the transmit and receive co-ordinate systems.

3.3.6 The Covariance Matrix C

The covariance matrix C is formed by taking the cross product of the Lexicographic vector Ω and its' conjugate transpose Ω^{*T} and taking an ensemble average of the elements in the space or time domain denoted by the ⟨ ⟩ brackets. Assuming reciprocity, we shall limit ourselves to the derivation of the three by three case. The formula for C_3 is:

$$C_3 = \langle \Omega \otimes \Omega^{*T} \rangle = \begin{bmatrix} \langle |S_{HH}|^2 \rangle & \sqrt{2}\langle |S_{HH}S_{HV}{}^*|^2 \rangle & \langle |S_{HH}S_{VV}{}^*|^2 \rangle \\ \sqrt{2}\langle |S_{HV}S_{HH}{}^*|^2 \rangle & 2\langle |S_{HV}|^2 \rangle & \sqrt{2}\langle |S_{HV}S_{VV}{}^*|^2 \rangle \\ \langle |S_{VV}S_{HH}{}^*|^2 \rangle & \sqrt{2}\langle |S_{VV}S_{HV}{}^*|^2 \rangle & \langle |S_{VV}|^2 \rangle \end{bmatrix}. \quad (37)$$

3.3.7 Coherency Matrix T

In a similar fashion to the covariance matrix, the coherence matrix T is formed by taking the cross product of the Pauli vector k and its' conjugate transpose k^{*T} and taking an ensemble average of the elements in the space or time domain denoted by the ⟨ ⟩ brackets. One again, assuming reciprocity, we shall limit ourselves to the derivation of the 3 by 3 case.

$$T_3 = \langle k \otimes k^{*T} \rangle =$$

$$\frac{1}{2}\begin{bmatrix} \langle |S_{HH} + S_{VV}|^2 \rangle & \langle (S_{HH} + S_{VV})(S_{HH} - S_{VV})^* \rangle & 2\langle (S_{HH} + S_{VV})S_{HV}{}^* \rangle \\ \langle (S_{HH} - S_{VV})(S_{HH} + S_{VV})^* \rangle & \langle |S_{HH} - S_{VV}|^2 \rangle & 2\langle (S_{HH} - S_{VV})S_{HV}{}^* \rangle \\ 2\langle S_{HV}(S_{HH} + S_{VV})^* \rangle & 2\langle S_{HV}(S_{HH} - S_{VV})^* \rangle & 4\langle |S_{VV}|^2 \rangle \end{bmatrix}. \quad (38)$$

Both the coherence T and the covariance C matrices are Hermitian positive semi-definite matrices that share the same real non-negative eigenvalues and orthogonal eigenvectors [38].

3.3.8 Other Representations of the Coherency and Covariance Matrices

In terms of defining and separating the dominant scattering mechanisms, it is useful to define the coherency matrix in an alternate form as follows:

$$[T] = k_{P*}k_P^* = \begin{bmatrix} A_0 - A & C - iD & H + iG & I - iJ \\ C + iD & B_0 + B & E + iF & K - iL \\ H - iG & E - iF & B_0 - B & M + iN \\ I + iJ & K + iL & M - iN & A_0 - A \end{bmatrix}. \quad (39)$$

Following from this definition of the coherency matrix, the Mueller Matrix can be expressed as:

$$[M] = \begin{bmatrix} A_0 + B_0 & C + N & H + L & F + I \\ C - N & A + B & E + J & G + K \\ H - L & E - J & A - B & M + D \\ I - F & G - K & M - D & A_0 - B_0 \end{bmatrix}. \quad (40)$$

If the vector theory of reciprocity is applied, the coherency matrix reduces to

$$[T] = k_{P*}k_P^* = \begin{bmatrix} A_0 - A & C - iD & H + iG & I - iJ \\ C + iD & B_0 + B & E + iF & K - iL \\ 0 & 0 & 0 & 0 \\ I + iJ & K + iL & M - iN & A_0 - A \end{bmatrix}. \quad (41)$$

The 3 by 3 coherency matrix can be expressed as follows:

$$[T_3] = \begin{bmatrix} A_0 + A & C - iD & I - iJ \\ C + iD & 2B_0 & K - iL \\ I + iJ & K + iL & A_0 - A \end{bmatrix}. \quad (42)$$

Similarly, applying reciprocity the Mueller matrix reduces to

$$[M] = \begin{bmatrix} A_0 + B_0 & C & L & I \\ C & A + B_0 & J & K \\ -L & -J & A - B_0 & D \\ I & K & -D & A_0 - B_0 \end{bmatrix}. \quad (43)$$

These definitions will prove to be useful in the following sections where the decomposition theories are explored in more detail.

3.3.9 SPAN of SAR Data

Another useful representation is the SPAN, or total power of the Scatting matrix, which can be defined using the elements of the Sinclair scattering matrix as:

$$SPAN = |S_{HH}|^2 + |S_{VV}|^2 + 2|S_{HV}|^2 . \quad (44)$$

It can also be computed from the Pauli coefficients as follows:

$$SPAN = |\alpha|^2 + |\beta|^2 + |\gamma|^2 . \quad (45)$$

Analysis cannot begin until several pre-processing steps have been performed to correct for various distortions, system noise and terrain effects that can bias the radar signal. It should be noted, that the Trace of both the covariance and coherency matrices are equal since the total power must remain constant under these transformations.

3.4 Pre-processing and Transformations of PolSAR Radar Data

3.4.1 Faraday Rotation

Satellite based radar systems are affected by Faraday rotation as the signal passes through the ionosphere [46-49]. The amount of rotation is dependent on the "total integrated electron concentration (TEC) along the radar path and its interaction with the local magnetic field vector" [50]. This effect causes the radar signal to undergo a propagation rotational transformation by an angle theta Θ which can be calculated from the data [46-50].

Table 5 - Maximum values for Faraday Rotation Angles for various wavelengths under peak TEC conditions

Band	Wavelength (cm)	Frequency	Faraday Rotation (°)
C	5. 6	4-8 GHz	2. 5
L	23. 6	1-2 GHz	40
P	68	300 MHz-1GHz	321

The Faraday rotation is wavelength dependent with longer wavelengths undergoing a larger transformation as Table 5 demonstrates [46]. Assuming all other distortions are negligible, the Faraday rotation by an angle Ω on the S scattering matrix is described by the measured matrix $[m]$ as follows [48, 50]:

$$m = \begin{bmatrix} m_{HH} & m_{VH} \\ m_{HV} & m_{VV} \end{bmatrix} = R_F \, S \, R_F = \begin{bmatrix} cos\Omega & sin\Omega \\ -sin\Omega & cos\Omega \end{bmatrix} \begin{bmatrix} S_{HH} & S_{VH} \\ S_{HV} & S_{VV} \end{bmatrix} \begin{bmatrix} cos\Omega & sin\Omega \\ -sin\Omega & cos\Omega \end{bmatrix}. \quad (46)$$

The Law of reciprocity states that S_{VH} equals S_{HV}, but after Faraday rotation, this relation no longer holds and thus can be used to calculate the Faraday rotation angle Ω as follows [50]:

$$\Omega = \frac{1}{4} \tan^{-1} \left\langle \frac{-2\,\mathrm{Re}\left(\left(S_{HV} - S_{VH} \right) \left(S_{HH} + S_{VV} \right)^{*} \right)}{\left| S_{HH} + S_{VV} \right|^{2} - \left| S_{HV} - S_{VH} \right|^{2}} \right\rangle. \quad (47)$$

Once Ω is calculated, it is straightforward to apply standard rotation matrices to the observed Sinclair matrix and correct this affect as demonstrated in equation 48 [47-50]:

$$S = \begin{bmatrix} S_{HH} & S_{VH} \\ S_{HV} & S_{VV} \end{bmatrix} = \begin{bmatrix} cos\Omega & -sin\Omega \\ sin\Omega & cos\Omega \end{bmatrix} \begin{bmatrix} m_{HH} & m_{VH} \\ m_{HV} & m_{VV} \end{bmatrix} \begin{bmatrix} cos\Omega & -sin\Omega \\ sin\Omega & cos\Omega \end{bmatrix}. \quad (48)$$

3.4.2 Terrain Induced Orientation Angle Correction

The local incident angle of the azimuthal slope of the terrain induces a transformation of both the strength and the relative phase of the radar return signal for all the polarimetric channels [51-54]. The orientation angle deflection of the scattered polarized signal θ is a function of the radar look angle ϕ, the target azimuthal slope **ω**, and to a lesser extent the range slope γ as described by the following equation 49 [54]:

$$tan\,\theta = \frac{tan\,\omega}{tan\,\gamma\,cos\,\varphi - sin\,\varphi} . \quad (49)$$

Thus the rotation of the scattering matrix S by an angle θ is described by equation 50:

$$\tilde{S} = \begin{bmatrix} cos\theta & sin\theta \\ -sin\theta & cos\theta \end{bmatrix} \begin{bmatrix} S_{HH} & S_{VH} \\ S_{HV} & S_{VV} \end{bmatrix} \begin{bmatrix} cos\theta & -sin\theta \\ sin\theta & cos\theta \end{bmatrix} , \quad (50)$$

where $\tilde{S}$ is the terrain slope augmented matrix.

Several approaches have been developed to correct for this, terrain orientation shift [51-54]. The local incident angle theta θ of the target can be calculated using a DEM with equation (49) or it can be derived from the elements of the Sinclair matrix as follows [34, 54]:

$$\theta = \begin{cases} \eta, if\ \eta \leq \pi/4 \\ \eta - \frac{\pi}{2}, if\ \eta > \pi/4 \end{cases} \quad ' \quad (51)$$

where

$$\eta = \frac{1}{4}\left[\tan^{-1}\left(\frac{-4Re(\langle(S_{HH} - S_{VV})S_{HV}^{*}\rangle)}{-\langle|S_{HH} - S_{VV}|^{2}\rangle + 4\langle|S_{HV}|^{2}\rangle}\right) + \pi\right] . \quad (52)$$

The observed Sinclair matrix can then be corrected by applying rotational matrices with the angle θ [53] using the equation:

$$S = \begin{bmatrix} S_{HH} & S_{VH} \\ S_{HV} & S_{VV} \end{bmatrix} = \begin{bmatrix} cos\theta & sin\theta \\ -sin\theta & cos\theta \end{bmatrix} \begin{bmatrix} \tilde{S}_{HH} & \tilde{S}_{VH} \\ \tilde{S}_{HV} & \tilde{S}_{VV} \end{bmatrix} \begin{bmatrix} cos\theta & -sin\theta \\ sin\theta & cos\theta \end{bmatrix}, \quad (53)$$

where $\tilde{\boldsymbol{S}}$ is the observed terrain affected scattering matrix.

For the purposes of this project, a custom script was developed to perform a correction ofthis terrain induced distortion.

3.4.3 Speckle Filtering

Radar data is susceptible to the phenomenon known as speckle which is due to constructive interference between adjacent wave fronts. Speckle noise is a major impediment to the analysis and classification of SAR images. Many techniques have been developed to reduce the effect of speckle from radar imagery [38]. Most speckle filtering approaches have some drawbacks. The spatial resolution is degraded and several inherent scattering characteristics are altered which can affect the subsequent decompositions to be performed in the analysis process [38]. Specifically the parameters of the Cloude-Pottier Entropy-Alpha decomposition are changed if an insufficient number of looks are available since the process requires an ensemble averaging. These effects include an under estimation of entropy, an over estimation of anisotropy, and an averaging of the alpha angle [38]. It is crucial that the speckle filtering of complex data be performed independently on the amplitude and phase information since averaging the complex number would fundamentally alter the scattering information. Due to the requirement of the independent averaging of amplitude and phase information, speckle filtering must be on either the three by three covariance **C** or the coherence **T** matrix [38, 55].

3.4.4 Multi-look Average Processing

A moving radar system obtains several looks at the same area because a radar pulse expands as an arc as it travels through space. This arcing behavior illuminates the area both behind and in front of the main target area. Thus, the radar system gets several looks at the same location on the ground as it travels past a point. Multi-look radar image data is formed during SAR processing by independently processing each individual radar received pulse separately for a

given area such that the image data could contain up to four individual looks in the azimuth direction[43]. Multi-look averaging combines these individual looks into one pixel and eliminates the speckle effect at the expense of azimuthal resolution [43].

3.4.5 Boxcar Speckle Filter

A boxcar filter is one of the more common approaches where an averaging window is used to detect and remove speckle from the radar image [38, 53, 56]. This average filtering has the effect of decreasing the resolution but increasing the SNR of the final product. The boxcar filter has the advantage of being straight forward to apply and use, and works well over homogenous areas but reduces the resolution and blurs edges.

3.4.6 Enhanced Lee Speckle Filter

An Enhanced Lee filter limits the aforementioned blurring effect by employing two superimposed windows of different non-square sizes where the smaller inner window is given a greater weighting[53]. This allows the filter to detect edges and build masks using sub (localized) means to protect the integrity of edge boundaries within an image [38, 53].

3.4.7 Noise Coherence Averaging

System noise can often reduce the coherency of a radar image. Testing a radar image for system and processing noise is advisable. This test is accomplished using the 3 by 3 coherency matrix to calculate a coherency factor γ as follows [34, 42]:

$$\gamma = \frac{|C_{23}|}{\sqrt{C_{22}C_{33}}} = \frac{\left|\langle |S_{HV}S_{VV}{}^{*}|^{2}\rangle\right|}{2\sqrt{2\langle |S_{HH}-S_{VV}|^{2}\rangle\langle |S_{VV}|^{2}\rangle}} \quad . \quad (54)$$

The coherence factor has an optimum value of one, which indicates that the image has a high level of coherence. The value of this coherency factor describes the level of noise present in the data and can be used to correct the elements of the coherence matrix before decomposition and analysis can begin [34, 42].

3.4.8 Decompositions

In natural systems such as forest ecosystems, multiple distributed targets exhibit a wide variety of scattering mechanisms. According to Cloude [55] these scattering mechanisms can be divided into five classes. They are as follows:

1) surface scattering,
2) low order multiple scattering from orthogonal surfaces,
3) volume scattering due to interaction with the forest canopy,
4) a combination of surface and volume scattering, and
5) anisotropic (directional) scattering due to the shape and structure such as the interaction with a single tree trunk.

It is useful to consider decomposition as a technique to extract the averaged dominant scattering mechanism within a cluster of pixels to assist in describing a target that will be invariant through changes in the radar line of sight and various other transformations.

Over the past 30 years, many types of decomposition theorems have been developed by various researchers to extract information of the multiple distributed targets present in each pixel of the radar signal [38, 55, 57-59]. The mathematical description of these techniques is extremely complex and involved and thus is considered beyond the scope of this thesis. The following will present an overview of the evolution of these techniques without delving into the actual mathematical description of these decompositions.

Lee [38] classifies decompositions into four main classes as follows:

1) Decompositions based on the dichotomy of the Kennaugh matrix (Huynen).
2) Model based decompositions (Freeman- Durden).
3) Eigen based decompositions (Cloude-Pottier).
4) Coherent decomposition of the S matrix.

Chandrasekhar[60] pioneered the work of vector radiative transfer (VRT) theory by modeling the effects on wave propagation through a cloud of random anisotropic particles. He noted that a polarized wave interacts with these scattering elements in 3 fundamental ways:

1) propagation,
2) attenuation, and
3) scattering.

He postulated that the interaction of a wave with random media could be described as a sum of the interaction of the individual elements [55].

Huynen's Ph. D. thesis[61] built upon Chandrasekhar's work and he developed the concept of extracting a single "pure" target Mueller matrix from which he could define a rank one coherency matrix and a single S scattering matrix [55]. The remainder of this extraction would be a Mueller matrix representing the remaining distributed non-symmetric targets (N-target) that would be invariant after a rotation around the radar line of sight. While insightful, the Huynen decomposition is limited by the requirement that there be a negative correlation between S_{HH} and S_{VV} scattering elements [38]. Further there are at least three unique pure target Mueller matrices that could be potentially extracted, which is less than ideal [55].

The Freeman–Durden three-component decomposition[62] was developed to classify forested ecosystem land classes based on the idea that there are three dominant scattering mechanisms in a natural forested environment [38, 62]. They are surface scattering, multiple bounce, and volume scattering. While useful at describing the physics of radar scattering, this technique is limited by the fact that the three-component scattering model is not always applicable as it assumes reflection symmetry, ($\langle S_{HH}S_{HV}^{*}\rangle = \langle S_{HV}S_{VV}^{*}\rangle = 0$, which is not always the case [38].

Coherent decompositions [38] utilize a basis set matrices (i.e. – Pauli basis set) to decompose the radar signal and neglect the effect of speckle, which can be a serious issue in natural systems with polarimetric data. Speckle filtering averages the data, which perturbs the underlying assumption of coherency. For this reason, this class of decompositions was not considered for this project.

3.4.9 Eigen-based decompositions

Eigen-based decompositions of the coherency matrix were first proposed by Cloude et al.(1996, 1999) [55, 63]. The strength of this approach lies in the fact that an Eigen decomposition is by its nature basis invariant but the results cannot be interpreted by a physical model [38]. The Eigen decomposition of the coherency matrix T_3 can be expressed as:

$$T_3 = U_3 \sum U_3^{-1} \quad (55)$$

where $\sum$ is a three by three diagonal matrix of positive real values and U_3 defines the three orthogonal unit eigenvectors [u_1, u_2,u_3] [38]. The three by three matrix $\sum$ has diagonal values that are the three related eigenvalues. The orthogonal eigenvectors each describe a scattering

mechanism while the largest eigenvalue and related vector denote the dominant scattering mechanism.

If one takes the largest eigenvalue λ_1 and the related vector u_1, a decomposed coherency matrix can be expressed [34, 38] as:

$$T_{01} = \lambda_1 u_1 u_1^{*T} = k_1 k_1^{*T} \quad (56)$$

where the target vector k_1 can be described using the generalized polarimetric parameterization defined previously as [38]:

$$k_1 = \sqrt{\lambda_1} u_1 = \frac{e^{i\varphi}}{\sqrt{2A_0}} \begin{bmatrix} 2A_0 \\ C + iD \\ H - iG \end{bmatrix} = e^{i\varphi} \begin{bmatrix} \sqrt{2A_0} \\ \sqrt{B_0 + B} e^{iarctan(\frac{D}{C})} \\ \sqrt{B_0 + B} e^{-iarctan(\frac{G}{H})} \end{bmatrix}. \quad (57)$$

The three general types of scattering mechanisms can be characterized as follows [38]:

Surface scattering: $A_0 >> B_0 + B$, B_0-B,

Dihedral scattering: $B_0 + B >> A_0$, B_0-B, and

Volume Scattering B_0 - B >> A_0 , B_{0+}B.

Building on Cloude's earlier work, the Cloude-Pottier Entropy-Alpha decomposition [64]employs an eigenvalue based analysis of the coherency matrix [38, 64]. This Eigen-decomposition of the Hermitian coherency matrix provides an orthogonal basis where each vector represents a different type of scattering mechanism[38, 64]. The strength of this approach is that it does not

rely on a predefined statistical distribution of physical canonical models [38]. Several useful rotationally invariant parameters arise from this method which aid in the description of the dominant target scattering mechanism.

3.4.9.1 Entropy (H) Decomposition Parameter

From the Eigen decomposition, it is possible to calculate a Von Neumann Entropy H by calculating the logarithmic sum of the eigenvalues of the coherency matrix [34, 38] as follows:

$$H = \sum_{i=1}^{n} -P_i \log_n P_i \quad where\ P_i = \frac{\lambda_i}{\sum_{i=1}^{n} \lambda_i} \ . \quad (58)$$

This entropy value H will have a range between 0 and 1. This value is significant in that it describes scattering characteristics of the target. If entropy is low the target is weakly depolarizing and it is possible to extract a dominant target matrix from the largest eigenvector and ignore the other Eigen components. If on the other hand the entropy is high, the target is strongly depolarizing and the full Eigen spectrum must be considered[38]. In the case where H = 1 the polarized information is zero and the signal can be assumed to be pure noise.

3.4.9.2 Alpha (α) Parameter

If we define the eigenvector u_i [34] as:

$$u_i = [\cos\alpha_i \, e^{-i\phi_i} \quad \sin\propto_i \cos\beta_i \, e^{-i(\delta_i+\phi_i)} \quad \sin\propto_i \sin\beta_i \, e^{-i(\gamma_i+\phi_i)}]^T \ . \quad (59)$$

It can be shown that under rotation around the radar line of sight the parameter alpha α will always remain invariant and is directly related to the scattering mechanism of the target [38]. The value of alpha gives the ratio of the different polarization scattering components within each pixel. Cloude et al. (2007) claimed that:

"This makes it a robust parameter for classification and parameter estimation as it is based not on local data statistics but on the physics of wave scattering" [50].

The value of alpha falls within the range of values from [0 to $\pi/2$]. When alpha equals 0 the dominant mechanism is a Bragg surface scattering such as over water. An Alpha value of $\pi/4$ indicates a dipole scattering whereas when alpha equal to $\pi/2$, indicates the scattering mechanism of a dihedral target [34, 38].

3.4.9.3 Anisotropy

If we define the eigenvalues as $\lambda_1 > \lambda_2 > \lambda_3 > 0$ then polarimetric Anisotropy can be defined [34] as:

$$A = \frac{\lambda_2 - \lambda_3}{\lambda_2 + \lambda_3}. \quad (60)$$

Anisotropy is useful when Entropy is high (> 0.7) but decreases in importance as the value of λ_2 and λ_3 become smaller and are increasingly affected by signal noise [38].

3.4.9.4 Single (and Double) Bounce eigenvalue Relative Difference (SERD and DERD)

This Eigen-based parameter was proposed by Allain [38], and leverages assumptions of natural system targets, in which the correlation between co-polar and cross-polar channels is zero. Allain defines three non-ordered size (NOS) eigenvalues and calculates an alpha parameter for each of these eigenvalues. If the associated alpha is less than or equal to $\boldsymbol{\pi}/4$ it is considered single bounce (α_S and λ_s) and if greater than or equal to $\pi/4$ it is double bounce (α_D and λ_D). He then defines the following two relations [38] as follows:

SERD = $\frac{\lambda_S - \lambda_{NOS3}}{\lambda_S + \lambda_{NOS3}}$, and (61)

DERD = $\frac{\lambda_D - \lambda_{NOS3}}{\lambda_D + \lambda_{NOS3}}$ (62)

These parameters which have a range of values from -1 to +1 are useful in discriminating natural systems providing more unique information than is present within the Entropy or Anisotropy parameters alone [38].

3.4.9.5 Shannon Entropy

Shannon entropy SE is the sum of the contributions to the entropy by both intensity and degree of polarization [38]. It is useful as a discriminator in that it directly relates the degree of randomness to the intrinsic degrees of coherence [65]. This provides a unique parameter which can be useful in discriminating between various scattering targets.

3.4.9.6 Polarization Fraction

The polarization fraction is defined [38] as follows:

$$PF = 1 - \frac{3\lambda_3}{\lambda_1 + \lambda_2 + \lambda_3}. \quad (63)$$

If λ_3 is 0, then the return is completely polarized, and then as the value of λ_3 increases the polarized fraction decreases [38].

3.4.9.7 Polarization Asymmetry

Polarization Asymmetry is a measure of the ratio of the sum and difference of the two eigenvalues of the polarized return [38]. Polarization Asymmetry is defined as follows:

$$PA = \frac{\lambda_1 - \lambda_2}{\lambda_1 + \lambda_2 - 2\lambda_3} \text{ .(64)}$$

3.4.9.8 Radar Vegetation Index

Radar vegetation index is defined by the following equation:

$$RVI = \frac{4\lambda_3}{\lambda_1 + \lambda_2 + \lambda_3} . \text{ (65)}$$

The radar vegetation index has an inclusive range of values from [0 to 4/3] The value of the radar vegetation index increases as the size of the trees increase[38].

3.4.9.9 Pseudo Probabilities (P_1, P_2, P_3)

The Pseudo probability P_N is defined as the ratio of an eigenvalue divided by the sum of all the eigenvalues:

$$P_N = \frac{\lambda_N}{\lambda_1 + \lambda_2 + \lambda_3} . \text{ (66)}$$

3.4.9.10 Pedestal Height

The pedestal height is a measure of a randomness of the scattering processes. It is defined as:

$$PH = \frac{\lambda_3}{\lambda_1} . \text{ (67)}$$

3.4.9.11 Beta (β), Delta (δ), Gamma (γ)

The previously presented eigenvector u_i definition was:

$$u_i = [\cos\alpha_i \, e^{-j\phi_i} \quad \sin\propto_i \cos\beta_i \, e^{-j(\delta_i + \phi_i)} \quad \sin\propto_i \sin\beta_i \, e^{-j(\gamma_i + \phi_i)}]^T \quad (68)$$

and also defines three additional parameters Beta (β), Delta (δ), and Gamma(γ). It should be noted that that these decomposition parameters, unlike Alpha, are roll variant and can provide information on the polarization orientation angle of the target [38], p. 234].

3.4.9.11 Epsilon (ε) and Nu (ν) Decomposition Parameters

If we consider the special case of the scattering matrix of a group of anisotropic particles, which can be described as:

$$S = \begin{bmatrix} a & 0 \\ 0 & b \end{bmatrix}. \quad (69)$$

A rotational matrix by an angle θ is defined as:

$$R(\theta) = \begin{bmatrix} 1 & 0 & 0 \\ 0 & cos2\theta & sin2\theta \\ 0 & -sin2\theta & cos2\theta \end{bmatrix}. \quad (70)$$

A coherence matrix rotated by θ can be defined as:

$$T(\theta) = R(\theta) \begin{bmatrix} \varepsilon & \mu & 0 \\ \mu^* & \nu & 0 \\ 0 & 0 & 0 \end{bmatrix} R(\theta)^{-1}, \quad (71)$$

where

$$\varepsilon = \frac{1}{2}|a+b|^2, \quad (72)$$

$$\nu = \frac{1}{2}|a-b|^2, \text{ and } \quad (73)$$

$$\mu = \frac{1}{2}(a+b)(a-b)^*. \quad (74)$$

Integrating the rotated coherency matrix from 0 to 2π provides:

$$\langle T(\theta)\rangle = \int_0^{2\pi} T(\theta)P(\theta)\,d\theta = \frac{1}{2}\begin{bmatrix} 2\varepsilon & 0 & 0 \\ 0 & \nu & 0 \\ 0 & 0 & \nu \end{bmatrix}. \quad (75)$$

If a single scattering mechanism dominates, then it can easily be identified from the following three cases:

Table 6 - Relationship between scattering mechanism and eigenvector decompositions

Scattering Mechanism	A and B Relationship	eigenvector
Dihedral Scattering	a = -b	$[\,0\ 1\ 0\,]^T$
Dipole scattering	a>>b	$[\,0.707\ 0.707\ \ 0\,]^T$
Surface Scattering	a = b	$[\,1\ 0\ 0\,]^T$

These averaged Epsilon (ε) and Nu (**ν**) are thus rotationally stable and can be used to define the physical characteristics of a given target [38].

3.4.9.12 Combinations of Entropy (H) and Anisotropy(A)

The polarimetric radar software-processing package POLSARPRO offers a selection of decomposition parameters that are non-linear combinations of Entropy and Anisotropy. These parameters include the following combinations [66]:

1) (1-H)*A. (76)
2) (1-A)*H. (77)
3) (1-H)*(1-A). (78)
4) H*A. (79)

Large H*A values correspond to A and H values and indicate two dominant scattering mechanisms with two related dominant eigenvalues and vectors. A large value for either H*(1-

A) or (1-H)*A or (1-H)*(1-A) indicates no dominant eigenvalue and implies a random scattering target [66].

3.4.9.13 Luneburg Anisotropy

Luneburg Anisotropy is defined as [67]:

$$LA = \sqrt{\frac{3}{2}}\sqrt{\frac{\lambda_2^2 + \lambda_3^2}{\lambda_1^2 + \lambda_2^2 + \lambda_3^2}} \quad (80)$$

where LA has valid values between [0 , 1] inclusively. Luneburg Anisotropy is an index-based measure that uses the second and third eigenvalues (which represent volumetric and anisotropic scattering) to assist in describing a scattering target. This can be useful as entropy increases in mature forest stands.

3.5 Geolocation and Orthorectification

The final step in the preprocessing of the radar data consists of transposing the data into a geo-referenced domain to correct for terrain effects and for analysis with Geographic Information Systems (GIS) data sets. This step is generally performed using a Digital Elevation Model (DEM) and orbital parameters to generate a synthesized SAR intensity image[68]. Ground control points (GCP) can then be collected by comparing the two images. Another important step in this process is to use the DEM to calculate shadow and layover effects created by the side looking nature of radar. Once identified, the shadow and layover areas in the geo-located radar image must be masked and excluded from further analysis. An open source software package, Map Ready (built by the Alaskan Satellite Facility (ASF)) is an example of software designed to perform this task [69].

The algorithm uses a DEM and orbital parameters to generate a simulated SAR image to use in the transformation. The side looking nature of satellite radar systems is complicated in mountainous regions where effects known as shadow and layover can occur [38]. Shadowing occurs when the back slope of a mountain is steeper than the radar look angle and thus is not visible to the radar system [38].

Layover occurs when the front slope of a mountain with respect to the radar system is steeper

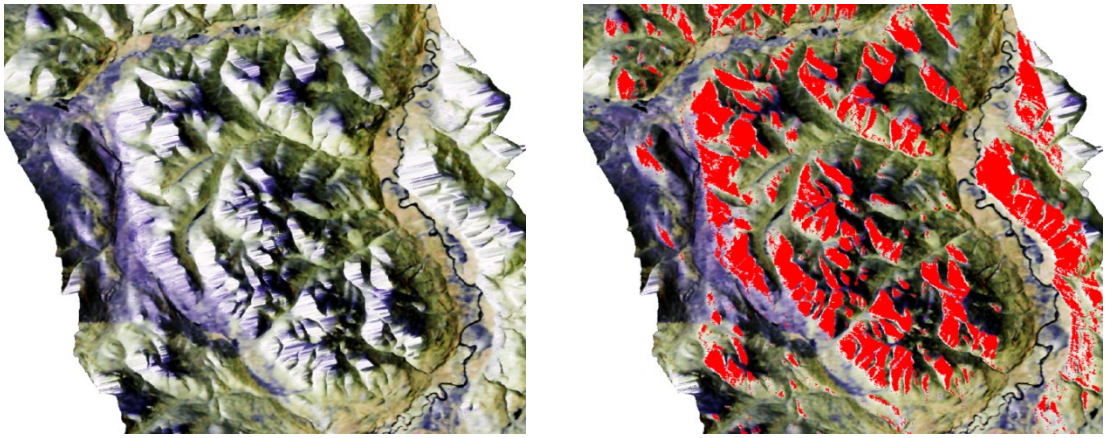

Figure 11 - PALSAR Blue Sheep Creek Alpha, Entropy, Lambda2&3 HSV decomposition image that has been geolocated on left while the image on the right displays the same image with a red shadow /layover mask in overlaid. All of the data under the mask must be excluded from analyses.

than the radar look angle [38]. In this case the top of the mountain appears to be closer to the sensor than the bottom of the mountain and it is impossible to correctly locate these pixels within a geo-located image. In both the cases of shadow and layover, the solution is to generate a mask for both areas and exclude those pixels from analysis. The open source software tool ASF MapReady will generate these masks as a by-product of the geo-location process [69].

3.6 Visualizations

3.6.1 Alpha, Entropy, Lambda as Hue, Saturation, and Value

Shane Cloude et al.(2007) [50] have developed a technique to improve visualization of natural forested ecosystems for topologically challenging areas [50]. The three input channels are Alpha, Entropy, and eigenvalues Lambda (λ_2+ λ_3) using a Hue-Saturation-Value (HSV) model to create an image. The Alpha channel is used to generate a hue value, starting with low Alpha values as blue, green for medium Alpha values, and increasing to red for higher values [50]. Entropy is used as the saturation variable, hence strongly depolarizing areas appear as either black or white [50]. The value channel is generated using the sum of the smallest eigenvalues λ_2+ λ_3 which reduces the amplitude modulation due to topographic effects [50]. This technique provides a useful tool to identify various features in forested areas. Polarized returns are black identifying open areas and water features. The boreal forest areas appear as green (with L-Band) due to the dominance of dipole scattering within the vegetation canopy. Recently burned areas appear as blue (with L-Band) since there is low entropy and low alpha values. Figure 11 is an example of Cloude et al.(2007) [50]Alpha, Entropy, and Lambda HSV visualization.

3.6.2 Pauli Visualization

The Pauli vector discussed in Section 3.3.6.1 is used to generate a visually appealing RGB image. The red channel is represented by HH+VV while the green and blue channels are created using HH-VV and 2HV respectively [50]. These channels correspond to the elements of the Pauli vector and coincidentally the diagonal elements T_{11}, T_{22}, T_{33} of the coherency matrix [38]. Theoretically they represent single bounce for HH+VV, double bounce for HH-VV and 45° rotated double bounce for 2HV [70].

3.6.3 Freeman-Durden Image Visualization

The Freeman-Durden decomposition is used to create another useful visual interpretation of Polarimetric radar images in forested ecosystems. The three parameters generated by the Freeman-Durden decomposition are single bounce related to surface scattering, double bounce related to ground tree trunk reflections, and volume scattering from the canopy [38]. These three components are used (double, volume, and single scattering) to represent the RGB channels of the image respectively. Hence, open areas and water are blue, closed forested areas are green and more open forested areas and urban environments are red [71].

3.6.4 Entropy-Alpha Plane

The entropy alpha plane is a useful representation of the main roll invariant Cloude-Pottier decomposition parameters. The plane can be divided into 9 areas each representing a unique

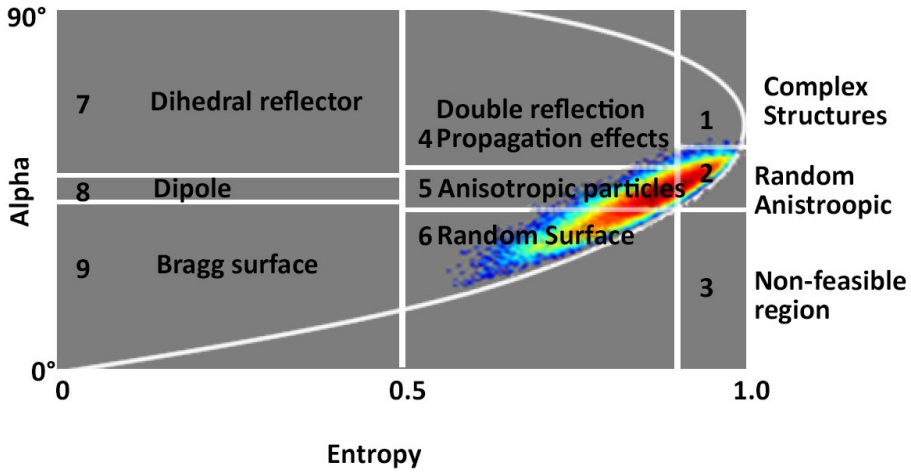

Figure 12 - Entropy-Alpha Plane Graph of Mature Forest. Each of 8 feasible regions in the plane represent a different type of scattering target allowing for a physical interpretation of the target's physical characteristics.

type of scattering target. Figure 12 demonstrates the power of this classification to aid in the discrimination of various scattering mechanisms of given targets.

4.0 Computer Systems, Data Flow and Software Environment

To complete this project a diverse set of software tools was required to:

1) Acquire relevant data,
2) Pre-process the data, and
3) Analyze the data.

This chapter will guide the reader through all of these steps and describe the software used to accomplish the given tasks.

4.1 Introduction

A large amount of data (~ 5TB) was employed as input for this project. A total of 18 quad-pol ALOS – 1 PALSAR images and six quad-pol Radarsat-2 images were selected for this investigation. DEMS for the entire study area were required for the orthorectification. Landsat optical data were acquired for NBR and dNBR calculations for each fire event. Landsat data were used for visualization and validation of the orthorectified Radar images. Polygonal GIS data of the historic wildfire events also were required for selection validation and verification phases of the project.

Each one of the 24 raw quad-pol images contains four complex floating point channels of data. Processing each one of these images requires four intermediate stages where the data storage requirements increase tenfold before even beginning to perform the decompositions into the 65 different products. Next these 65 products needed to be orthorectified.. This does not include the testing of various filters and visualizations that were also investigated. Analysis, and classification and modelling products increased storage requirements further. In total over five Terabytes of data were generated for this project which challenged the limits of computing

systems especially when this project began in 2008. The following sections will describe in detail the complete data process from acquisition to fire mapping products.

4.2 Software

A large selection of open source and proprietary software was used for this project. The following is a brief description of all the various software tools that were used.

POLSARPRO [72] was used to unpack, transform, apply speckle filters and to generate decomposition parameters, and classifications for PALSAR imagery. It was also used to generate Entropy/Alpha and Entropy/Anisotropy graphs [72]. POLSARPRO is described as a

> "Polarimetric SAR Data Processing and educational tool that aims to facilitate the accessibility and exploitation of multi polarized SAR data sets … with the objective to provide a tool for self education … and a comprehensive suite of functions for SAR data analysis" [72].

POLSARPRO provides tools for SAR data extraction, basis conversion, speckle filtering, various decompositions, classifications, and image generation. POLSARPRO provides tools for interferometric SAR analysis as well. POLSARPRO is an open source project developed under the GNU General Public License V2 with contributions from various governmental organizations and universities including ESA, Natural Resources Canada, NASA, the Alaska SAR Facility, JAXA, and the U.S. Naval Research Laboratory. POLSARPRO runs on various Windows, Linux and Macintosh operating systems. POLSARPRO provides a GUI interface to run the underlying code (which is written in C) and individual executables can be executed from the command line or from custom designed scripts.

The **Radarsat2 Toolbox** (RSTB) [73] was used for data extraction, basis transformation, to apply speckle filters, to generate decomposition parameters, to apply terrain corrections and to orthorectify Radarsat-2 imagery.. Radarsat2 Toolbox was developed by Array Systems Computing Inc. under contract from the Canadian Space Agency (CSA) in collaboration with the Canadian Forest Service and the Geological Survey of Canada (GSC). The objective was to provide an open source toolbox for processing visualizing, and analyzing Radarsat2 SAR Products to maximize the utilization of Radarsat2 data. The Radarsat2 toolbox was built using the next ESA SAR toolbox (NEST) application programming interface (API). This toolbox provides tools to perform data extraction, basis conversions, speckle filtering, radiometric correction due to atmospheric and topographical influences, speckle filtering, image orthorectification, and image classification and analysis. While not used in this project, the Radarsat2Toolbox also provided interferometric tools for Radarsat2 data analysis. NEST and the Radarsat-Toolbox were developed under the GNU General Public License V2. They are written in Java and can be used on various Windows, Linux, and Macintosh operating systems.

ASF MapReady [69] Remote Sensing Toolkit was employed to apply terrain corrections and orthorectify the decomposition parameters generated from the PALSAR data. Shadow and layover masks were generated using the MapReady toolkit.. MapReady was developed by the Alaska SAR Facility to provide tools data extraction, radiometric and terrain correction, image orthorectification, and polarimetric decomposition for level one SAR data. MapReady is distributed free of charge under the specific licensing terms of ASF with or without modification. The underlying source code is written in C and C++ and the GUI can be run on both Windows and Linux operating systems while the executables theoretically can be run on Macintosh operating systems but are not specifically supported.

Statistica [74] was used for statistical analysis, including multiple linear regression of the decomposition parameters for the purpose of identifying the most significant factors for describing boreal forest age for modelling.. Statistica is a proprietary software package created by StatSoft which has recently been purchased by Dell. Originally released in 1986, Statistica has continued to grow and evolve with version 12 released in 2013. It is described as a numerical analysis package that provides tools for data analysis, data management, statistics, data mining and visualization. The licensing is proprietary and no information is available regarding the source code implementation, although an API is available to access objects for scripting in languages such as R, Java, Visual Basic, and C#.

ENVI/ IDL [75] was used to build batch scripting routines for generating dNBR burn maps, data extraction and model application to generate forest age maps. These tools were also used for visualization, statistical analysis and data manipulation. IDL stands for interactive data language. It was released by Research Systems Inc (RSI) in 1979 and ran on PDP-11 computer systems. Two years later a VAX-11 Macro and FORTRAN version was released. In 1987, a C version of IDL was released for providing cross platform for accessibility to modern PC based operating systems. ENVI which stands for Environment for Visualizing Images was built using IDL and released in 1994. It was specifically designed for geospatial applications in remote sensing. ENVI and IDL leverages several large scientific computing libraries including BLAS (Basic Linear Algebra Subprograms) and SCALPAC (SCAlable Linear Algebra PACkage) developed by the Oak Ridge National Laboratory, thus providing multithreaded computing for enhanced performance. One of the major advantages of IDL and ENVI is that it supports matrix algebra equations which it processes in a multithreaded model. IDL also provides a command line interpreter which facilitates streamlined code prototyping and debugging.

ESRI's ArcInfo [76] was used for visualization, quality control and figure generation of intermediate and resultant products. The ESRI **Arcpy** python module routines were used for batch processing of ancillary data sets such as the NFDB data ESRI stands for Environmental Systems Research Inc. ArcINFO is one application of a family of Geographic Information Systems (GIS) products that can be used for spatial analysis and visualization of both vector and raster based data. The most current desktop version is 10.4 and runs only on a minimum of Windows 7 SP1 operating systems. The python Arcpy module – developed by ESRI - allows for direct access to a scripting API of the ARC objects with Python 2.7.

PCI Geomatica [77]and PCI's scripting language **EASI** [77] was used for visualization, quality control, classifications, orthorectification, mosaicking, statistical analysis, and file manipulation of various ancillary and radar decomposition datasets. PCI Geomatica is a proprietary desktop software application for remote sensing and is distributed by PCI Geomatics Inc., which was founded in 1982. The current version of the core visualization application is Geomatica 2014. It provides a scripting API called EASI that allows for command line functionality and batch processing capabilities, which is supported by modern Windows operating systems of 7 or greater. The original concepts for the software application were created at the Canada Centre for Remote Sensing (CCRS) in the 1970s.

GoogleEarthPro [78]was used as a visual reference aid in selecting PALSAR and Radarsat2 imagery. GoogleEarthPro is a virtual GIS mapping system that automatically drapes modern satellite imagery on 3-D model of earth by default. Originally developed by Keyhole Inc, it was acquired by Google in 2004. Unlike the freeware version GoogleEarth, the pro version allowed for the loading of both raster and vector based imagery into the application which facilitated the selection of candidate images in an expeditious manner. GoogleEarth is supported by Windows,

Linux and Macintosh operating systems running a minimum of a Pentium III processor 500 MHz with at least 256 MB of RAM.

The free statistical programming language **R** and in particular the **glmutil** package [79] was used to investigate quality of various models built using the decomposition parameters [80]. R is an implementation of the statistical programming language S developed at Bell Labs by John Chambers. R is distributed under the GNU General Public License V2 and was written in C and FORTRAN. Like IDL, R provides matrix arithmetic functionality and a command line interpreter, which allows for fast code development and powerful debugging capabilities. The Comprehensive R Archive Network (CRAN) provides access to over 5800 user created packages with over 120,000 functions. The glmulit package, which stands for General Linear Model Utilities was written by Vincent Calcagno and performs "automated model selection and model averaging… generating all possible models under various user constraints and finds the best model in terms of a specified information criteria using a genetic algorithm". Glmutil depends upon seven other R packages in the CRAN repository.

Mathwork's **Matlab** [81] was utilized to generate scripts to handle high level matrix manipulations of the radar data such as correcting coherence noise, Faraday rotation and terrain induced distortions. Matlab stands for matrix laboratory, and was originally conceived in the 1970's by Cleve Moler as an educational tool at the University of New Mexico. It is fourth generation programming language that supports matrix arithmetic and provides a command line interpreter like both IDL and the R programming language. Matlab is written in C and distributed by MathWorks as a proprietary software product. Matlab runs on all modern Windows, Linux, and Macintosh operating systems. Matlab leverages the LAPACK (Linear Algebra Package) libraries designed to exploit modern cache-based computing systems.

Microsoft Office Excel [82] was used for data manipulation, statistical analysis and image generation of results. Excel 2003 and 2010 are licensed as a proprietary software product of Microsoft Corp. and run solely on windows based operating systems.

Custom scripts in **R, Python**, **EASI, IDL**, **C and C++** were developed within the CFS Advanced Forest Technologies group and by the author. These scripts were used to perform noise coherence averaging, data extraction, statistical analysis, and generating batch scripting routines.

4.3 Image Acquisition Process

Radar image acquisitions were made in two ways but in both cases the first step is to identify potential areas of interest. The NFDB, the Alberta historical fire data, and the satellite scene footprint data sets - in the form of polygonal GIS ESRI shape files - were viewed both within ESRI's ARCMap and GoogleEarthPro where potential areas of interest were identified. Next data could either be requested for acquisition or the archive could be searched to identify previously acquired candidate images. For this project both methods were used to obtain imagery. In the case of PALSAR data all scene requests were made through the Alaskan Satellite Facility (ASF). The requests were made by supplying a list of possible scenes (locations) and the desired mode of acquisition. This request had to fall within the parameters of the predefined satellite acquisition schedule. ASF then prepared a proposed acquisition schedule based on client requests which was forwarded to the Japanese Space Agency (JAXA) who ultimately decided

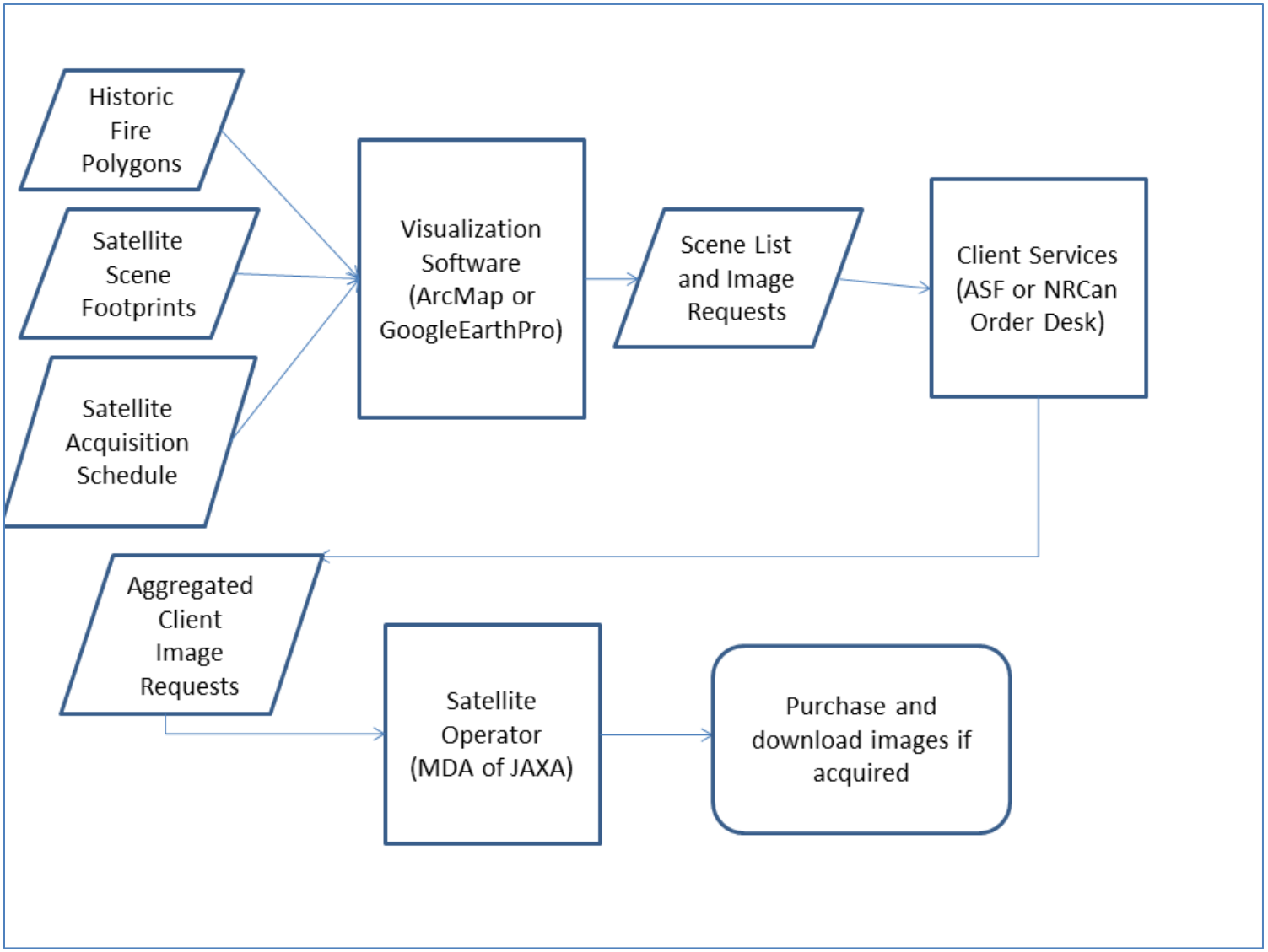

Figure 13 - Radar Image Acquisition Process

which scenes would be acquired. The Radarsat-2 requests were made in a similar fashion with the Natural Resources Canada Radarsat Order Desk acting as the coordinator between the clients and the satellite operator, Macdonald Dettwiler Associates (MDA). If all went well, the requested scenes were acquired when not pre-empted by higher priority acquisitions. As previously noted, the image archives could be searched for previously acquired images over the study areas but only a very few scenes were available in this manner. Ultimately if the images became available, they could be purchased and downloaded. Figure 13 presents a graphical interpretation of this process for clarity.

4.4 PALSAR Pre-processing

Once the images were acquired, a complex system of pre-processing steps was performed to generate geolocated decomposition images, along with shadow and layover masks where required in topographically challenging areas. Figure 14 displays the processing methodology that was applied to the PALSAR images. Over the course of this project a wide variety of computing systems both Windows and Linux-based were used for processing. The Windows-based systems included both XP 32 bit and more recently in Windows 7 64 bit systems. The Linux system used was Scientific Linux 5.1.4 known as Boron. All of the software packages used for this project were compatible with both the Windows and Linux systems unless otherwise noted.

Both PALSAR and Radarsat-2 radar data were delivered in a compressed format that required extraction before they could be used. ESA's POLSARPRO was used for the POLSAR images while the Radarsat-2 Toolbox was used for the Radarsat-2 images. This extraction process could take anywhere from 5 to 30 minutes depending on the system being used.

Once extracted the data was converted to the four by four covariance matrix usin Equation 37 for further processing using a modified version of a custom script developed by the Advanced Forest Technologies (AFT) group at the Pacific Forestry Centre (PFC) of the Canadian Forest Service (CFS) based on the direction of Dr. Shane Cloude and Dr. David Goodenough. Appendix B presents a basic version of this script. This script performed three main functions;

1) Estimated noise and the coherence (and corrected the data based on this estimate as discussed in Section 3.4.7,
2) Calculated and corrected for the Faraday rotation as described in Section 3.4.1, and
3) Performed a terrain induced polarization angle shift correction as discussed in Section 3.4.2.

This process could take anywhere from 30 minutes to 2 hours per image depending on the computer system being used.

Once all of the corrections had been applied it was then possible to perform speckle filtering on the single-look data. An enhanced Lee speckle filter (Section 3.4.6) was applied to the images based on a seven by seven and three by three moving window pair. The enhanced Lee filter was selected due to its ability to preserve the edges within the data. This process required anywhere from 15 minutes to over an hour per image depending on the system being used. The filtering for PALSAR images was performed using ESA's POLSARPRO software The Radarsat-2 data was processed with the Radarsat Toolbox software package using a Windows based system since this software was specifically optimized for Radarsat-2 data.

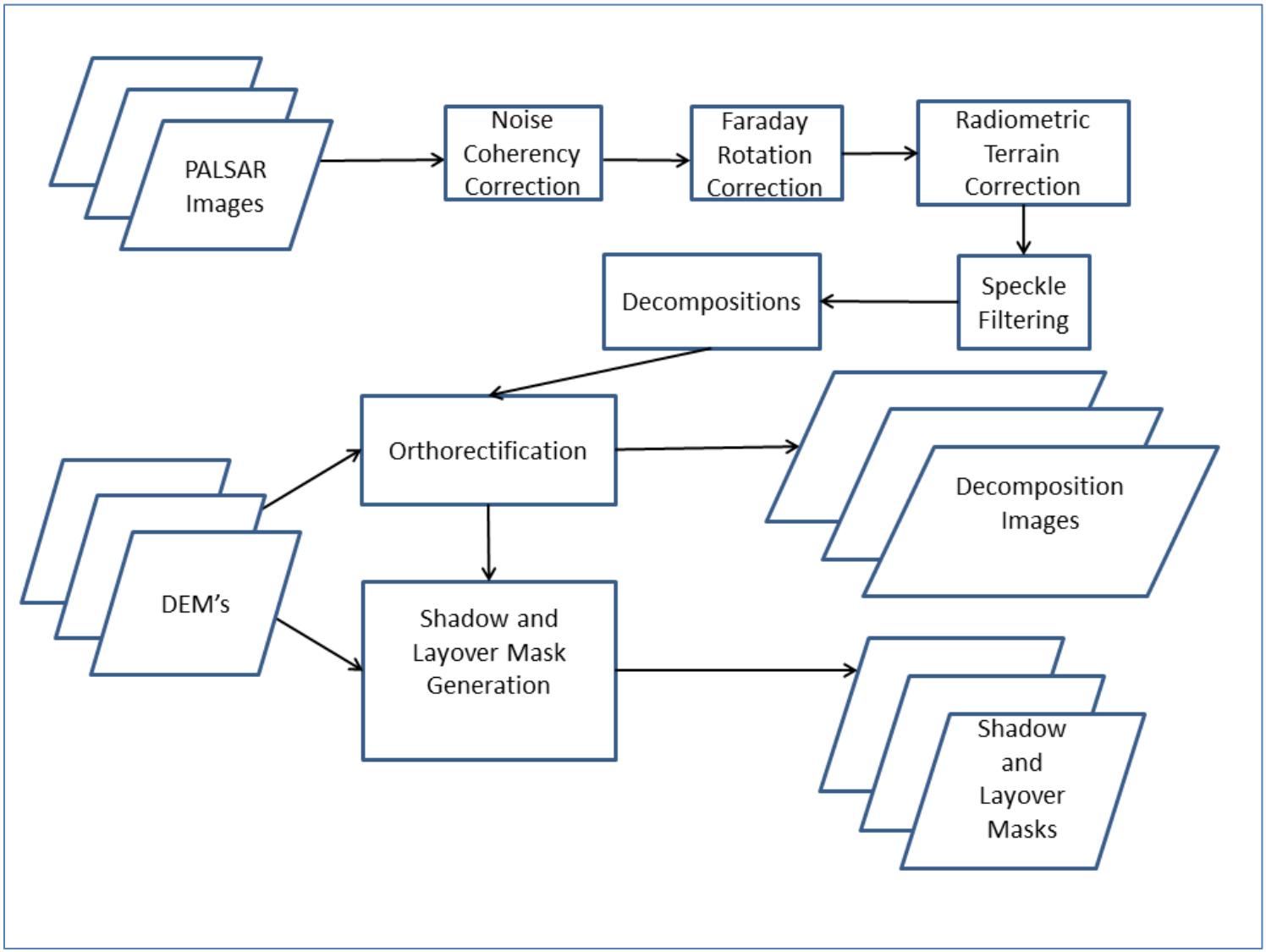

Figure 13 - PALSAR Processing Chain used for this project. Noise coherency and correction of Faraday rotation and shadow and layover masks.

Once the filtering was complete, the previously discussed polarimetric decompositions could be performed. The PALSAR images were decomposed using the POLSARPRO software whereas the Radarsat-2 images were processed with the Radarsat Toolbox in a Windows-based system. It should be noted that the Radarsat Toolbox only offered a limited set of decomposition parameters in comparison to the POLSARPRO software package.

The final step in the pre-processing involved generating geolocated, orthorectified decomposition images as well as shadow and layover masks so that a random sample of points within known fire events could be obtained. The Windows-based ASF MapReady software package was used for PALSAR images while the Radarsat Toolbox was used for the Radarsat-2 mages. The process required a DEM as an input. In the case of the Radarsat Toolbox these DEM's were automatically downloaded. For the MapReady process these DEM's needed to be downloaded, mosaicked together, and transformed to a UTM projection and a WGS84 datum with square pixels for the process to run correctly. The windows based PCI Geomatics software package was used for the mosaicking and reprojection for the DEM preparation.

Multiple python scripts were developed to automate and semi-automate the processing wherever possible using native system calls to the built in functions in POLSARPRO and the ASF MapReady radar software processing tools.

4.5 Sample Selection

In order to identify the best parameters for the discrimination of dated historical wildfire events it was crucial to select stable points within known fire events with a sufficient buffer so as to accommodate the ensemble averaging that is performed during the speckle filtering/ multi-look step of pre-processing stage for the radar images. The sample selection process was further

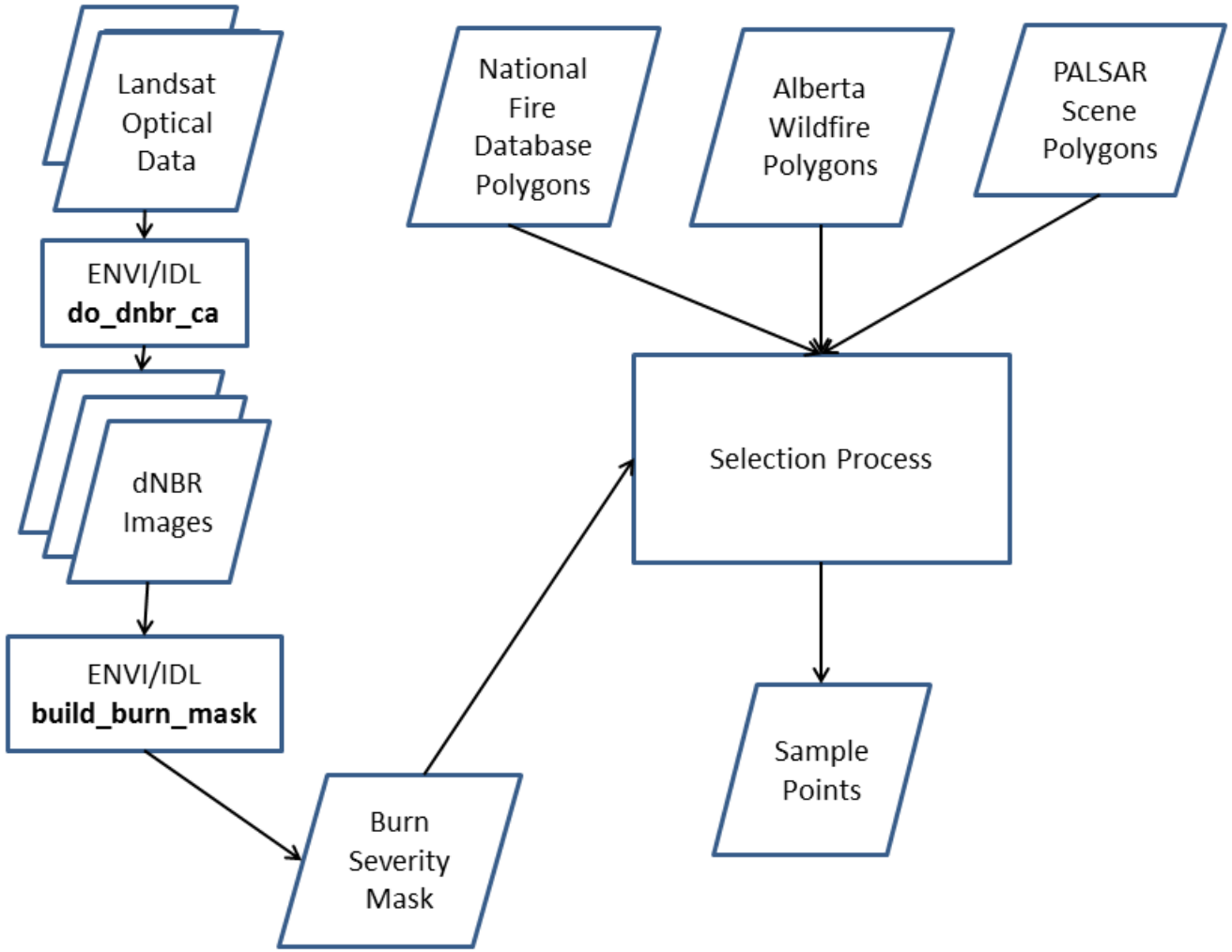

Figure 14 - Sample Point Selection

complicated due to the dynamic nature of wildfire events. The level of burn severity within an individual event can vary widely within a few 100 m due to factors such as terrain, fuel load, moisture levels and micro-climate.

Sample points were selected based on a demonstration of high burn severity by using a combination of optical data from the CFS Landsat BAP dataset and yearly dNBR indexes. The CFS National Fire Database and Alberta the fire polygons were employed to guide the sample point selection, for wildfire events prior to the launch of Landsat-4 in 1984 when no optical data was available. Due to the nature of the selection process not all of the available PALSAR images provided an acceptable set of sample points and were excluded from further analysis.

Appendix C and D present ENVI/IDL code that was used to generate NBR, and dNBR indices from optical BAP data that was used to assist in the sample point selection process. Figure 14 presents the process workflow employed for the sample selection phase of the project.

4.6 Analysis, Classification, and Modeling Methodology

Once a set of sample points was selected for analysis, a custom script extracted the decomposition values for a PALSAR scene from all of the decomposition products produced in the preprocessing stage. These samples were then analyzed using several different software packages include Statistica, Microsoft Excel and R to identify those decomposition parameters with the highest correlation with respect to the year of the wildfire event. All of these processes were performed with a Windows-based environment. The justification for using the different software packages was because each one provided unique results and confidence matrix providing a more complete picture for this phase of the analysis. Initial analysis has focused on identifying historical fire scars within various PALSAR images and extracting the average values

of various decomposition parameters from these wildfire events. These values were then analyzed using linear regression with respect to the year in which the wildfire event occurred. The challenge has been to invert these correlations to obtain an estimated date of ignition for

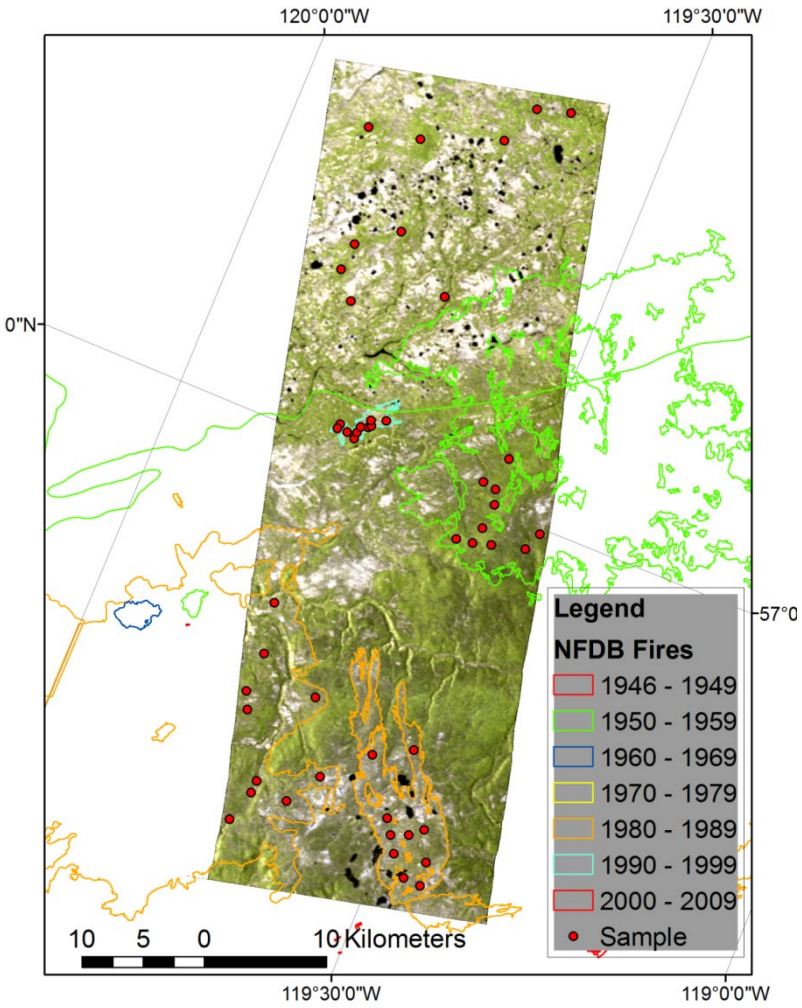

Figure 15 - Geolocated PALSAR Alpha, Entropy, Alpha HSV image acquired on May 15, 2009. The image has been generated using a Hue, Saturation, Value colour mapping respectively to Entropy, Alpha(1) and Lambda 2 plus 3 decomposition parameters of the Cloude-Pottier Entropy –Alpha decomposition. Sample points used for analysis are denoted in red. Alberta fire polygons are overlaid on the image.

these fire events. This problem is created by the variability within an individual fire event and is probably due to the range of severity occurring within the forested environment by the dynamic

processes of the wildfire event. The goal was to identify a unique independent set of parameters that can both detect and provide a reasonable estimate of the age of a wildfire event.

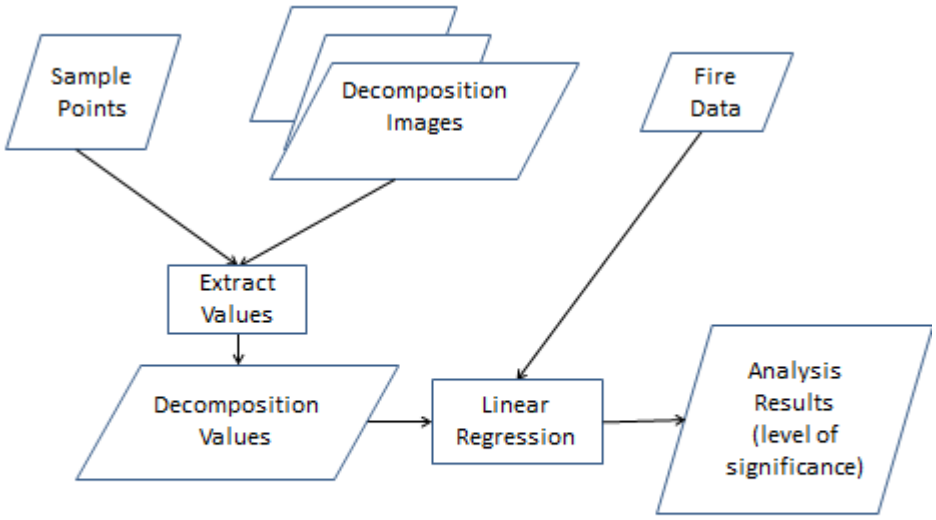

The Figure 16 - Analysis Phase Process Steps

The most significant decomposition parameters were identified with respect to the wildfire age, from the linear regression analysis. These significant decomposition parameters were then used as input channels for both a parametric Maximum Likelihood Classification (MLC) using PCI and a non-parametric LOGIT classifiers written in Fortran which could be run within PCI's EASI scripting environment.

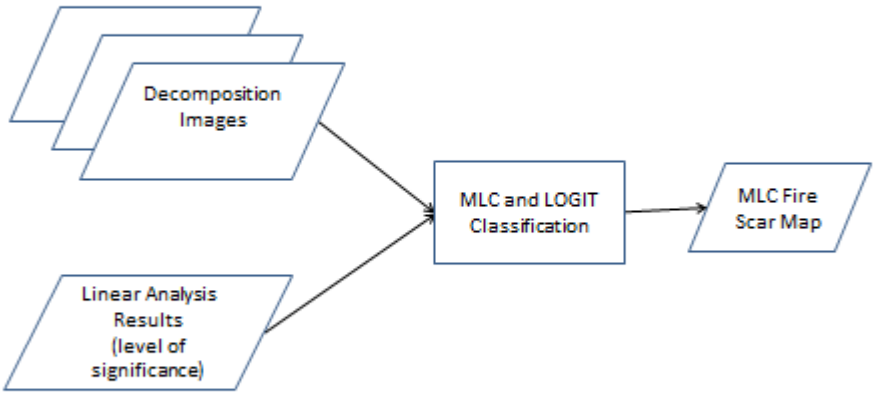

Figure 17 - Classification Process Flow to Create Fire Scar Map

5 Methodology and Analysis Results

Once the radars scenes were processed, the first step was to select the optimal datasets for further analysis, which will be the focus of the beginning of this chapter. Next, several different experiments were performed to address issues such as correlation to observed burn severity, and the importance of seasonality image of acquisition. The first phase of analysis focused primarily on the L-Band PALSAR data decompositions with respect the date of historic wildfire within individual images. Finally the potential of Canada's C-Band Radarsat-2 full polarimetric fine view acquired data will be tested using 6 temporal images of the 2002 Keg River fire. Since each image is unique with respect to the targets available and hence the exact method of interrogation that can occur, it was decided for clarity to co-locate the methodology and results together for each image experiment. It is the author's hope that this presentation approach will be easier to for the reader to assimilate**.**

5.1 PALSAR Scene Acquisition

The following PALSAR scenes were acquired in the study area to be used for analysis as displayed in Table 7. These images were selected based on their location with respect to the Chinchaga fire event and more recent fires to provide a dynamic range of fire events for sampling. Figure 12 displays the footprint of the 18 PALSAR images that are listed in table five.

Table 7 - PALSAR Image Summary

ID	Scene Id	Incidence Angle	Date of Acquisition	Scene Centre Latitude	Scene Centre Longitude	Mode
1	ALPSRP062601190	21.5	Mar 29,2007	59.376	-112.555	Quad-pol
2	ALPSRP147501140	23.1	Oct 30,2008	56.982	-120.779	Quad-pol
3	ALPSRP167631140	21.5	Mar 18,2009	56.937	-121.132	Quad-pol
4	ALPSRP167921150	21.5	Mar 20,2009	57.424	-117.051	Quad-pol
5	ALPSRP168651150	21.5	Mar 25,2009	57.423	-118.665	Quad-pol
6	ALPSRP169381140	21.5	Mar 30,2009	56.937	-120.055	Quad-pol
7	ALPSRP170401150	21.5	Apr 06,2009	57.427	-117.59	Quad-pol
8	ALPSRP171131210	21.5	Apr 11,2009	60.343	-120.568	Quad-pol
9	ALPSRP171131220	21.5	Apr 11,2009	60.828	-120.807	Quad-pol
10	ALPSRP171711140	21.5	April 15, 2009	56.941	-110.392	Quad-pol
11	ALPSRP174921180	23.1	May 07,2009	58.934	-113.016	Quad-pol
12	ALPSRP175361150	23.1	May 10,2009	57.472	-118.278	Quad-pol
13	ALPSRP176091160	23.1	May 15,2009	57.961	-120.086	Quad-pol
14	ALPSRP176091140	23.1	May 15,2009	56.985	-119.678	Quad-pol
15	ALPSRP177261180	23.1	May 23,2009	58.935	-128.052	Quad-pol
16	ALPSRP179151180	23.1	Jun 05,2009	58.935	-112.484	Quad-pol
17	ALPSRP179301140	23.1	Jun 06,2009	56.983	-121.839	Quad-pol
18	ALPSRP179591150	23.1	Jun 08,2009	57.473	-117.746	Quad-pol

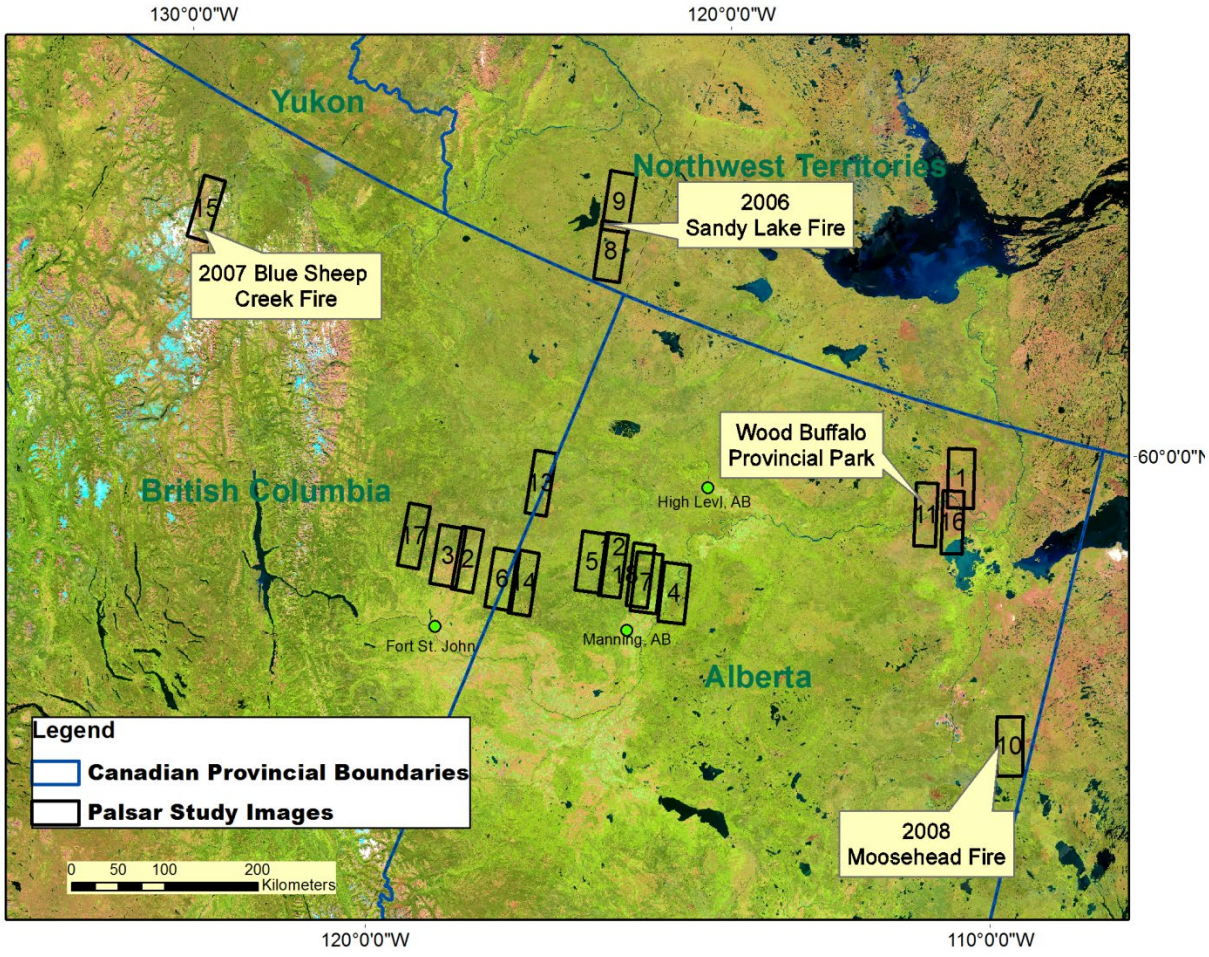

Figure 18 - PALSAR study images – The numbers complement the ID values from Table 7. The closest weather stations to the acquired scenes are also noted in this figure.

5.1.1 Weather conditions for PALSAR Scene Acquisitions

While radar systems can operate in all weather conditions, the radar signal can be significantly affected by rain, snow and soil moisture. Weather data from the closest Environment Canada weather stations was acquired to assist in the selection of the most viable images for further investigation. A complete table of the weather conditions on the date of acquisition for the PALSAR images can be found in Appendix E. To remove any doubt about the existence of snow and high soil moisture (due to melting snow) any scene acquired when the mean temperature that was below five degrees Celsius was removed from consideration. This included all the images

acquired in the months of March, April, and October even though some of the early analysis results indicated strong correlations. The May 7th image was removed from consideration due to rainfall recorded on the day of acquisition. Soil moisture was more difficult to determine due to no direct measurements but it was noted that no significant rainfall was recorded at the nearest weather station on both the day or in the week prior to acquisition for all of the remaining images.

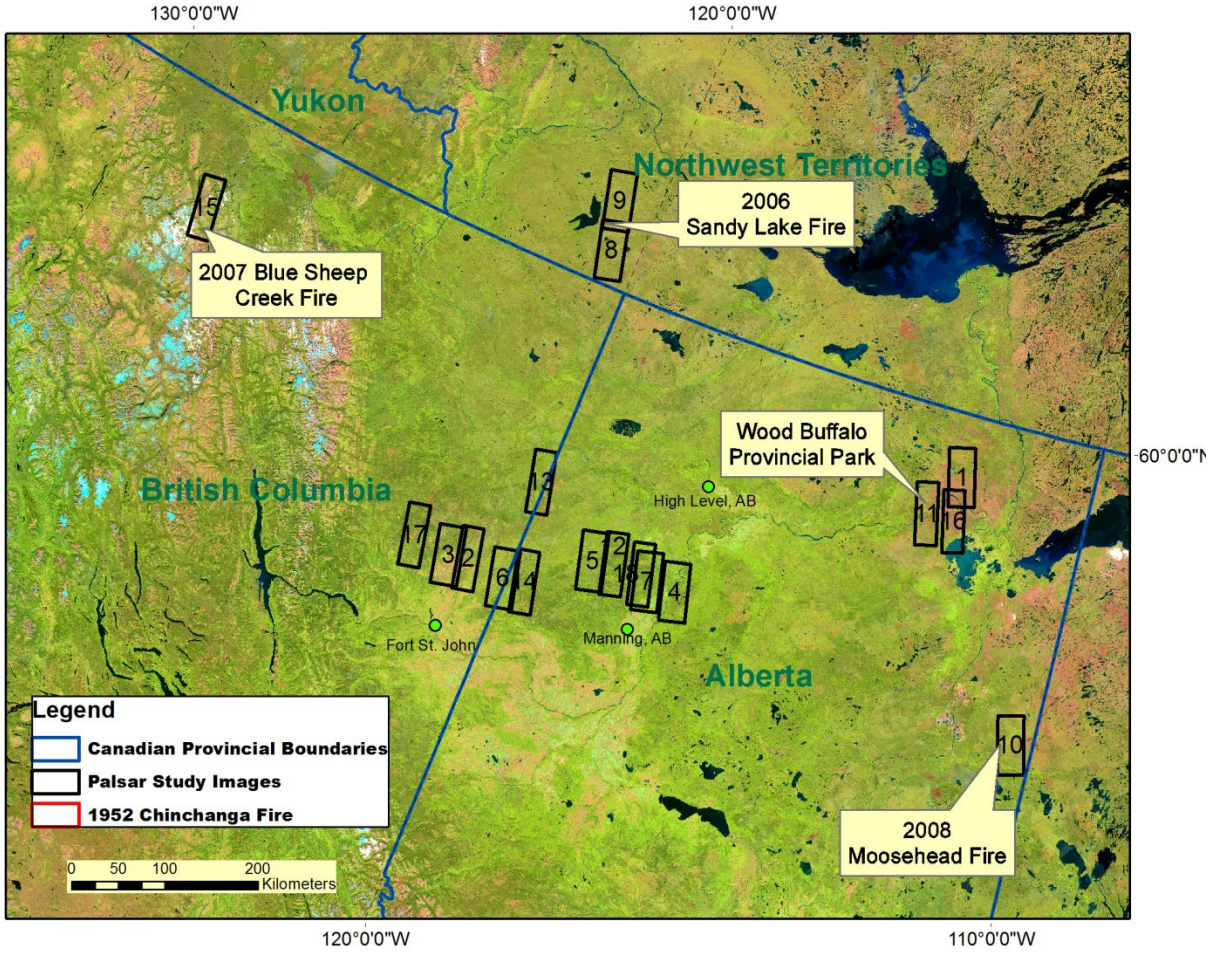

Figure 19 - PALSAR study images – The numbers compliment the ID values from Table 4. The closest weather stations to the acquired scenes are also noted in this figure.

5.1.2 Terrestrial Ecoregions and Ecozones for PALSAR Scene Acquisitions

The PALSAR images all located within the boreal forest in three distinct ecozones that vary in both climate and tree species represented. The vast majority of the PALSAR images are located in the Boreal Planes Ecozone. This ecozone averages 400 mm of precipitation and mean daily July air temperatures of between 12 and 17 degrees Celsius [83]. This region is dominated by the conifer species, white and black spruce, jack pine and tamarack. Broadleaf trees such as white birch, trembling aspen and balsam poplar are also found in this area [83]. The two PALSAR images of

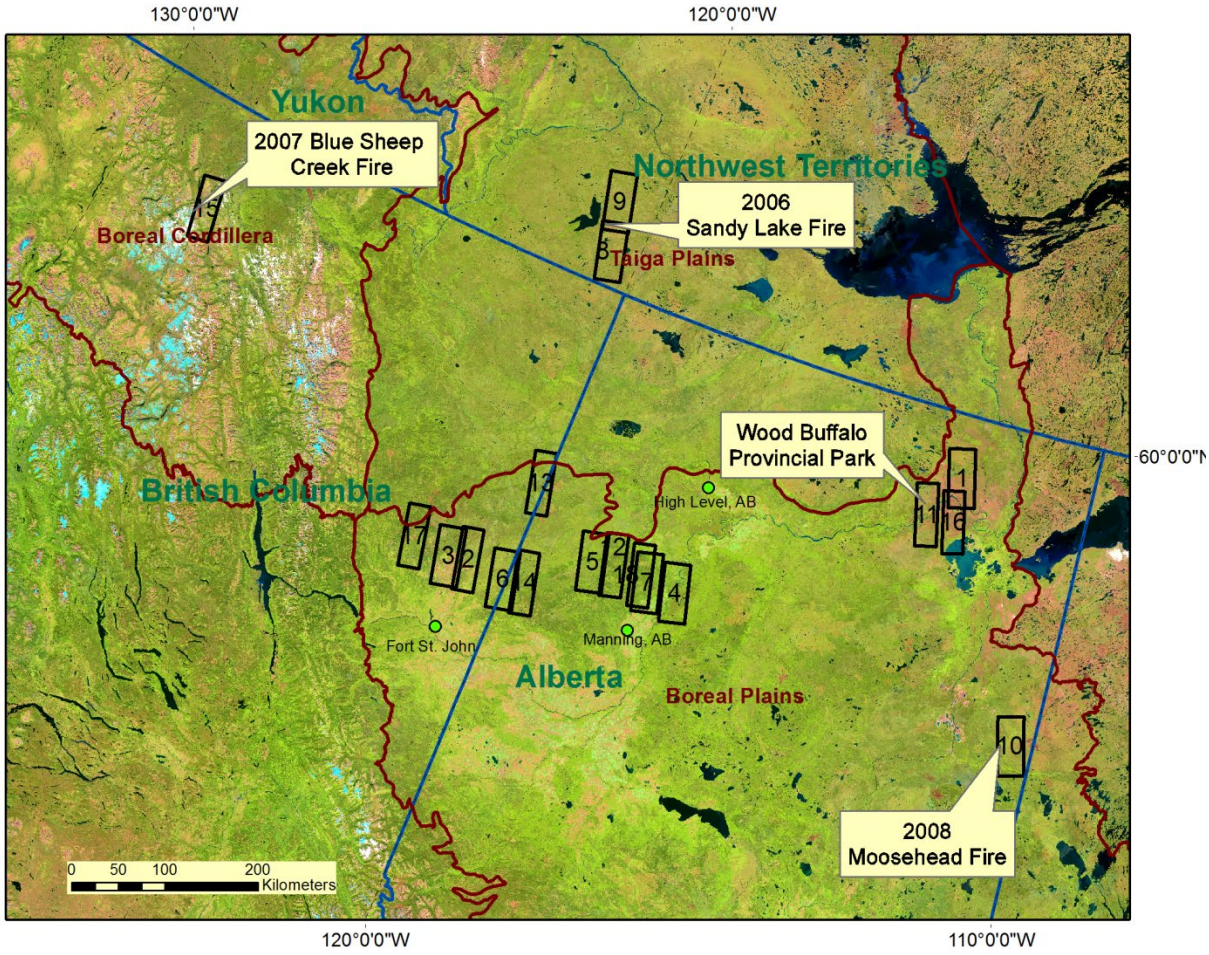

Figure 20 - Three main Ecozones within the study area. The Ecozones are denoted by the red borders.

the Sandy Lake fire in the Yukon Territory are located in the Taiga Plains Ecozone. The climate of this area is semiarid and cold with precipitation ranging from 400 mm in the south to 200 mm in the north and average July air temperature between 10 and 15° C [83]. The mixed wood forest on the southern range of this ecozone includes white and black spruce, tamarack, white birch, trembling aspen, balsam poplar and lodgepole pine. The PALSAR image over the Blue Sheep Creek fire is located in the Boreal Cordillera ecozone. This mountainous region averages 600 mm of precipitation and average July air temperatures between 13 and 18° C. Sub- alpine tree species include lodgepole pine, alpine fir, and Engelmann spruce [83]. Figure 9 presents the study area within the context of the Ecozones represented.

5.2 Analysis

The complete set of PALSAR images was visually compared with the Alberta and NFDB fire history data sets. Four PALSAR images were selected based on the previously discussed weather considerations, their co-location within the same ecozone (the Boreal Plains) to provide the broadest possible age range of wildfire events. These four PALSAR images were acquired on May 15th (2 – North and South), June 6th, and June 8th, and shall henceforth be referred to by their date of acquisition.

5.2.1 Observed Composite Burn Index and PALSAR Decomposition Parameters

One early area of investigation focused on the relationship between the Polarimetric decomposition parameters of a PALSAR scene and the actual ground observations of burn severity that were quantified using the US Forest Services Composite Burn Index or CBI, which estimates the level of burn severity experienced throughout the five levels of strata within the forest. The

author was fortunate to obtain composite burn index field data collected by Parks Canada at the site of the 2005 Peace Point and 2007 Boyer Rapids wildfire events in Wood Buffalo National Park. The CBI data collected was stratified into five distinct categories as previously discussed in Section 2.5. While Wood Buffalo National Park was not within the main Chinchaga study area, it was within the same Ecozone (the Boreal Plains) and equal latitude. The Composite Burn Index varies on a scale from 0 to 3 where a maximum value of 3 indicates highest level of burn severity. Each of these classes was then assigned a CBI value based on the severity of damage to this class. These five values were then used to generate an overall CBI value for each plot. The overall CBI values were averaged equally between the five strata . A second approach, calculated a weighted CBI using the observed proportion that each stratified class contributes to the overall composition of the forest within each plot. Further CBI values were calculated separately for over-story and the under-story.

Thus there were a total of nine distinct CBI values that were available be compared to the radar decomposition parameters. Figure 24 presents an Alpha Entropy Lambda Hue Saturation Value decomposition image of the PALSAR June 5, 2009 acquisition over the Boyer and Peace point wildfires with the field sampling plots where CBI data was available. In total, between the two wildfire events there were 98 viable plots with CBI data available for analysis.

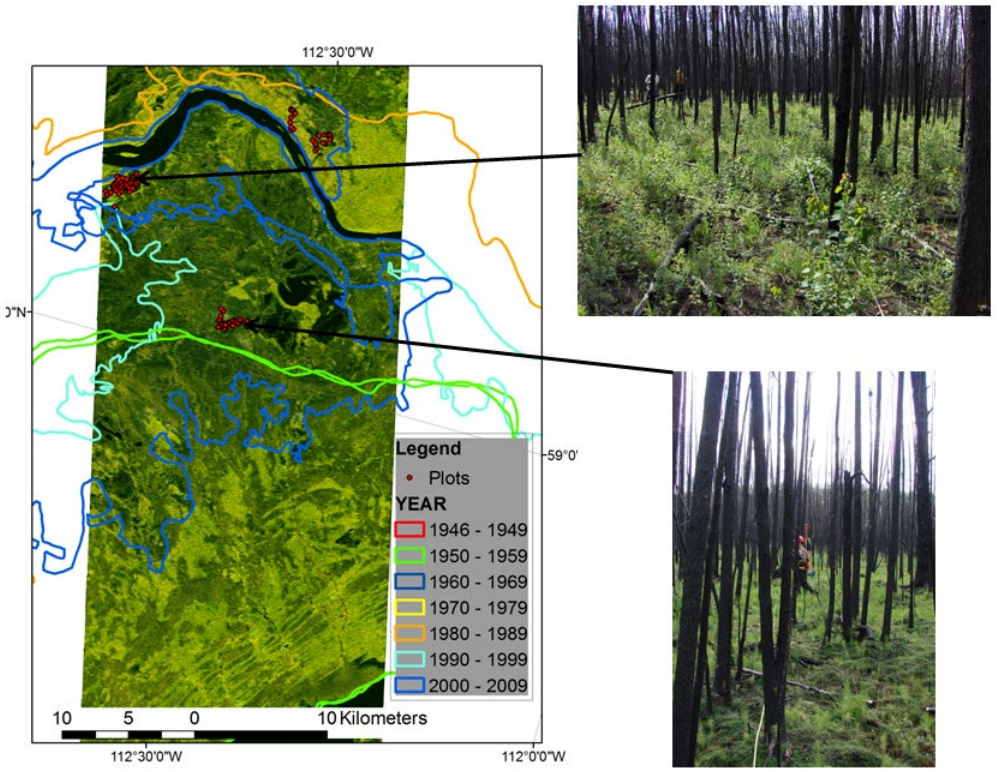

Figure 21 - Hue Saturation Value (HSV) image of Alpha, Entropy, Lambda2&3 (AHL) decomposition image of PALSAR June, 5, 2009 over Wood Buffalo National Park with sample plots from field measurements with accompanying images

The nine CBI values were compared to the decomposition parameters by calculating the Pearson correlation coefficient for all the decomposition parameters and the results are presented in Appendix F. These results suggest that there was a correlation between wild fire effects in the upper strata of the forest (intermediate and large trees) and their related CBI values. This relationship between radar decomposition parameters appears to be consistently strongest with the dominant trees at the forest stand level. Relationships between the CBI values and radar decomposition parameters such as the second and third eigenvalues, probabilities and their subsequent derived values such as RVI, SERD, Pedestal, and polarization fraction all exhibit high R^2

values. Similarly the various Entropy values, Alpha and Anisotropy also appear to be relatively sensitive to the severity of a given wild fire event.

It should be noted that CBI is a human interpreted value based on observation and is therefore subject to variances based on individual biases. Thus CBI values may not be as stable between sites, especially if different survey teams recorded the measurements, but the results from this analysis were encouraging.

Overall, this area of analysis demonstrated that radar decomposition parameters appeared to be moderately sensitive to burn severity within single fire events which suggests that some consideration should be made for this fact during both the classification and modelling phases of this work. Further since it has been demonstrated that CBI and dNBR have a strong correlation [84], it follows that dNBR data calculated from Landsat data could be used to identify areas of high burn severity for sample points to be used for the Polarimetric decomposition analyses.

5.2.2 Temporal Stability between Acquisition Dates

Another early question to be addressed the stability of the decomposition parameters with respect to the seasonality of an image's acquisition. This information could indicate the parameters that are the most temporally stable for dating historic wildfire events. The PALSAR images acquired on April 6, 2009 and June 8, 2009 overlapped and provided an opportunity to investigate this question of temporal stability between early and late spring images. While the look angle was different by 1.6 degrees between the two images, it was not considered significant enough to invalidate this analysis. Three different land cover types (2002 fire scar, forest, and clearcut) were equally sampled and statistics and histograms for Alpha, Entropy, RVI and Luneburg Anisotropy were generated. The results of this analysis can be found in Appendix G.

Entropy, RVI and Luneburg Anisotropy all increased in the June image by approximately 10% as did the standard deviation of these parameters. Alpha also increased slightly by 3% in the later June image. This suggests that seasonality of an image can affect the signal response of a Polarimetric radar acquisition, it is not known if the stability of calibration within the instrument between the two dates might be responsible for some of the observed differences. One final note was that the overall histograms of the overlapping area of the April image displayed a bimodal distribution whereas the June image did not. While not conclusive this bimodal distribution could be due to snow accumulations present within the image.

5.2.3 Entropy/Alpha and Entropy/Anisotropy graphs of selected Forest types in PALSAR Quad-pol Image June 6, 2009

Two of the more useful tools for visualizing polarimetric data are the entropy/alpha and entropy/anisotropy diagrams. These diagrams can provide insight into the separability of classes with various classification techniques. The PALSAR image on June 6, 2009 on the western end of the Chinchaga wildfire event in northeastern BC yielded an unexpected result with a previously unknown fire event in British Columbia. A very large wildfire event G80381 occurred 3 years earlier and was easily distinguished by its radar signature and the subsequent decompositions. This image provided distinct sample areas that represented four distinct boreal forest successional stages. They were

1) Mature forest – not known to have burned since at least 1940,
2) Intermediate forest burned in Chinchaga fire in 1952,
3) Immature forest harvested in 1991 (observed from Landsat BAP images), and
4) Recent fire scar from 2006 event.

Figure 16 displays a 2007 Landsat BAP image on the left with an Entropy Alpha Lambda decomposition on the right. In the same figure, the bottom panels present both Entropy-

Anisotropy and Entropy-Alpha graphs of the four selected areas of interest. The four sample regions are all clearly distinguishable within these graphing planes. Both Entropy and the Alpha values steadily increase with the age of the forest due to an increase in volume scattering, although this is less discernable between the two older classes of forest. The Anisotropy was observed to be changing slightly across all four samples with the values being inversely proportional to the age of the forest. These diagrams suggest that it may be possible to separate these four successional stages using various classification techniques.

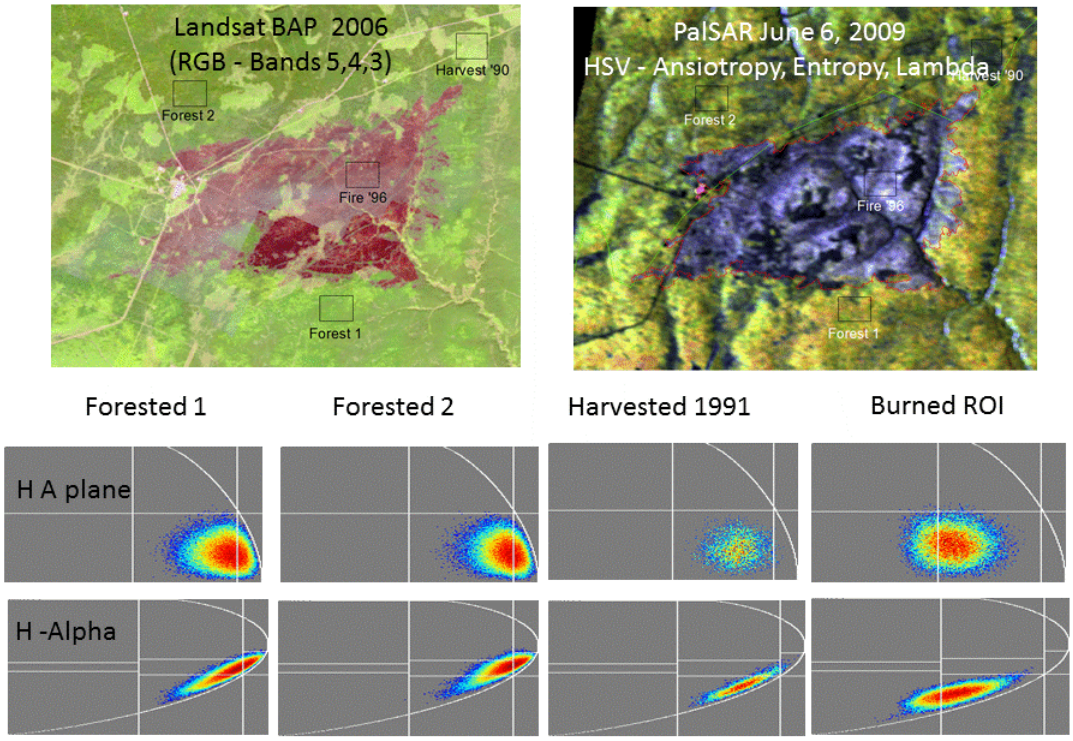

Figure 22 - Landsat optical image immediately after 2006 BC Wildfire G80381. Entropy-Anisotropy, and Entropy-Alpha diagrams of 2006 BC Wildfire G80381 and surrounding forested and harvested areas. The scale for H and A is zero to one and zero to ninety degrees for alpha.

5.2.2 PALSAR Quad-pol Image March 25, 2009

While not included in the final overall analysis due to weather considerations as noted previously, the results from the analysis for the March 25 image are included here to demonstrate the issues with the ability of polarimetric radar to accurately detect fire scars in early season. The full polarimetric PALSAR image acquired on March 25, 2009 provided a wide array of boreal wildfire events to sample. There were wildfire events from 1952, 1969, 1980, 1994, and 1995. A total of fifty sample areas within these fire events were randomly selected across the image and values were then extracted for all 60 different radar decomposition parameters. These parameters were analyzed using linear regression to identify the most sensitive with respect to the age of the wildfire events.

Table 8 - Results of Linear Analysis of decomposition Parameters for March 25, 2009 PALSAR quad-pol image

Parameter	R^2
P_2	0.47
Alpha	0.48
Anisotropy12	0.46
(1- H) (1-A)	0.45
Luneburg Anisotropy	0.44
Alpha1	0.50
P_1	0.42
Asymmetry	0.47
Alpha2	0.48
Entropy	0.39
Pedestal	0.38
SERD	0.37
P_3	0.35
RVI	0.35
Polarisation Fraction	0.34

The Table 8 presents the results of this regression analysis for all the parameters with a R^2 value greater than 0.3. The results of the linear regression indicate that there is a weak

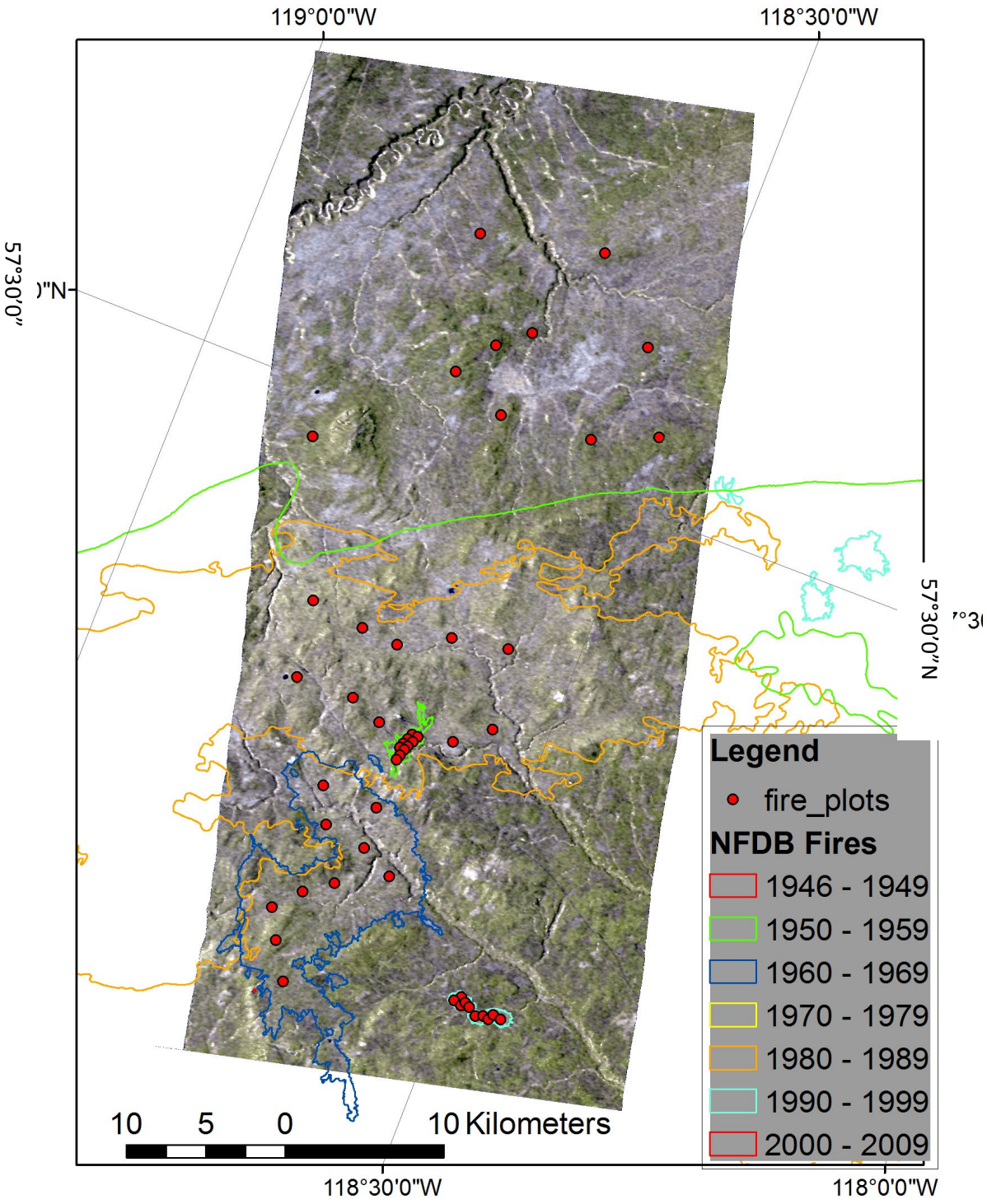

Figure 23 - HSV of Alpha, Entropy and Lambda of PALSAR image for March 25, 2009

relationship between some of the decomposition parameters and number of years since a wildfire event, even for a radar image acquired in the early spring. It will be shown in subsequent analysis of the late spring PALSAR images demonstrated much higher correlations than this early season image.

5.2.3 PALSAR Quad-pol Image May 15, 2009 – South

The quad-pol PALSAR image acquired on May 15 on the southern border of the Chinchaga wildfire event was another target rich image with fire events in the years 1950, 1958, 1982, 1987, and 1993. Fifty random sample plots were selected (10 for each event) and statistics were extracted with a 10 by 10 pixels window over each sample. A linear regression was performed on these samples with 60 decomposition parameters and the best results are presented in Table 6.

Table 9 - Linear regression results for May 15, 2009 PALSAR image

Parameter	R^2
Pedestal	0.95
Luneburg Anisotropy	0.94
SERD	0.94
Anisotropy12	0.93
RVI	0.92
P_3	0.92
Polarisation Fraction	0.92
P_1	0.92
Alpha	0.90
P_3	0.90
Alpha1	0.89
Alpha2	0.86
H(1-A)	0.85
Entropy	0.82
Asymmetry	0.78
L_1	0.78
(1-H)(1-A)	0.77
(1-H)A	0.76
L_3	0.75

The R^2 results were very encouraging with 19 parameters scoring 0.75 or better. Entropy and Alpha R^2 were 0.82 and 0.90 respectively. Once again, the eigenvalues, their probabilities and

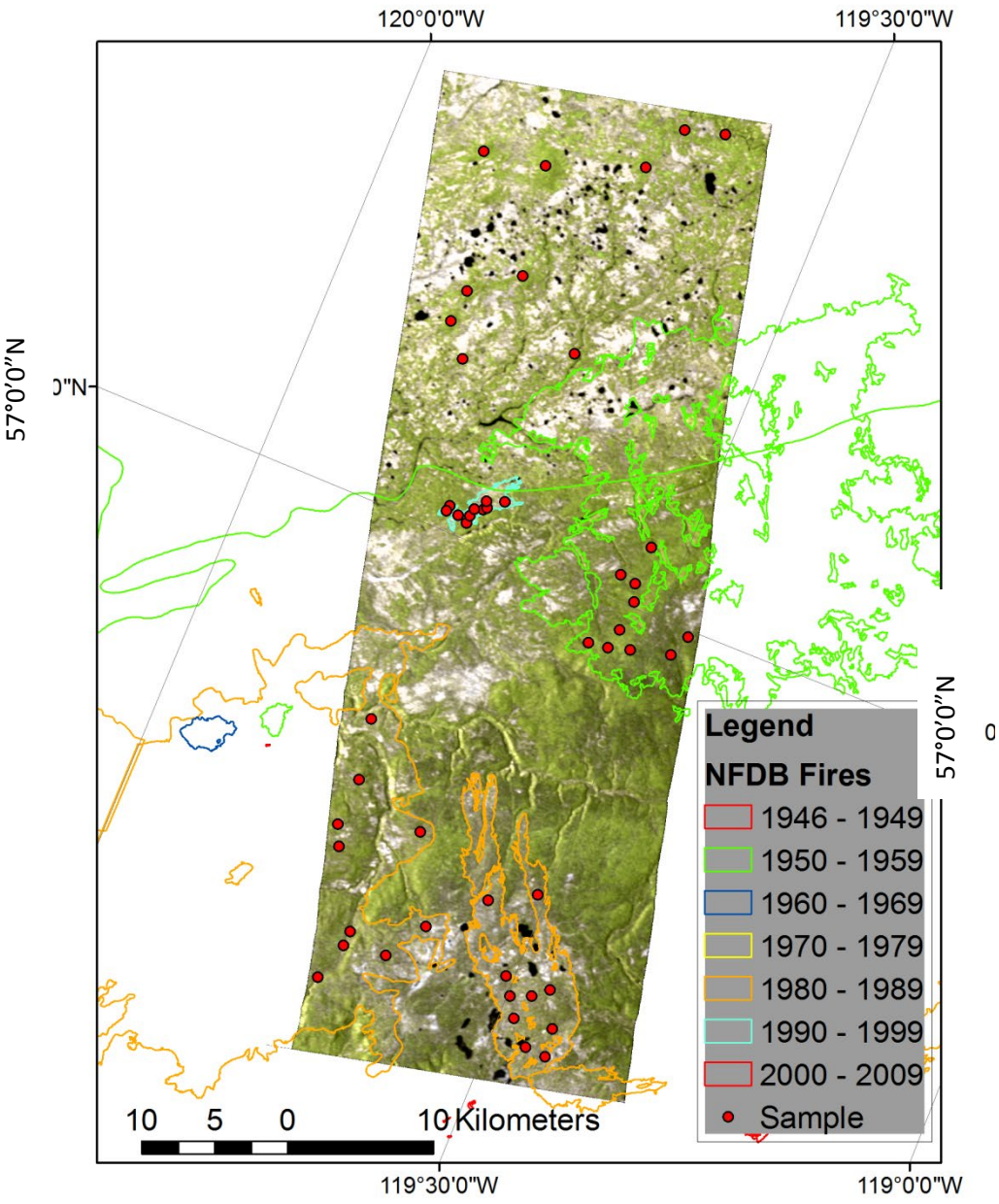

Figure 24 - HSV- Alpha, Entropy, Lambda PALSAR decomposition image acquired May 15, 2009 with Sample plots

their derived parameters all show a strong linear relationship to the date of wild fire events and the subsequent regeneration.

5.2.4 PALSAR Quad-pol Image May 15, 2009 – North

A second PALSAR quad-pol image was acquired on the 15th of May intersecting the northern boundary of the Chinchaga fie event. The scene also offered a rich target environment with fire events occurring in 1950, 1982, 1993, and 2002. Once again, a random set of 10 sample plots was created for each event including 20 plots in what was considered unburned for at least 100 years. A 10 by 10 window was used to extract mean values of all the 60 decomposition parameters that were generated by POLSARPRO and a linear regression analysis was performed. The high scoring Radar Cross Section RCS parameter is a measure of the signal intensity and is highly sensitive to topographic variation and hence could only be used in images acquired over relatively flat areas. It should be noted that this northern image appears to cover an area with less dense vegetation than the previously discussed images. This observation could explain the high correlation of the

Table 10 - R^2 results of linear regression analysis over the Northern May 15, 2009 PALSAR image

Parameters	R^2
Max Radar Cross Section	0.99
Pedestal height	0.99
P_3	0.98
Max Radar Cross Section (Phi)	0.97
Alpha	0.82
Alpha 3	0.80
H(1-A)	0.74
Anisotropy 34	0.63
Luneburg Anisotropy	0.60
Beta1	0.59
RVI	0.54
Entropy	0.42
Alpha 1	0.41

RCS; if the low density forest allowed surface scattering to be the dominant scattering mechanism in this image.

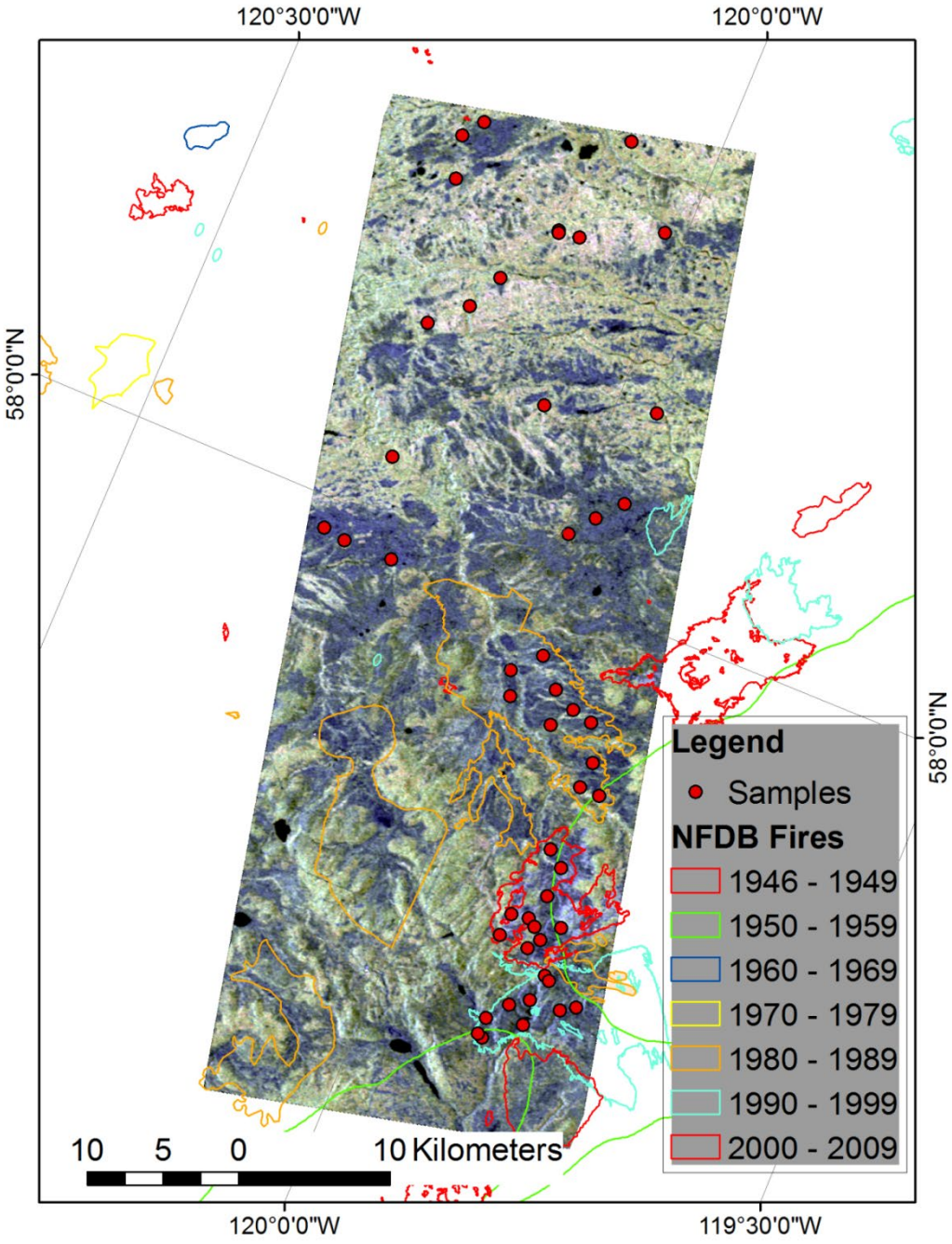

Figure 25 - HSV- Alpha, Entropy, Lambda PALSAR decomposition image acquired May 15, 2009 with Sample plots

5.2.5 PALSAR Quad-pol Image June 8, 2009

The June 8, 2009 PALSAR image was located directly over the 2002 Keg River Fire and some smaller historic wildfire events in 1952, 1990, 1961, 1985, 1998.

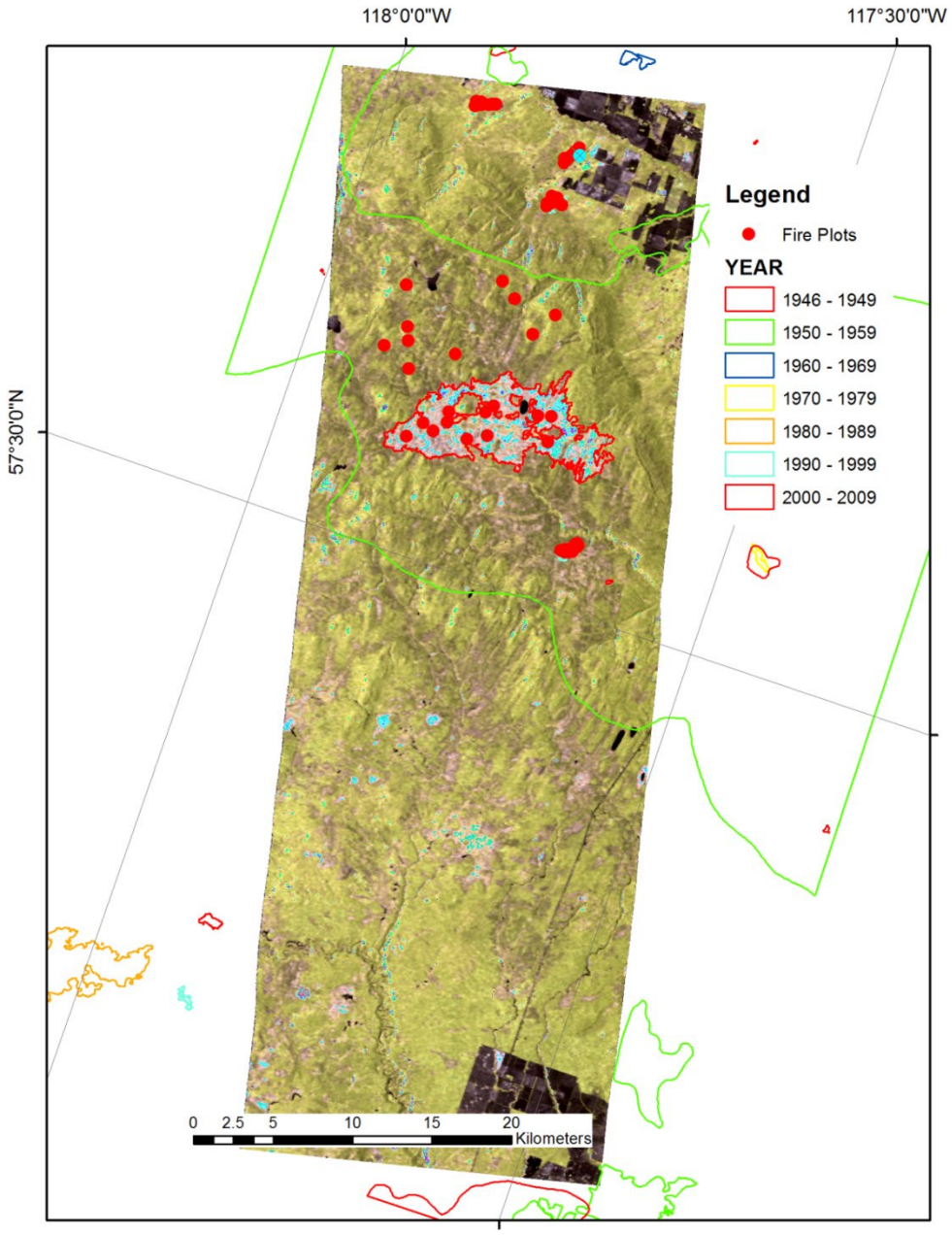

Figure 26 - HSV Alpha, Entropy Lambda Image of PALSAR June 8th, 2009 acquistion

A series of sample points from all of the various fires were selected based on the previously presented methodology. A linear regression was then performed with respect to the various decomposition parameters and the date of the wildfire events. The results of this analysis are presented in Table 11.

Table 11 - R^2 results from linear regression of Decomposition parameters of PALSAR June 8th image.

Parameter	R^2
SERD	0.942
Pedestal Height	0.936
Radar Vegetation Index	0.928
Polarisation Fraction	0.923
Luneburg Anisotropy	0.921
Alpha	0.895
Anisotropy12	0.890
Entropy	0.839

5.2.6 Summary analysis of the Selected PALSAR images

The next phase of analysis was to combine all the extracted decomposition parameters from four PALSAR images (May 15th north and south, and June 6th and 8th) which combined to sample 13 different wildfire events over a span of 70 years.

A linear regression analysis was performed on these combined data. The results of this analysis are displayed in Table 12. The combined analysis for the four images yielded lower results than what was observed within the individual images, with the highest R^2 values not exceeding 0.35. This was likely due to many factors all of which have been previously noted. Radar signals are highly attenuated by water, thus differences in soils moisture could play a role in the increased variability between scenes. As well differences in calibration of the radar instrument between scenes could also be a factor in the lower correlations observed. The variability, the severity of

wildfire event, and its effect on the subsequent regeneration could also play a role in this process. Regeneration can be highly variable as it is sensitive to a host of environmental factors such as topography, wind, moisture availability, and forest age. Some of these factors can vary within a few hundred meters thus making decomposition signature extension for classification from one image to another more challenging. Based on these observations it was decided to focus solely on the classification of individual images which will be presented in the following sections.

Table 12 - Linear Regression R^2 results of combined analysis of four PALSAR images examining 13 different wildfire events over 70 years.

Parameter	R^2
Alpha3	0.34
Alpha	0.32
Alpha1	0.32
SERD	0.32
Pedestal Height	0.31
Polarisation Fraction	0.31
RVI	0.30
P3	0.30
Delta2	0.30
Luneburg Anisotropy	0.30
P1	0.29
Alpha2	0.29
Anisotropy12	0.28
Entropy	0.27
Combination_H1mA	0.27
P2	0.26

5.3 Parametric and Non-parametric Classifications

The linear regression results presented previously were used to select the most descriptive parameters to be used in various classification approaches. The main challenge was the high correlation between these parameters as displayed.

These high correlations in Table 12 were not unexpected since these parameters are all derived from the 3 original complex radar signals (HH, VV, HV) and their subsequent Eigen decompositions. Following the example of Cloude et al. (2007) [50] an entropy, alpha, anisotropy combination of parameters was selected for input into various classification frameworks. It should be noted that Luneburg Anisotropy and RVI were also employed as inputs due to their high correlation with a fire event age.

Table 13 - Correlation between extracted decomposition parameters for 18 fire events over the 70-year span.

	Alpha	Luneburg Anisotropy	Entropy	Pedestal	Polarization	RVI	SERD
Alpha	1.00	0.95	0.94	0.90	-0.91	0.92	-0.93
L. Anisotropy	0.95	1.00	0.96	0.98	-0.97	0.97	-0.93
Entropy	0.94	0.96	1.00	0.93	-0.96	0.97	-0.89
Pedestal	0.90	0.98	0.93	1.00	-0.99	0.99	-0.92
Polarization	-0.91	-0.97	-0.96	-0.99	1.00	-1.00	0.92
RVI	0.92	0.97	0.97	0.99	-1.00	1.00	-0.92
SERD	-0.93	-0.93	-0.89	-0.92	0.92	-0.92	1.00

Two supervised classification techniques were investigated: PCI Geomatica's parametric maximum likelihood and a non-parametric LOGIT classifier. The reason for using two different types of classifiers was to test and compare their performance with these data sets. The four late spring PALSAR images of June 6, 2009, June 8, 2009 and the two May 15th images were selected for classification. This focusing on the late spring images was based on the assumption that the selection of a late spring image would minimize the influence of high soil moisture that possibly could affect the decomposition parameters and the subsequent classification of the earlier spring

images. Four classes were selected for a MLC process: forest, clear-cut, agricultural, water, and the most recent fire scar depending on the image. It should be noted that all four images did not necessarily contain exemplars of all the training classes. The PCI Geomatica supervised maximum likelihood classification application was used for this process. The results were positive with best overall classification results exceeding 97 % with the MLC classifier.

5.3.1 June 6, 2009 PALSAR Classification Results

The PALSAR image acquired on June 6, 2009 provided four main classes to be tested. First, the 2006 B.C. wildfire G80381 provided an excellent exemplar of a three year old boreal fire scar. Within the scene there was also mature forest, clearcuts, and some agricultural land cover. There

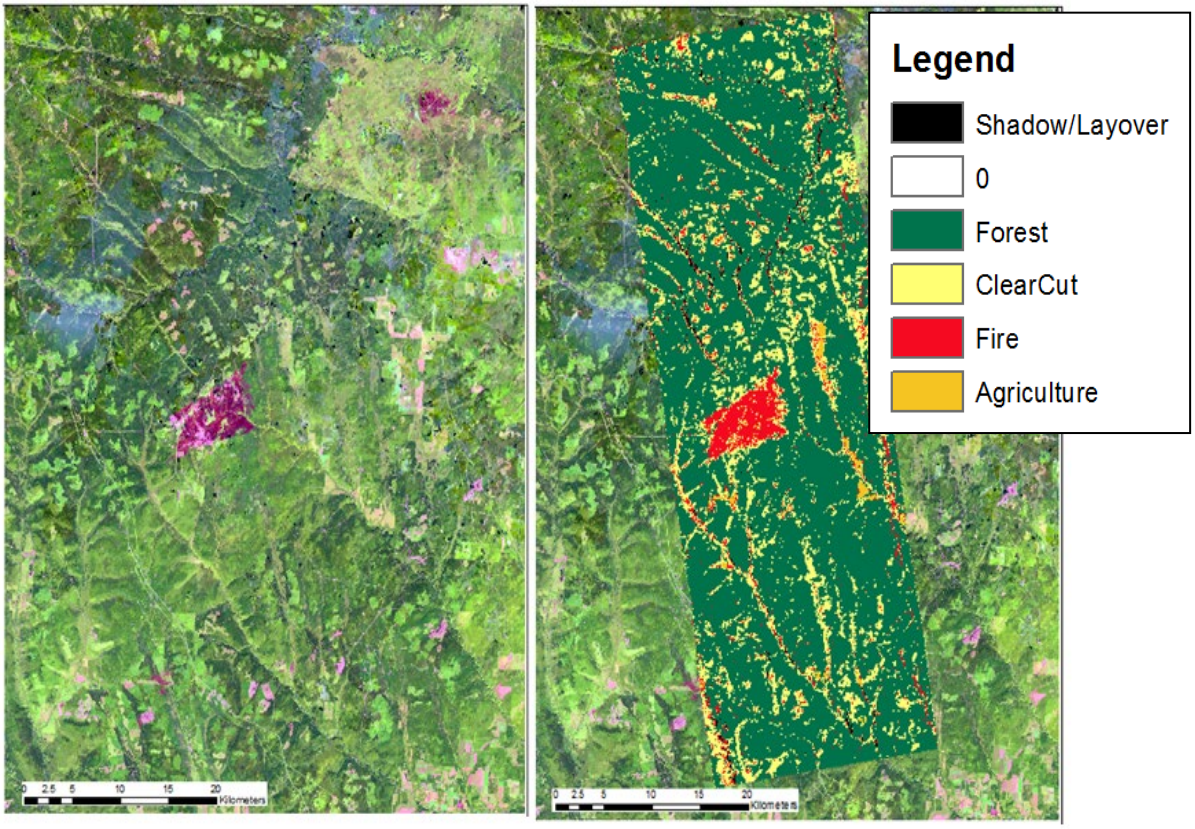

Figure 27 - Maximum Likelihood Classification results of June 6, 2009 PALSAR image. Optical image on the left for reference and the classification image on the right

were what appeared to be some oil and gas anthropogenic structures within the scene, but they were too small to be classified separately, especially when one considered the amount of averaging that was applied to the radar image due to multi-looking and speckle filtering. There was also a small amount of shadow and layover present in the scene. These areas were excluded from the classification process. The best result was achieved using all four input channels (Alpha, Entropy, Radar Vegetation Index and Luneburg Anisotropy) in a Maximum Likelihood Classification framework. Overall accuracy of 97% was achieved for the four classes used in this image. The resultant classification image is displayed in Figure 26.

Visually one can see in the classification image that there was some confusion between fire and some errors of commission for fire in topographically challenging and agricultural areas. The confusion matrix for this classification is presented.

Table 14 - Confusion Matrix Four Maximum Likelihood Classification of June 6 PALSAR image using Alpha, Entropy, Radar Vegetation Index and Luneburg Anisotropy

Code	Pixels	Forest	Clearcut	Fire	Agriculture
Forest	2752	98	2	0	0
Clearcut	1106	0.18	96.84	2.98	0
Fire	1814	0	1.16	98.46	0.39
Agriculture	236	0	1.69	0	98.31
Average	accuracy	=	97.9	%	
Overall	accuracy	=	97.94	%	

The greatest amount of confusion was between agricultural, clearcut and recent fire land cover types. Other Maximum Likelihood Classifications using a subset of the previously mentioned input channels yielded results with an overall accuracy path of between 90 and 95%. Within this

set of classifications, the maximum amount of confusion was primarily between the non-forested classes (fire, clearcut, and agriculture) present in the image. A complete set of all these results can be viewed in Appendix H.

A Non-parametric LOGIT classification was also performed on the same image with the same input channels and the same class exemplars as discussed for the MLC phase. In this series of tests the best classification results with an overall accuracy of 92% was achieved using Alpha, Entropy and Radar Vegetation Index as input channels. The main source of error within this

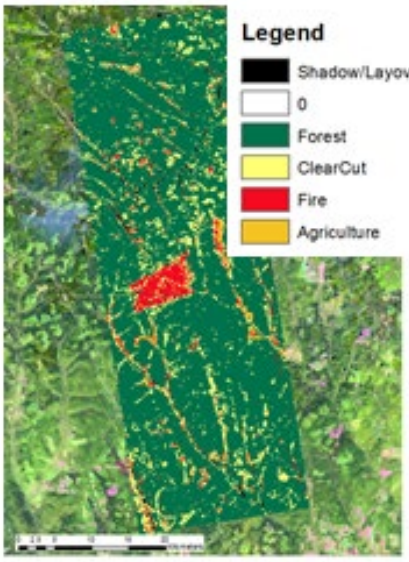

Name	Pixels	Forest	Clearcut	Fire	Agriculture
Forest	2752	99.1	0.9	0	0
Clearcut	1106	33.9	63.1	3	0
Fire	1814	0.2	0.7	99.1	0
Agriculture	236	1.7	0	11.9	86.4
Average accuracy =			86.93%		
Overall accuracy =			91.84%		

Kappa Coefficient =			0.87122	
Standard Deviation =			0.00554	
Confidence Level		99%	0.87122	0.01
		95%	0.87122	0.01
		90%	0.87122	0.01

Figure 28 - LOGIT classification of Alpha entropy and the radar vegetation index for the June 6, 2009 PALSAR image

classification occurred as a result of errors of commission whereby clear-cut pixels were classified as forest. Errors of commission also occurred to a lesser extent where agriculture pixels were classified as fire. When the Luneburg Anisotropy was substituted for radar vegetation index as an input channel overall accuracy dropped to 78%.

In the LOGIT test, errors of commission were forest pixels mistakenly classified as clear-cut, but the converse result which was observed in the MLC tests discussed prevoiously was completely absent. The other main source of confusion occurred between the clear-cut and the fire class. Figure 27 presents the classification image and the associated confusion matrix for the class exemplars. Other LOGIT classifications were performed but the overall accuracies were between 10 and 15% lower than with the Alpha, Entropy and RVI input channels alone. The complete results of these LOGIT classifications can be viewed in Appendix I.

5.3.2 June 8, 2009 PALSAR Classification Results

The June 8 2009 PALSAR image provided five land cover classes for testing. In this image there was a seven year old Keg River fire scar, as well as mature forest, clear cuts, agricultural areas, and water. The same four input channels (Alpha, Entropy, Radar Vegetation Index, and Luneburg Anisotropy) were used together and in subsets for both Maximum Likelihood and LOGIT classification tests. Like the June 6 image, the best results were achieved using a maximum likelihood classifier using all four channels.

The maximum likelihood classification results were between 77 and 70% overall accuracy. The confusion matrix for the best MLC result is presented in Figure 28.The greatest source of confusion in this classification was errors of commission whereby clear-cut was incorrectly assigned to the forest or fire class. There was also moderate confusion between agricultural and

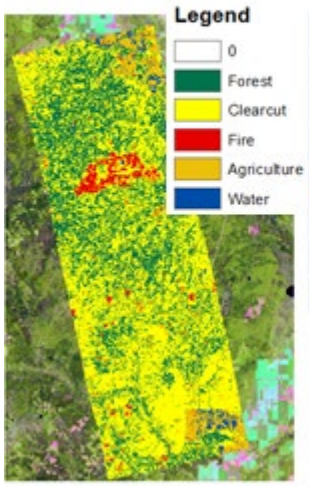

Code	Pixels	Forest	Clearcut	Fire	Agriculture	Water
Forest	760	94.87	5.13	0	0	0
Clearcut	1544	33.23	55.83	10.82	0.13	0
Fire	834	0	0.12	97	2.88	0
Agriculture	9037	0.46	2.52	2.2	77.35	17.46
Water	611	0	0	0	23.24	76.76
Average	accuracy	=	80.36	%		
Overall	accuracy	=	77.05	%		

Kappa	Coefficient	=	0.60014	
Standard	Deviation	=	0.00617	
	Confidence	Level	:	
	99%	0.6	+/-	0.016
	95%	0.6	+/-	0.012
	90%	0.6	+/-	0.01

Figure 29 - MLC result for Alpha, Entropy, RVI, and Luneburg Anisotropy for June 8th PALSAR Image

the water class, probably due to similarities in their surface scattering characteristics and potentially high moisture contents in the agricultural soils. The best LOGIT classification with an overall accuracy of 73% was using the input channels Alpha, Entropy, and Luneburg Anisotropy. Once again the highest source of confusion was with errors of commission within the clear-cut class being assigned to forest and confusion with water pixels being assigned to the agricultural class. The complete results for all of the classification tests of the June 8 image can be found in Appendix J.

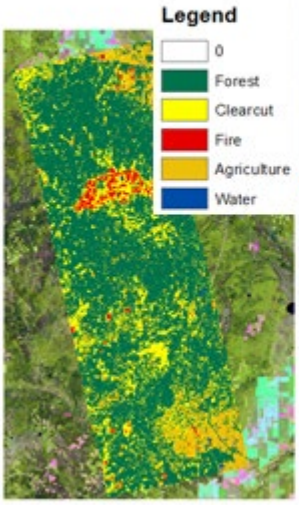

	Pixels	Forest	Clearcut	Fire	Agriculture	Water
Forest	760	98.3	0.1	0	1.6	0
Clearcut	1544	58.4	38.7	2.6	0.4	0
Fire	834	0	4.2	84.3	11.5	0
Agriculture	9037	1.9	11.2	6.9	78.9	1.1
Water	611	0	7.4	0	68.9	23.7
Average	accuracy	=	64.78%			
Overall	accuracy	=	72.94%			

Kappa	Coefficient	=	0.50237
Standard	Deviation	=	0.00656
Confidence	Level	:	
99%	0.50237	+/-	0.01693
95%	0.50237	+/-	0.01286
90%	0.50237	+/-	0.0108

Figure 30 - LOGIT result with Alpha, Entropy, Luneburg Anisotropy for June 8 PALSAR image

5.3.3 May 15, 2009 South PALSAR Classification Results

The May 15 south PALSAR image offered a wide array of fire events occurring in 1952, 1958, 1982, 1987, and 1993. Four land classes were selected for training and classification: fire (1993), mature forest, clearcut, and water. The same four input channels were used in the previous two classification tests described. The best results were achieved with an ML classifier using the input channels Alpha, Entropy, and RVI with an overall classification accuracy of 87%. Figure 30 presents the best classification image achieved for the May 15 south PALSAR image.

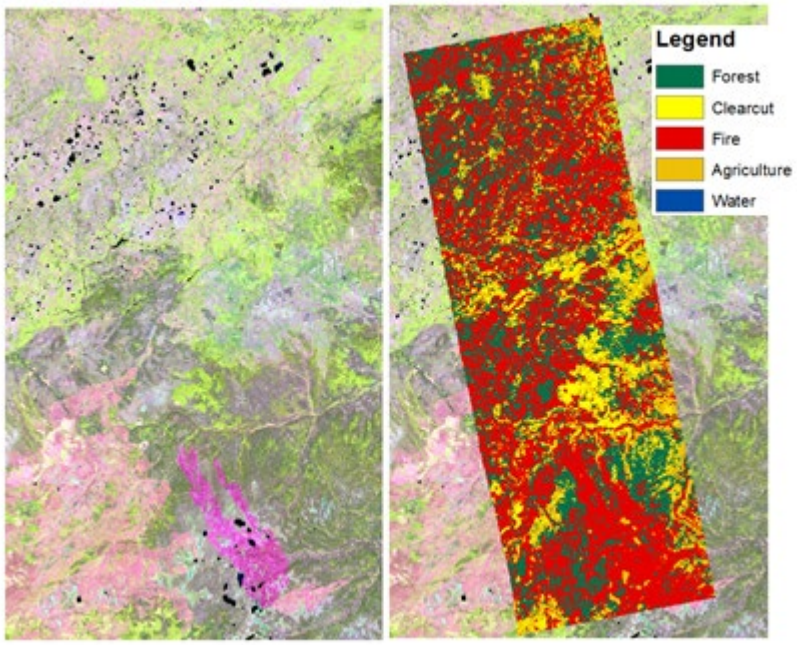

Figure 31 - Landsat BAP and MLC result of PALSAR May 15 south Image using Alpha, Entropy, and RVI

For the best MLC result, the only confusion occurred between the forest and fire classes. This could possibly be due to unburned islands accidentally included in the 1993 fire exemplar, or vigorous regeneration may have occurred. Neither possibility was definitively confirmed in the BAP optical image. This scene demonstrates some of the challenges of detecting and classifying historic wildfire events. The optical image appears to show very little regeneration in any of the fire events including the 70 year old Chinchaga fire. This is probably due to poor site index values (lack of organic matter due to severe ground fires or too much water as evidenced by the high percentage of lakes in the northern half of the image) both of which would hinder regeneration. It appears that all of these historic fires were classified with the more recent fire events. The confusion matrix for the best MLC classification is presented in Table 15.

Table 15 - Confusion Matrix for MLC classification using Alpha, Entropy, and RVI for May 15 set of PALSAR image

Code	Pixels	Forest	Clearcut	Fire	Agriculture	Water
Forest	3875	82.04	0	17.26	0	0.7
Clearcut	1007	0	100	0	0	0
Fire	2179	11.93	0	88.07	0	0
Agriculture	0	0	0	0	0	0
Water	266	0	0	0	0	100
Average	accuracy	=	92.53	%		
Overall	accuracy	=	86.95	%		

The LOGIT classification tests were much lower with overall accuracies averaging approximately 40%. The complete results for all of the classification tests for the May 15th, 2009 PALSAR image can be found in Appendix K.

5.3.4 May 15, 2009 North PALSAR Classification Results

The May 15th, 2009 North PASAR scene also offered a rich target environment with fire events occurring in 1982, 1993, and 2002. The same training classes were used as previously except there were no agricultural or recent clearcut exemplars available for classification and training. The first classification tests class focused on the 2002 wildfire event present in the image. The input channels tested were identical to those used in the previous classifications. The results in this area were lower than in the previous classification tests for the other PALSAR images. The best result was achieved with a ML classifier with Alpha, Entropy, and Luneburg Anisotropy with an overall accuracy of 65%. A MLC test with Alpha, Entropy, and RVI demonstrated an overall

accuracy of 62%. In both these 3 channel classifications the main confusion was between the fire and forest classes. Most interesting was the result for the MLC process when all four input channels were used; the overall accuracy dropped to 42% with majority of the errors being errors of commission with respect to the forest class pixels being misclassified as fire. The LOGIT results ranged from an overall accuracy of 19 to 57 percent. The best LOGIT result – 57% - was with Alpha, Entropy, and Luneburg Anisotropy. Once again the majority of the confusion was between the fire and forest classes. These classification results were viewed with suspicion – due to the lower values than the other images - and hence several sets of different training classes were created and tested but the results remained consistent and stable between classification tests with different training exemplars. The complete results for these tests can be seen in Appendix L. A series of classification tests was also performed using 4 unique fire classes for 1952, 1982, 1993, and 2002 wildfire events.

The MLC classifications for these events displayed overall accuracies in the range of 24-27% and the LOGIT classifier failed to provide any meaningful results. The results for these tests can be found in Appendix M.

5.3.5 May 15, 2009 North PALSAR Classification Results Using An Expanded Set of Input Parameters

Since the classification results for May 15th north image were disappointing, it was decided to explore other parameters with high linear regression R^2 values. Maximum Radar Cross Section and Pedestal Height were selected to be included in this series of classification tests. As previously noted intensity based parameters like RCS are sensitive to topography but this was not an issue in the May 15 north image which had relatively low topographic variation. The training classes were also reviewed and it was discovered using the BAP data set that the clearcuts in the image were

not as recent as first considered. The clearcut class was replaced with an exposed land class with several good exemplars available for training and validating in the northern portion of the image. A water training class was also included although there was a very limited amount of exemplars available. It was also decided to solely test with the MLC classifier since the LOGIT results from the expanded number of classes failed to

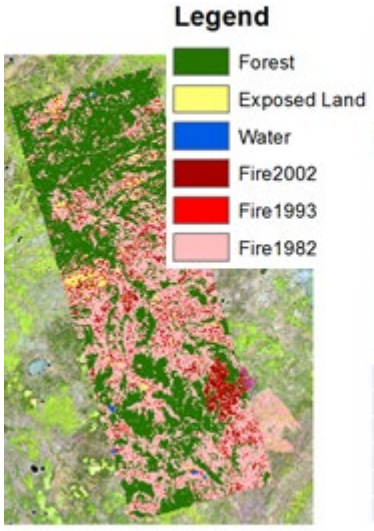

Code	Pixels	Forest	ExposedLand	Water	Fire 2002	Fire 1993	Fire 1982
Forest	1371	99.93	0	0	0	0	0.07
ExposedLand	483	0	93.37	0	4.76	0	1.86
Water	533	0	0	100	0	0	0
Fire2002	1386	0	4.4	0	85.35	0	10.25
Fire1993	784	0.38	0	0	0.26	74.23	25.13
Fire1982	1232	0.08	1.54	0	34.66	0.41	63.31
Average accuracy =			86.03	%			
Overall accuracy =			84.63	%			

Kappa Coefficient =		0.80897		
Standard Deviation =		0.00592		
Confidence Level :				
99%	0.809	+/-	0.015	
95%	0.809	+/-	0.012	
90%	0.809	+/-	0.01	

Figure 32 - MLC results for Alpha, Pedestal Height, Polarization Fraction, and RCS Max for 4 Different Wildfire Events for May 15th North PALSAR image

provide reliable results. The initial MLC results were excellent with overall accuracies with 2 fire classes 2002 and 1993 reaching 97.5% with Alpha, Entropy, RVI, Luneburg Anisotropy, Pedestal Height, and RCS max as input channels. A small amount of confusion (< 5%) was noted between the two fire classes and the exposed land class which was probably due to different regeneration rates caused by variances in site index. These results can be viewed in Appendix N. Next the number of fire classes was expanded to three 1982, 1993, and 2002 using these new parameters.

The results were again very positive with an overall accuracy of 85% using Alpha, Entropy, RVI, Luneburg Anisotropy, Pedestal Height, and RCS. Once again the main source of confusion (10 to 35%) was between the various fire classes and to a lesser extent (5%) between the exposed land class and the most recent 2002 fire, probably for the same reasons noted with respect to regeneration rates. The figure 31 the best classification results as discussed previously for three fire classes. It should be noted that the 1952 wildfire was excluded from testing due to the small area present in the image, and the lack of confidence in the historic fire polygons based on a visual assessment using a 1984 BAP image. The complete results can be viewed in Appendix O.

5.3.6 May 15, 2009 South PALSAR Classification Results Using An Expanded Set of Input Parameters

Following on the positive results of employing an expanded set of input parameter in the May 15th northern image it was decided to revisit the May 15th southern image for classification testing, since it displayed minimal topographic variation and provided a rich set of potential wildfire exemplars of various ages. After reviewing the linear regression results for the image, it was decided to include Polarisation Fraction as well as RCSmax and Pedestal Height along with the initial input channels of Alpha, Entropy, RVI, and Luneburg Anisotropy. Training exemplars included Forest, Water, and four wildfire classes for the years 1993, 1987, 1982, and 1958 were generated for these tests. As with the previous northern image, the clearcut exemplar was removed from the test classes, since they appeared to be older than previously believed upon validation with the BAP data set. The author was not confident in defining any exposed land exemplar pixels to replace the clearcut in this image. The MLC results were consistent for all the combinations of input channels tested, ranging from 72-78% overall accuracy of the four different wildfire events. The best result was achieved using Alpha, Pedestal Height, Polarization Fraction and RCS max. Figure 33 presents the classification image and the resulting confusion matrix.

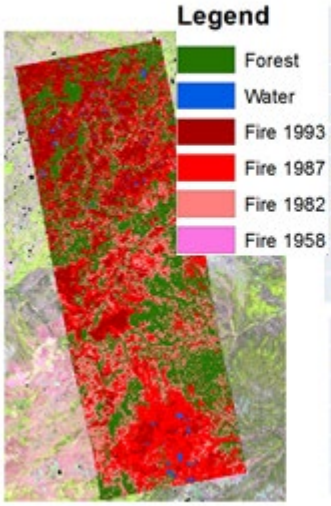

	Pixels	Forest	Water	Fire 1993	Fire 1987	Fire 1982	Fire 1958
Forest	1714	81.97	0	0.82	6.77	10.44	0
Water	557	0	100	0	0	0	0
Fire 1993	248	0	0	95.56	4.44	0	0
Fire 1987	2632	0.11	0	12.16	77.36	10.37	0
Fire 1982	841	11.77	0	0	6.78	81.45	0
Fire 1958	1081	32.56	0	0	0.37	13.14	53.93
Average	accuracy	=	81.71	%			
Overall	accuracy	=	77.8	%			

Kappa	Coefficient	=	0.714	
Standard	Deviation	=	0.006	
	Confidence	Level	:	
	99%	0.714	+/-	0.01622
	95%	0.714	+/-	0.01232
	90%	0.714	+/-	0.01034

Figure 33 - MLC results for Alpha, Pedestal Height, Polarization Fraction, and RCS Max for 4 Different Wildfire Events for May 15th South PALSAR image

Thirty percent of the 1958 wildfire events were classified as forested. The most recent fire, the 26 year old 1993 event, was classified to 95% overall accuracy with the other 5% erroneously committed to the 1987 event that occurred 5 years prior. This was the main challenge to the classifier in this image; three of the four events occurred within a ten year span. This confusion is ultimately tied to the variations in the forest regeneration rates due to site index. This was exacerbated by the low regeneration rates observed in this area as previously discussed in Section 5.3.3. The complete set of results for the May 15th south image, with the expanded set of input channels, can be found in Appendix P.

5.4 Radarsat-2 C-Band For Wildfire Detection

The Canadian Satellite Radarsat-2 was launched in 2007 and carries a C-Band Full Polarimetric radar instrument. While C-Band is not the best wavelength (6cm) to image the forest, protocol dictates that some investigation into the ability to map wildfire scars would be prudent. The author was extremely fortunate to have access to a multi-temporal series of Radarsat-2 Fine Quad-pol images over the 2002 Keg River Fire during the growing season of 2013.

5.4.1 Temporal Analysis over the 2006 Keg River Wildfire

First the seasonal variability of C-Band Radarsat-2 images over the 2002 Keg River Wildfire event is explored. A total of six images were selected and processed according to the previously described processing steps using the Radarsat-Toolbox suite of tools. The figure 34 presents a HSV transformation Alpha, Entropy and Lambda2+Lambda3 decomposition image of the six images for a visual comparison. The colours of these C-Band images are a departure from the previously presented L-Band images due to the different scattering properties of the shorter wavelength C-Band radar signal. Two 100 pixel by 100 pixel sample areas were selected, one within the Keg River fire event of 2006 and an adjacent forest stand burned during 1950 Chinchaga fire event. The values of alpha, anisotropy and entropy were extracted and averaged for each temporal image. The results are presented in the Figure 35. The values of Sigma naught (σ_0), which describes the strength of the return radar signal, were also extracted from all six images and the results are presented in Table 14.

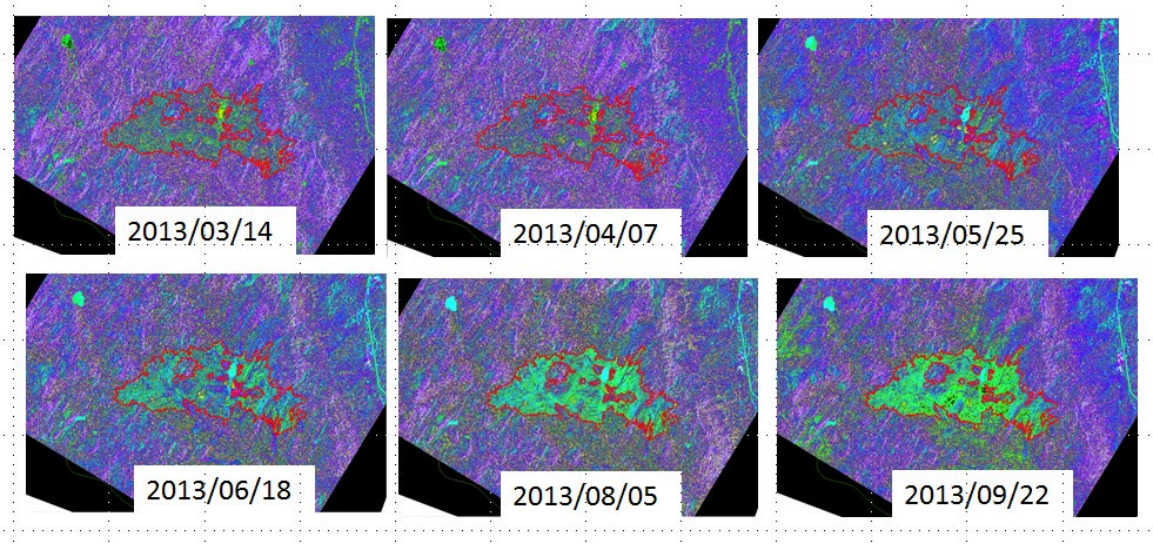

Figure 34 - 2013 Temporal Series of Radarsat-2 images over the 2006 Keg River Fire. All images were created as HSV of Alpha, Entropy, Lambda decompositions.

This temporal series provides an insight into seasonal variability of C-Band radar images in forested environments. Radar signals are highly sensitive to moisture as water is a high attenuating factor. Since σ_0 is reported as decibels (dB), the lower the value the higher the amplitude of the received backscatter radar signal. As such, the maximum value can potentially be used as a proxy for moisture content in the forest environment.

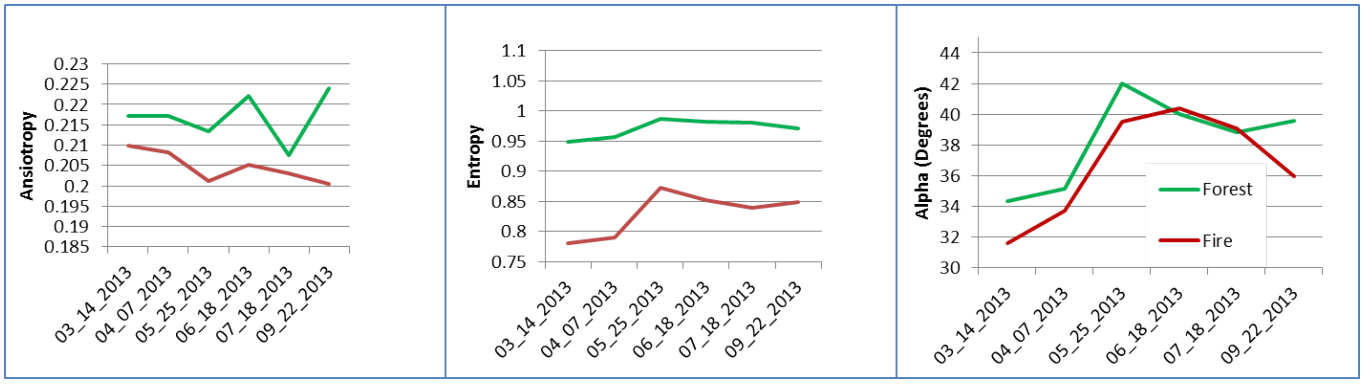

Figure 35 - Graphs of Temporal variation of Radarsat six images for Anisotropy, Entropy, and Alpha for sample area within the Keg River wildfire and nearby Forest

Table 16 - σ_0 statistics for temporal Radarsat-2 images

Date	Max(dB)	Min(dB)	Mean(dB)
March 14, 2013	11.1	93.3	78.1
April 7, 2013	6.0	93.3	77.5
May 25, 2013	10	93.3	77.3
June 18, 2013	11.1	93.3	77.7
August 5, 2013	6.0	93.3	76.6
September 22, 2113	6.0	93.3	76.6

Entropy was relatively stable across the temporal span of the images while both anisotropy and alpha were highly variable but were not correlated with the variation in sigma naught. With both Anisotropy and entropy distinct values were observed between the forest post Chinchaga and the recent Keg River fire event. This is promising, although the variability within the anisotropy could cause confusion within classifiers with C band radar images.

5.4.2 Parametric Classification of Radarsat-2 for 2002 Keg River Wildfire

The analysis presented in the previous section suggests that the late season September 22, 2013 image would provide the maximum separability based on the parameters selected between both the forest and fires classes. Training exemplars for this image were defined as follows: mature forest, water, fire (2002), and agriculture. The input channels selected for the classification tests included Alpha, Entropy, RVI, Luneburg Anisotropy, and Lambda2+3. Based on the previous test results, only MLC tests were performed. The classification accuracies were low for the tests involving combinations of Alpha, Entropy, RVI, and Luneburg Anisotropy attempting to correctly classify the eleven year old fire scar. Interestingly the results improved dramatically when the

Lambda2+3 channel (created for the HSV visualization image) was included in the classification

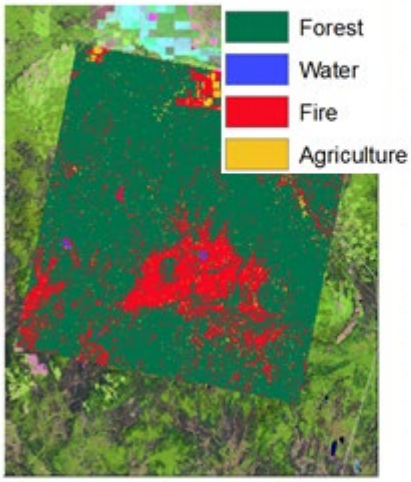

	Pixels	Forest	Water	Fire	Agriculture
Forest	3192	94.89	0	4.42	0.69
Water	2699	0	100	0	0
Fire	13562	8.17	0	87.81	4.02
Agriculture	14448	3.34	0	10.72	85.94
Average	Accuracy	=	92.16	%	
Overall	Accuracy	=	88.65	%	

Kappa	Coefficient	=	0.827	
Standard	Deviation	=	0.003	
	Confidence	Level	:	
	99%	0.827	+/-	0.007
	95%	0.827	+/-	0.005
	90%	0.827	+/-	0.004

rk.

Figure 36 - September 22, 2013 RS2 MLC image and confusion Matrix using Alpha, Entropy, Luneburg Anisotropy, and Lambda2+3 input channels

framework.

Using the input channels of Alpha, Entropy, Luneburg Anisotropy, and Lambda2+3, the overall accuracy reached 89%. The main source of confusion was errors of commission of fire to the forested class and agriculture to the Fire class. Figure 34 displays the best MLC results on the previous page. A complete set of the classification test for this Radarsat-2 image can be found in Appendix Q. For completeness MLC tests were performed on the June 18, 2013 Radarsat-2 image and the overall accuracy results were lower by 3-15% using the same input channels. The results are presented in Table 17. This result demonstrates that Radarsat-2 can be used to detect recent boreal fire scars with a reasonable accuracy depending on the season of acquisition.

Table 17 - Comparison of Classification Results Between September 22 and June 18 2013 Radatsat-2 images

Inputs	September 22, 2013	June 18, 2013
Alpha, Entropy, L. Anisotropy RVI, Lambda2+3	Overall accuracy = 75.27 %	Overall accuracy = 72.01 %
Alpha, Entropy, RVI, Lambda2+3	Overall accuracy = 88.58 %	Overall accuracy = 71.75 %
Alpha, Entropy, Lambda2+3	Overall accuracy = 87.92 %	Overall accuracy = 71.57 %

5 Discussion and Conclusion

The central questions of this thesis are:

5) How can we extract historical fire scar information from polarimetric SAR?
6) Can polarimetric SAR be used to detect and date historical wildfire events in the boreal forest of western North America?
7) Can polarimetric SAR be used to assess the severity of past wildfire events on the boreal landscape with particular attention to the area burned?

Linear regression analysis comparing the Polarimetric decomposition parameters of PALSAR late spring images to the date of historic wildfire events produced R^2 values of up to 0.95 for various parameters. The eigenvalue derived parameters such as Radar Vegetation Index, Polarisation Fraction, Pedestal Height, Single Bounce eigenvalue Relative Difference, Radar Vegetation Index, Entropy, and Luneburg Anisotropy consistently demonstrated the highest R^2 values with respect to the date of a historic wildfire event for all four of the late spring PALSAR images available. The Alpha parameter also performed well with respect to its correlation with the date of historic wildfire events. Several tests were undertaken to classify a combination of decomposition channels of various L-Band PALSAR images using both a Gaussian Maximum Likelihood Classification and non-parametric LOGIT classification algorithms. The Maximum Likelihood Classifier out-performed the non-parametric classifier in all tests. This result suggests that even though the original distribution of these decomposition parameters was Poisson. After multiple averaging windows are applied , the data can be approximated by a Gaussian distribution allowing a parametric classifier to perform well.

A high degree of accuracy (< 90%) was achieved when classifying a single recent fire event with the input channels Alpha, Entropy, RVI, and Luneburg Anisotropy for both the parametric MLC and non- parametric LOGIT classifiers for the four late spring PALSAR images. The MLC classifications were consistently higher than those of the LOGIT classifier.

It was also found that successful classifications of multiple historic fire events from different years within single images were possible. Two PALSAR images acquired on May 15 provided an excellent set of historic fire exemplars that could be used for testing. The northern image contained historic fire events from 7, 16, and 27 years prior to the acquisition date of the PALSAR image. In this image classification, results exceeded 85% accuracy in dating these three events. The southern PALSAR image contained four historic fire events from 51, 27, 22, and 16 years prior to the acquisition date. In this case overall accuracies exceeded 78% with the data using a maximum likelihood classifier. The key to the higher accuracy with the multiple wildfire events was in part due to the addition to the input channels of Pedestal Height, Polarisation Fraction and Radar Cross Section as well as the previously discussed channels of Alpha, Entropy, RVI, and Luneburg Anisotropy.

The final phase of the project investigated the ability of Radarsat-2 C-Band data to detect fire scars. Six Radarsat-2 fine quad-pol images were acquired over the 2002 Keg River fire during the growing season of 2013. Initial analysis suggested that the September 22nd image would provide the highest degree of separability for the classifier. Classification results were extremely positive with overall accuracies exceeding 88% for classifying this single eleven year old historic fire event. In this case the inclusion of a channel that was the sum of the second and third eigenvalues dramatically improved the quality of the result. This is due to the second and third eigenvalues being related to volumetric and anisotropic scattering.

This research provided several valuable insights into the relationship between the radar full polarimetric L band PALSAR and C-band Radarsat-2 decomposition parameters and the effects of fire in the boreal forest. Seasonality plays a crucial role in the ability of full polarimetric radar to detect and classify historic wildfire scars. This was demonstrated by the results of linear regression analysis of various decomposition parameters and the dates of wildfire events on several PALSAR images. The R^2 values (< 0.5) obtained for the early spring March 25, 2009 image were significantly lower when compared to the high R^2 values (> 0.9) of all four of the late spring PALSAR images. The six Radarsat-2 images acquired over the growing season of 2013 supported this observation with the highest degree of separability observed to be with the late fall image.

This work also demonstrated the utility of the Eigen decomposition theory and the various parameters derived from the eigenvalues of this decomposition. All of these parameters demonstrated a high degree of correlation to the age of a historic wildfire event with polarimetric radar image parameters. While these results are encouraging, challenges remain. Radar signals are not temporally invariant. Variations in calibration of the instrument and environmental variations due to moisture levels and seasonal phenological changes can all affect the quality of the radar image and ultimately the decomposition parameters that are generated This temporal instability as was demonstrated in with PALSAR L-Band data in Sections 5.2.2. and with Radarsat-2 C-Band data in Section 5.4.1. This issue makes it difficult to extend the results from one image to another (signature extension).

Within the context of wildfire classifications, the major source of confusion between the different wildfire class exemplars was suspected to be due to differences in the regeneration rates within these wildfire events. The boreal forest is a complex biological system that can be influenced by many factors. Geographic factors such as site index, topography and climate such as moisture

levels and wind can produce wide variations in how wildfires spread across the landscape and the level of burn severity that they inflict on the forest environment. These same factors affect the structural composition of the forest and its ability to regenerate after a wildfire has occurred. The seasonality can also affect both the type and severity of a wildfire event due to phenological and moisture variations. The wildfire history of individual sites also affects wildfire behavior since the age of the stand and the fuel load all are directly dependent on the recent fire history of an area.

The results of this project demonstrated that boreal wildfire scars can be identified and classified to a high level of accuracy within individual scenes. The more complex challenge of modeling forest age across multiple scenes proved more difficult. Many questions remain on how to improve the level of accuracy that can be achieved by mitigating the variations in the radar signatures due to differences in moisture levels, regeneration rates and burn severity. These could be used in conjunction with other remote sensing techniques for fires to improve estimates of burn severity and subsequent regeneration rates, both of which could prove useful to climate and carbon modeling researchers in the future.

7 Future Work

There are several avenues of investigation that could provide insights into the utility of full polarimetric radar remote sensing for historical mapping of boreal wildfires. One area would be to investigate further the effect of moisture levels within the environment and how these affect the returned radar signals. Passive microwave data from sensors such as AVHRR's snow water equivalents (SWE) data or the new SMAP (soil moisture active passive) satellite could provide additional information on soil moisture that could be used to calibrate the radar data and its decomposition parameters. Study areas could also be located closer to existing weather stations that could provide more precise data coincident with acquisition dates and times.

The ongoing Landsat BAP project could also provide a more detailed analysis of the immediate effects of fire on the landscape and a more accurate mapping of burn severity variation within a single fire event using NBR and dNBR indices. This data could be used as an additional source of information for modelling which could potentially improve the results. In addition an investigation of the correlation between the observed CBI values, the optical dNBR indexes and the various radar decomposition parameters could provide insights into fire scar mapping and regeneration rates within the boreal forest.

Compact polarimetry radar which transmits a single circular polarization and receives two linear orthogonal polarizations is a very active area of research [85, 86]. Canada's future Radarsat Constellation Mission (RCM) of three C-Band compact polarimetry satellites to be launched in 2018 will be a new important source of terrestrial radar data for the boreal forest. Recent studies by Chen, Goodenough, and Cloude[85, 86] using simulated compact polarimetry have demonstrated that this type of radar data can be used to map land cover and to detect and map boreal fires scars .

Other valuable areas of investigation include quantifying the variance of radar signals between all of the various boreal ecozones across multiple seasons.

8 References

[1] D. Alcaraz-Segura, E. Chuvieco, H. E. Epstein, E. S. Kasischke, and A. Trishchenko, "Debating the greening vs. browning of the North American boreal forest: differences between satellite datasets," *Global Change Biology,* vol. 16, pp. 760-770, 2010.

[2] L. L. Bourgeau-Chavez, P. A. Harrell, E. S. Kasischke, and N. H. F. French, "The detection and mapping of Alaskan wildfires using a spaceborne imaging radar system," *International Journal of Remote Sensing,* vol. 18, pp. 355-373, 1997.

[3] F. S. Chapin and A. D. McGuire, "Arctic and boreal ecosystems of western North America as components of the climate system," *Global Change Biology,* vol. 6, pp. 211-233, 2002.

[4] E. Chuvieco, P. Englefield, A. P. Trishchenko, and Y. Luo, "Generation of long time series of burn area maps of the boreal forest from NOAA-AVHRR composite data," *Remote Sensing of Environment,* vol. 112, pp. 2381-2396, 2008.

[5] P. S. A. Beck and S. J. Goetz, "Satellite observations of high northern latitude vegetation productivity changes between 1982 and 2008: ecological variability and regional differences," *Environmental Research Letters,* vol. 6, pp. 045501-045501, 2011.

[6] B. D. Amiro and J. M. Chen, "Forest-fire-scar aging using SPOT-VEGETATION for Canadian ecoregions," *Canadian Journal of Forest Research,* vol. 1125, pp. 1116-1125, 2003.

[7] M. S. Balshi, A. D. McGuire, Q. Zhuang, J. Melillo, D. W. Kicklighter, E. Kasischke, C. Wirth, M. Flannigan, J. Harden, J. S. Clein, T. J. Burnside, J. McAllister, W. a. Kurz, M. Apps, and a. Shvidenko, "The role of historical fire disturbance in the carbon dynamics of the pan-boreal region: A process-based analysis," *Journal of Geophysical Research,* vol. 112, pp. 1-18, 2007.

[8] G. B. Bonan and H. H. Shugart, "Environmental factors and ecological processes in boreal forests," *Annual review of ecology and systematics,* vol. 20, pp. 1-28, 1989.

[9] M. E. Alexander, C. N. Stefner, J. A. Mason, B. J. Stocks, and G. R. Hartley, "Characterizing the Jack Pine - Black Spruce Fuel Complex of the International Crown Fire Modelling Experiment (ICFME)," ed: CFS, NRCan, 2004.

[10] L. A. Arroyo, C. Pascual, and J. Manzanera, "Fire models and methods to map fuel types: The role of remote sensing," *Forest Ecology and Management,* vol. 256, pp. 1239-1252, 2008.

[11] L. L. Bourgeau-Chavez, E. S. Kasischke, K. Riordan, S. Brunzell, M. Nolan, E. Hyer, J. Slawski, M. Medvecz, T. Walters, and S. Ames, "Remote monitoring of spatial and temporal surface soil moisture in fire disturbed boreal forest ecosystems with ERS SAR imagery," *International Journal of Remote Sensing,* vol. 28, pp. 2133-2162, 2007.

[12] J. Amthor, J. Chen, J. Clein, and S. Frolking, "Boreal forest CO 2 exchange and evapotranspiration predicted by nine ecosystem process models- Intermodel comparisons and relationships to field measurements," *Journal of Geophysical Research,* vol. 106, pp. 623-648, 2001.

[13] V. K. Arora and G. J. Boer, "Fire as an interactive component of dynamic vegetation models," *Journal of Geophysical Research,* vol. 110, pp. 1-20, 2005.

[14] B. Bond-Lamberty, S. D. Peckham, D. E. Ahl, and S. T. Gower, "Fire as the dominant driver of central Canadian boreal forest carbon balance," *Nature,* vol. 450, pp. 89-92, 2007.

[15] B. D. Amiro, B. J. Stocks, M. E. Alexander, M. D. Flannigan, and B. M. Wotton, "Fire, climate change, carbon and fuel management in the Canadian boreal forest," *International Journal of Wildland Fire,* vol. 10, 2001.

[16] D. G. Goodenough, W. Hong, H. Chen, Y. Li, A. Richardson, F. Cao, E. Chen, P. Wang, and G. W. Hobart, "Mapping Fire Scars From Space Using Radarsat-2 Polarimetric SAR," presented at the ASTRO 2010, Toronto, ON, pp. 1-5, on DVD, 2010.

[17] M. Ohlson, B. Dahlberg, T. Økland, K. J. Brown, and R. Halvorsen, "The charcoal carbon pool in boreal forest soils," *Nature Geoscience,* vol. 2, pp. 692-695, 2009.

[18] T. C. Lemprière, W. A. Kurz, E. H. Hogg, C. Schmoll, G. J. Rampley, D. Yemshanov, D. W. McKenney, R. Gilsenan, A. Beatch, D. Blain, J. S. Bhatti, and E. Krcmar, "Canadian boreal forests and climate change mitigation," *Environmental Reviews,* vol. 21, pp. 293-321, 2013.

[19] B. Hawkes, D. G. Goodenough, B. Lawson, A. Thomson, W. Sahle, O. Niemann, P. Fuglem, J. Beck, B. Bell, and J. Symington "Forest Fire Fuel Type Mapping Using GIS and Remote Sensing in British Columbia," presented at the Proc. GIS, Vamcouver, pp. 647-656, 1995.

[20] C. E. Smyth, G. Stinson, E. Neilson, T. C. Lemprière, M. Hafer, G. J. Rampley, and W. A. Kurz, "Quantifying the biophysical climate change mitigation potential of Canada's forest sector.," *Biogeosciences,* vol. 11, pp. 3515-3529, 2014.

[21] J. Beck, J. Parminter, M. Alexander, E. MacDermid, T. Van Nest, A. Beaver, and S. Grimaldi, Eds., *Fire Ecology and Management,* Forestry Handbook for British Columbia. Vancouver, BC: University of British Columbia, 2005,.

[22] D. T. Price, R. I. Alfaro, K. J. Brown, M. D. Flannigan, R. A. Fleming, E. H. Hogg, M. P. Girardin, T. Lakusta, M. Johnston, D. W. McKenney, J. H. Pedlar, T. Stratton, R. N. Sturrock, I. D. Thompson, J. A. Trofymow, and L. A. Venier, "Anticipating the consequences of climate change for Canada's boreal forest ecosystems.," *Environmental Reviews,* vol. 21, pp. 322-365, 2013.

[23] V. A. Barber, G. P. Juday, and B. P. Finney, "Reduced growth of Alaskan white spruce in the twentieth century from temperature-induced drought stress," *Nature,* vol. 405, pp. 668-73, 2000.

[24] T. A. Black, W. J. Chen, A. G. Barr, M. A. Arian, Z. Chen, Z. Nesic, E. H. Hogg, H. H. Neumann, and P. C. Yang, "Increased carbon sequestration by a boreal deciduous forest in years with a warm spring," *Geophysical Research Letters,* vol. 27, pp. 1271-1274, 2000.

[25] J. L. Allen and B. Sorbel, "Assessing the differenced Normalized Burn Ratio's ability to map burn severity in the boreal forest and tundra ecosystems of Alaska's national parks," *International Journal of Wildland Fire,* vol. 17, pp. 463-463, 2008.

[26] S. H. Boles and D. L. Verbyla, "Comparison of Three AVHRR-Based Fire Detection Algorithms for Interior Alaska," *Remote Sensing of Environment,* vol. 72, pp. 1-16, 2000.

[27] C. H. Key and N. C. Benson, "Landscape Assessment (LA) Sampling and Analysis Methods," USDA Forest Service Gen. Tech. Rep. RMRS-GTR-164-CD, 2006 2006.

[28] D. P. Roy, L. Boschetti, and S. N. Trigg, "Remote Sensing of Fire Severity: Assessing the Performance of the Normalized Burn Ratio," *IEEE Geoscience and Remote Sensing Letters,* vol. 3, pp. 112-116, 2006.

[29] T. Loboda, K. J. O'Neal, and I. Csiszar, "Regionally adaptable dNBR-based algorithm for burned area mapping from MODIS data," *Remote Sensing of Environment,* vol. 109, pp. 429-442, 2007.

[30] J. D. Miller, E. E. Knapp, C. H. Key, C. N. Skinner, C. J. Isbell, R. M. Creasy, and J. W. Sherlock, "Calibration and validation of the relative differenced Normalized Burn Ratio (RdNBR) to three measures of fire severity in the Sierra Nevada and Klamath Mountains, California, USA," *Remote Sensing of Environment,* vol. 113, pp. 645-656, 2009.

[31] J. D. Miller and A. E. Thode, "Quantifying burn severity in a heterogeneous landscape with a relative version of the delta Normalized Burn Ratio (dNBR)," *Remote Sensing of Environment*, vol. 109, pp. 66-80, 2007.

[32] K. A. Murphy, J. H. Reynolds, and J. M. Koltun, "Evaluating the ability of the differenced Normalized Burn Ratio (dNBR) to predict ecologically significant burn severity in Alaskan boreal forests," *International Journal of Wildland Fire*, vol. 17, pp. 490-490, 2008.

[33] L. L. Bourgeau-Chavez, E. S. Kasischke, S. Brunzell, J. P. Mudd, and M. Tukman, "Mapping fire scars in global boreal forests using imaging radar data," *International Journal of Remote Sensing*, vol. 23, pp. 4211-4234, 2002.

[34] D. G. Goodenough, H. Chen, A. Richardson, S. Cloude, W. Hong, and Y. Li, "Mapping fire scars using Radarsat-2 polarimetric SAR data," *Canadian Journal of Remote Sensing*, vol. 37, pp. 500-509, 2011.

[35] D. G. Goodenough and H. Chen, "Evaluation of multi-temporal and multi-polarization ASAR for Boreal forests in Hinton," in *Workshop on the Analysis of Multi-Temporal Remote Sensing Images, 2005 International*, 2005, pp. 1-4.

[36] JAXA. (1997, Nov, 15, 2013). *ALOS Research and Application Project*. Available: http://www.eorc.jaxa.jp/ALOS/en/about/palsar.htm

[37] Canadian Space Agency. (2009, Sept, 11, 2010). *Radarsat2 Satellite Characteristics*. Available: http://www.asc-csa.gc.ca/eng/satellites/radarsat/radarsat-tableau.asp

[38] J.-S. Lee, Pottier, Eric *Polarimetric Radar Imaging: From Basics to Applications*, 1st Edition ed. Boca Raton, Florida: CRC Press, 2009.

[39] D. G. Goodenough, H. Chen, and A. Dyk, "Evaluation of Convair-580 and Simulated Radarsat-2 Polarimetric SAR for Forest Change Detection," Proc. of IGARSS 2006, Denver, Co., pp. 6-9, 2006.

[40] Alberta Environment and Sustainable Resource Development, "Historical Wildfire Database", Calgary, AB: Government of Alberta, 2004

[41] J. C. White, M. A. Wulder, G. W. Hobart, J. E. Luther, T. Hermosilla, P. Griffiths, N. C. Coops, R. J. Hall, P. Hostert, A. Dyk, and G. L., "Pixel-based image compositing for large-area dense time series applications and science," *Canadian Journal of Remote Sensing*, vol. 40, pp. 192-212, 2014.

[42] Center for Topographic Information, Natural Resources. Canada, "Canadian Digital Elevation Data," Natural Reseources Canada, Ottawa, ON: GeoConnections, (2008, August 20, 2009) . Available: ftp://ftp2.cits.rncan.gc.ca/pub/geobase/official/cded/

[43] S. R. Cloude, *Polarisation: Applications in Remote Sensing*, 1st Edition ed. Oxford, England: Oxford University Press, 2009.

[44] C. Wolf. (1996, Sept 20,2014). RadarTutorial. Available: http://www.radartutorial.eu/06.antennas/an14.en.html [45] European Space Agency, "Radar Courses," (2000, Sept. 15, 2014) Available: http://earth.esa.int/applications/data_util/SARDOCS/spaceborne/Radar_Courses

[46] W. M. Boerner, "Basic Concepts in RADAR Polarimetry," (2005. Aug 10, 2014), Available: http://earth.eo.esa.int/polsarpro/Manuals/LN_Basic_Concepts.pdf

[47] A. Freeman and S. S. Saatchi, "On the detection of Faraday rotation in linearly polarized L-band SAR backscatter signatures," *IEEE Transactions on Geoscience and Remote Sensing, ,* vol. 42, pp. 1607-1616, 2004.

[48] S. H. Bickel and R. H. T. Bates, "Effects of magneto-ionic propagation on the polarization scattering matrix," in *Proc. Institute of Radio Engineers*, 1965, pp. 1089–1091.

[49] A. Freeman, "Calibration of Linearly Polarized Polarimetric SAR Data Subject to Faraday Rotation," *IEEE Transactions on Geoscience and Remote Sensing*, vol. 42, August 2004, 2004.

[50] A. Freeman and S. S. Saatchi, "Detection, Estimation and Correction of Faraday Rotation in Linearly Polarized SAR Backscatter Signatures," *Radio*, 1998.

[51] S. R. Cloude, E. Chen, Z. Li, X. Tian, Y. Pang, S. Li, E. Pottier, L. Ferro-Famil, M. Neumann, W. Hong, F. Cao, Y. P. Wang, and K. P. Papathanassiou, "Forest Structure Estimation Using Space Borne Polarimetric Radar: An ALOS-PALSAR Case Study," 2007.

[52] J. S. Lee, D. L. Schuler, and T. L. Ainsworth, " A review of polarization orientation angle estimation from polarimetric SAR data," in *Frontiers of Remote Sensing Infromation Processing*, ed: World Scientific, 2003, pp. 89-104.

[53] J. S. Lee and D. L. Schuler, "Polarization orientation estimation and applications: a review," *IGARSS 2003*, Toulouse, France, pp. 428-430.

[54] J.-S. Lee, D. L. Schuler, and T. L. Ainsworth, "Polarimetric SAR Data Compensation for Terrain Azimuth Slope Variation," *IEEE Transactions on GeoScience and Remote Sensing,* vol. 38, Sept. 2000 2000.

[55] J.-S. Lee, D. L. Schuler, T. L. Ainsworth, E. A. K. E. Krogager, D. A. K. D. Kasilingam, and W. M. A. B. W. M. Boerner, "On the estimation of radar polarization orientation shifts induced by terrain slopes," *IEEE Transactions on Geoscience and Remote Sensing,* vol. 40, pp. 30-41, 2002.

[56] S. R. Cloude and E. Pottier, "A review of target decomposition theorems in radar polarimetry," *IEEE Transactions on Geoscience and Remote Sensing,* vol. 34, pp. 498-518, 1996.

[57] T. L. Ainsworth, S. R. Cloude, and J. S. Lee, "Eigenvector Analysis of Polarimetric SAR Data," *IGARSS 2002 , .,* 2002, pp. 626 - 628.

[58] C. Fang, H. Wen, and W. Yirong, "An Improved Cloude-Pottier Decomposition Using H/ α/SPAN and Complex Wishart Classifier for Polarimetric SAR Classification," in *International Conference on Radar CIE '06,* 2006, pp. 1 - 4

[59] J. S. Lee, M. R. Grunes, and T. L. Ainsworth, "Unsupervised classification using polarimetric decomposition and the complex Wishart classifier," *Transactions on Geoscience and Remote Sensing,* vol. 37, pp. 2249-2258, 1999.

[60] R. Touzi, "Target Scattering Decomposition in Terms of Roll-Invariant Target Parameters," *IEEE Transactions on GeoScience and Remote Sensing,* vol. 45, pp. 73-84, 2007.

[61] S. Chandrasekhar, *Radiative Transfer*. New York: Dover, 1960.

[62] J. R. Huynen, "Phenomenological theory of radar targets," Ph. D., Technical University, Delft, The Netherlands, 1970.

[63] A. Freeman and S. L. Durden, "A Three-Component Scattering Model for Polarimetric SAR Data," *IEEE Transactions on Geoscience and Remote Sensing,* vol. 36, May 1998 pp. 963 - 973, 1998.

[64] S. R. Cloude, I. Hajnsek, and K. P. Papathanassiou, "An Eigenvector Method for the Extraction of Surface Parameters in Polarmetric SAR," in *CEOS SAR workshop,* Toulouse, France, 1999, pp. 693-698.

[65] S. R. Cloude and E. Pottier, "An Entropy Based Classification Scheme for Land Applications of Polarimetric SAR," *IEEE Transactions on GeoScience and Remote Sensing*, vol. 35, pp.68-781997.

[66] P. Réfrégier and J. Morio, "Shannon entropy of partially polarized and partially coherent light with Gaussian fluctuations," *JOSA A*, vol. 23, pp. 3036-3044, 2006.

[67] E. S. Agency. (2006, June 15, 2012). *Do It Yourself 4 - Polarimetric decompositions*. Available: http://earth.eo.esa.int/polsarpro/Manuals/DIY_4_Polarimetric_decompositions.pdf

[68] G. Singh, Y. Yamaguchi, and S.-E. Park, "Capability Assessment of Fully Polarimetric ALOS–PALSAR data for Discriminating Wet Snow from Other Scattering Types in Mountainous Regions," *IEEE Transactions on Geoscience and Remote Sensing*, vol. 52, p. 23, 2014.

[69] Alaska Satellite Facility and Engineering Group, "ASF MapReady User Manual,"

[70] Alaska Satellite Facility, "MapReady Remote Sensing Software," , 2009.

[71] L. Zhang, J. Zhang, B. Zou, and Y. Zhang, "Comparison of Methods for Target Detection and Applications Using Polarimetric SAR Image," *PIERS*, vol. 4, p. 6, 2008 2008.

[72] X. Zhang and S. Kondragunta, "Temporal and spatial variability in biomass burned areas across the USA derived from the GOES fire product," *Remote Sensing of Environment*, vol. 112, pp. 2886-2897, 2008.

[73] European Space Agency, "Polarimetric SAR Data Processing and Educational Tool (POLSARPRO) 4.2 ", ed: European Space Agency, 2011 [74]Array Systems Computing Inc, "RADARSAT-2 Polarimetric Toolbox," Toronto, ON, CA, 2012.

[75] StatSoft Inc., "STATISTICA, version 8.0," Tulsa, OK, 2008.

[76] ENVI\IDL, "ENVI Reference Guide," Boulder, Colorado: Exelis Visual Information Solutions, 2010.

[77] Environmental Systems Research Institute. ESRI 2011. ArcGIS Desktop: Release 10. Redlands, CA: Environmental Systems Research Institute, 2011.

[78] PCI Geomatics, PCI Geomatics Geo-imaging products and solutions: "PCI Geomatica 2012," Richmond Hill, ON, CA, 2012.

[79] Google, "Google EarthPro (Version 6)," Google, 2009. [80]V. Calcagno, "glmulti: Model selection and multimodel inference made easy. R package version 1.0.7," 2013.

[81] R Core Team, "R: A language and environment for statistical computing.," Vienna, Austria: R Foundation for Statistical Computing, 2014.

[82] MathWorks Inc, "MATLAB and Statistics Toolbox Release 2012b. Natick, Massachusetts, United States, 2012.

[83] Microsoft, "Microsoft Office 2003: Excel," Redmond, WA, US, 2003.

[84] D. Sankoff, G. Plunkett, and H. Chen, "LDIAS Software Description – LOGIT Revised, Software Report,," Pacific Forestry Centre, Canadian Forest Service, Natural Resources Canada Victoria, BC.2004.

[85] D. Sankoff, G. Plunkett, and D. G. Goodenough, "LANDSAT Digital Image Analysis System (LDIAS) LOGIT Report," Canada Centre for Remote Sensing, Department of Energy, Mines and Resources, Government of Canada, , Ottawa, Ontario1986.

[86] Parks Canada, "Terrestrial Ecozones of Canada," 1986.

[87] N. O. Soverel, "Validating burn severity classifications using Landsat imagery across western Canadian national parks," M.Sc. Thesis, Forestry, University of British Columbia, Vancouver, BC, 2010.

[88] H. Chen, D. G. Goodenough, and S. R. Cloude, "Compact Radar Polarimetry For Fire Scar Mapping and Landcover Classification," presented at the IET International Radar Conference Xi'an, Shaanxi, China, pp. 1-4, 2013.

[89] H. Chen, D. G. Goodenough, and S. R. Cloude, "Mapping Forest Fire Scars With Simulated RCM Compact-Pol Data," presented at the IGARSS 2014, Quebec, QC, pp. 1572-1575, 2014.

Appendix A. CBI Fire Survey Worksheet

FIREMON LA Form

BURN SEVERITY -- COMPOSITE BURN INDEX (BI)

PD - Abridged	Examiners:		Fire Name:	
Registration Code		Project Code		Plot Number	
Field Date mmddyyyy	/ /	Fire Date mmyyyy	/		
Plot Aspect		Plot % Slope		UTM Zone	
Plot Diameter Overstory		UTM E plot center		GPS Datum	
Plot Diameter Understory		UTM N plot center		GPS Error (m)	
Number of Plot Photos		Plot Photo IDs			

BI – Long Form	% Burned 100 feet (30 m) diameter from center of plot =							Fuel Photo Series =
STRATA RATING FACTORS	BURN SEVERITY SCALE							FACTOR SCORES
	No Effect	Low		Moderate		High		
	0.0	0.5	1.0	1.5	2.0	2.5	3.0	
A. SUBSTRATES								
% Pre-Fire Cover: Litter =	**Duff =**		**Soil/Rock =**		**Pre-Fire Depth (inches): Litter =**	**Duff =**	**Fuel Bed =**	Σ =
Litter/Light Fuel Consumed	Unchanged	--	50% litter	--	100% litter	>80% light fuel	98% Light Fuel	N =
Duff	Unchanged	--	Light char	--	50% loss deep char	--	Consumed	
Medium Fuel, 3-8 in.	Unchanged	--	20% consumed	--	40% consumed	--	>60% loss, deep ch	
Heavy Fuel, > 8 in.	Unchanged	--	10% loss	--	25% loss, deep char	--	>40% loss, deep ch	$\bar{X}$ =
Soil & Rock Cover/Color	Unchanged	--	10% change	--	40% change	--	>80% change	
B. HERBS, LOW SHRUBS AND TREES LESS THAN 3 FEET (1 METER):								
Pre-Fire Cover =			**% Enhanced Growth =**					Σ =
% Foliage Altered (blk-brn)	Unchanged	--	30%	--	80%	95%	100% + branch loss	N =
Frequency % Living	100%	--	90%	--	50%	< 20%	None	
Colonizers	Unchanged	--	Low	--	Moderate	High-Low	Low to None	$\bar{X}$ =
Spp. Comp. - Rel. Abund.	Unchanged	--	Little change	--	Moderate change	--	High change	
C. TALL SHRUBS AND TREES 3 to 16 FEET (1 TO 5 METERS):								
Pre-Fire Cover =			**% Enhanced Growth =**					Σ =
% Foliage Altered (blk-brn)	0%	--	20%	--	60-90%	> 95%	Signifcnt branch loss	N =
Frequency % Living	100%	--	90%	--	30%	< 15%	< 1%	
% Change in Cover	Unchanged	--	15%	--	70%	90%	100%	$\bar{X}$ =
Spp. Comp. - Rel. Abund.	Unchanged	--	Little change	--	Moderate change	--	High Change	
D. INTERMEDIATE TREES (SUBCANOPY, POLE-SIZED TREES)								
Pre-Fire % Cover =			**Pre-Fire Number Living =**		**Pre-Fire Number Dead =**			Σ =
% Green (Unaltered)	100%	--	80%	--	40%	< 10%	None	N =
% Black (Torch)	None	--	5-20%	--	60%	> 85%	100% + branch loss	
% Brown (Scorch/Girdle)	None	--	5-20%	--	40-80%	< 40 or > 80%	None due to torch	
% Canopy Mortality	None	--	15%	--	60%	80%	%100	$\bar{X}$ =
Char Height	None	--	1.5 m	--	2.8 m	--	> 5 m	
Post Fire: %Girdled =			**%Felled =**		**%Tree Mortality =**			
E. BIG TREES (UPPER CANOPY, DOMINANT, CODOMNANT TREES)								
Pre-Fire % Cover =			**Pre-Fire Number Living =**		**Pre-Fire Number Dead =**			Σ =
% Green (Unaltered)	100%	--	95%	--	50%	< 10%	None	N =
% Black (Torch)	None	--	5-10%	--	50%	> 80%	100% + branch loss	
% Brown (Scorch/Girdle)	None	--	5-10%	--	30-70%	< 30 or > 70%	None due to torch	
% Canopy Mortality	None	--	10%	--	50%	70%	%100	$\bar{X}$ =
Char Height	None	--	1.8 m	--	4 m	--	> 7 m	
Post Fire: %Girdled =			**%Felled =**		**%Tree Mortality =**			

Community Notes/Comments:	CBI = Sum of Scores / N Rated:	Sum of Scores	N Rated	CBI
	Understory (A+B+C)			
	Overstory (D+E)			
	Total Plot (A+B+C+D+E)			

% Estimators: **20 m Plot:** 314 m^2 1% = 1x3 m 5% = 3x5 m 10% = 5x6 m
30 m Plot: 707 m^2 1% = 1x7 m (<2x4 m) 5% = 5x7 m 10% = 7x10 m

After, Key and Benson 1999, USGS NRMSC, Glacier Field Station.
Version 4.0 8 27, 2004

Strata and Factors are defined in FIREMON Landscape Assessment, Chapter2, and on accompanying BI "cheatsheet." www.fire.org/firemon/lc.htm

Appendix B. Radar_correction.m

This Matlab script, provided by Ashlin Richardson, performs 3 phases of the preprocessing for the Radar data.
It calculates and corrects for coherency noise. (Section 3.4.7)
It calculates and corrects for Faraday rotation (Section 3.4.1)
It performs a terrain orientation radiometric correction (Section 3.4.2)
.

```
function generateT3 (input_directory)
output_directory = strcat(char(input_directory), 'Out/');
config_file = [char(input_directory),'config.txt'];
config_file
config = textread(config_file, '%s', 'delimiter', '\n', 'whitespace', ' \b\t');

NRow = str2num(char(config(2)));
NCol = str2num(char(config(5)));
%NRow
%NCol
disp 'Opening C4 files ...'
input_directory=strcat(input_directory,'C4/');

fC11=fopen(strcat(input_directory,'C11.bin'),'rb');

fC12_r=fopen(strcat(input_directory,'C12_real.bin'),'rb');
fC12_i=fopen(strcat(input_directory,'C12_imag.bin'),'rb');

fC13_r=fopen(strcat(input_directory,'C13_real.bin'),'rb');
fC13_i=fopen(strcat(input_directory,'C13_imag.bin'),'rb');

fC14_r=fopen(strcat(input_directory,'C14_real.bin'),'rb');
fC14_i=fopen(strcat(input_directory,'C14_imag.bin'),'rb');

fC22=fopen(strcat(input_directory,'C22.bin'),'rb');

fC23_r=fopen(strcat(input_directory,'C23_real.bin'),'rb');
fC23_i=fopen(strcat(input_directory,'C23_imag.bin'),'rb');

fC24_r=fopen(strcat(input_directory,'C24_real.bin'),'rb');
fC24_i=fopen(strcat(input_directory,'C24_imag.bin'),'rb');

fC33=fopen(strcat(input_directory,'C33.bin'),'rb');

fC34_r=fopen(strcat(input_directory,'C34_real.bin'),'rb');
fC34_i=fopen(strcat(input_directory,'C34_imag.bin'),'rb');

fC44=fopen(strcat(input_directory,'C44.bin'),'rb');
```

```
oT11=fopen(strcat(output_directory,'T11.bin'),'wb');

oT12_r=fopen(strcat(output_directory,'T12_real.bin'),'wb');
oT12_i=fopen(strcat(output_directory,'T12_imag.bin'),'wb');

oT13_r=fopen(strcat(output_directory,'T13_real.bin'),'wb');
oT13_i=fopen(strcat(output_directory,'T13_imag.bin'),'wb');

oT22=fopen(strcat(output_directory,'T22.bin'),'wb');

oT23_r=fopen(strcat(output_directory,'T23_real.bin'),'wb');
oT23_i=fopen(strcat(output_directory,'T23_imag.bin'),'wb');

oT33=fopen(strcat(output_directory,'T33.bin'),'wb');
%output_directory
ogamx = fopen(strcat(output_directory,'gamx.bin'),'wb');

disp 'Reading C4 files ...'
C11=fread(fC11, NRow*NCol, 'single');

C12r=fread(fC12_r, NRow*NCol, 'single');
C12i=fread(fC12_i, NRow*NCol, 'single');
C12 = C12r +i*C12i;

C13r=fread(fC13_r, NRow*NCol, 'single');
C13i=fread(fC13_i, NRow*NCol, 'single');
C13 = C13r + i* C13i;

C14r=fread(fC14_r, NRow*NCol, 'single');
C14i=fread(fC14_i, NRow*NCol, 'single');
C14 = C14r + i*C14i;

C22=fread(fC22, NRow*NCol, 'single');

C23r=fread(fC23_r, NRow*NCol, 'single');
C23i=fread(fC23_i, NRow*NCol, 'single');
C23 = C23r + i*C23i;

C24r=fread(fC24_r, NRow*NCol, 'single');
C24i=fread(fC24_i, NRow*NCol, 'single');
C24 = C24r + i*C24i;

C33=fread(fC33, NRow*NCol, 'single');

C34r=fread(fC34_r, NRow*NCol, 'single');
C34i=fread(fC34_i, NRow*NCol, 'single');
```

```
C34 = C34r + i*C34i;

C44=fread(fC44, NRow*NCol, 'single');

%compute gamx
disp 'Computing the complex coherency and plotting it ...'
gamx = C23./sqrt(C22.*C33);
plot(gamx,'o','MarkerSize',2);
hold on;
t = 0:pi/100:2*pi;
plot(exp(i*t),'r');
axis equal
hold off;
gamx = abs(gamx);
%convert to T4
disp 'Converting C4 to T4 ...'
T = cell(4,4);
T{1,1} = C11 + C14 + conj(C14) + C44;
T{1,2} = C11 - C14 + conj(C14) - C44;
T{1,3} = C12 + C13 + conj(C24) + conj(C34);
T{1,4} = C12 - C13 + conj(C24) - conj(C34);
T{2,2} = C11 - C14 - conj(C14) + C44;
T{2,3} = C12 + C13 - conj(C24) - conj(C34);
T{2,4} = C12 - C13 - conj(C24) + conj(C34);
T{3,3} = C22 + C23 + conj(C23) + C33;
T{3,4} = C22 - C33 + conj(C23) - C33;
T{4,4} = C22 - C33 - conj(C23) + C33;
disp 'Radiometric Correction of T4 ...'
 %radiometric correction of T4
 for k=1:4,
    for j=1:4,
       T {k,j} = 0.5*T{k,j};
    end
 end
 disp 'Estimate Faraday Rotation from T4'
 mask = gamx > 0.5;
 faraday=0.25*angle(T{1,1}-T{4,4}+i*2*T{4,4});
 faraday = faraday.*mask;
 disp '  Mean Faraday Rotation: '
 FR_mean = mean(nonzeros(faraday))
 c = cos(-2*FR_mean);
 s = sin(-2*FR_mean);

 disp 'Correct Faraday rotation in T3'
 t11f = c*c*T{1,1} - s*c*(T{1,4}+conj(T{1,4})) + s*s*T{4,4};
 t12f = c*T{1,2} - s*conj(T{2,4});
 t13f = c*T{1,3} - s*conj(T{1,4});
 t14f = s*c*(T{1,1} - T{4,4}) + c*c*T{1,4} - s*s*conj(T{1,4});
```

```
t44f = s*s*T{1,1} + s*c*(T{1,4}+conj(T{1,4})) + c*c*T{4,4};
T{1,1} = t11f;
T{1,2} = t12f;
T{1,3} = t13f;
T{1,4} = t14f;
T{4,4} = t44f;

disp 'Correct for SNR in T3 HV channels ... '
%correct for SNR in T3
T{3,3} = gamx.*T{3,3};
T{2,3} = sqrt(gamx).*T{2,3};
T{1,3} = sqrt(gamx).*T{1,3};

disp 'Correcting for Azimuth Slope/Oriented Volume ...'

theta = -0.25*atan2(2*real(T{2,3}),T{2,2}-T{3,3}+eps);
c = cos(2*theta);
s=sin(2*theta);
r12 = T{1,2}.*c - T{1,3}.*s;
r13 = T{1,2}.*s + T{1,3}.*c;
r22 = T{2,2}.*c.*c + T{3,3}.*s.*s -2*real(T{2,3}).*s.*c;
r23 = (T{2,2} - T{3,3}).*s.*c + T{2,3}.*c.*c -conj(T{2,3}).*s.*s;
r33 = T{2,2}.*s.*s + T{3,3}.*c.*c + 2*real(T{2,3}).*s.*c;

T{1,2} = r12;
T{1,3} = r13;
T{2,2} = r22;
T{2,3} = r23;
T{3,3} = r33;
disp 'Check - The average of T23 must be zero: '
mean(real(T{2,3}(:)))

disp 'Rotation by 45 degrees if T33 > T22 ...'
mask = T{3,3} > T{2,2};
theta2 = mask*pi/4;
c=cos(2*theta2);
s=sin(2*theta2);
r12 = T{1,2}.*c - T{1,3}.*s;
r13 = T{1,2}.*s + T{1,3}.*c;
r22 = T{2,2}.*c.*c + T{3,3}.*s.*s -2*real(T{2,3}).*s.*c;
r23 = (T{2,2} - T{3,3}).*s.*c + T{2,3}.*c.*c -conj(T{2,3}).*s.*s;
r33 = T{2,2}.*s.*s + T{3,3}.*c.*c + 2*real(T{2,3}).*s.*c;
T{1,2} = r12;
T{1,3} = r13;
T{2,2} = r22;
T{2,3} = r23;
T{3,3} = r33;
```

```
disp 'Writing into files ... '
fwrite(ogamx, real(gamx), 'single');

fwrite(oT11, T{1,1},  'single');
fwrite(oT12_r, real(T{1,2}),  'single');
fwrite(oT12_i, imag(T{1,2}),  'single');
fwrite(oT13_r, real(T{1,3}),  'single');
fwrite(oT13_i, imag(T{1,3}),  'single');


fwrite(oT22, T{2,2},  'single');
fwrite(oT23_r, real(T{2,3}),  'single');
fwrite(oT23_i, imag(T{2,3}),  'single');

fwrite(oT33, T{3,3},  'single');

disp 'Closing files ...'
fclose(fC11);

fclose(fC12_r);
fclose(fC12_i);

fclose(fC13_r);
fclose(fC13_i);

fclose(fC14_r);
fclose(fC14_i);

fclose(fC22);

fclose(fC23_r);
fclose(fC23_i);

fclose(fC24_r);
fclose(fC24_i);

fclose(fC33);

fclose(fC34_r);
fclose(fC34_i);

fclose(fC44);


fclose(oT11);

fclose(oT12_r);
fclose(oT12_i);
```

```
fclose(oT13_r);
fclose(oT13_i);


fclose(oT22);

fclose(oT23_r);
fclose(oT23_i);

fclose(oT33);

fclose(ogamx);
disp ‘Process complete. '
```

Appendix C. do_dnbr_ca.pro

This code takes a stack of 26 (1984 – 2009) years of Landsat BAP composite optical data and generates NBR and dNBR images for 25 years as per Section 2.4

```
pro do_dnbr_ca
    compile_opt idl2
    RT_DIR = 'G:\new_bap\UTM12'
    PROV = 'AB'
    DIR_LIST = list(PROV)

    dirHt = hash()
    BASE_DIR =  FILEPATH('',ROOT_DIR = RT_DIR)
    TARGET_YEARS = indgen(29)+1984
    print, TARGET_YEARS

    cd , BASE_DIR
    srs = file_search('SRef_UTM*CC*.dat', count=count, /test_read)
    proj_file = 'G:\new_bap\UTM12\SRef_UTM12S_1984_CC_w_13_11.dat'
    ENVI_OPEN_FILE,proj_file, r_fid=pr_fid, /NO_REALIZE
    ENVI_FILE_QUERY, pr_fid, ns=prns, nl=prnl, nb=prnb, dims=prdims,  BBL=prbbl

    srHt = hash()
    for i= 0, n_elements(srs)-1 do begin
        indx = strsplit(srs[i],'_')
        strYr = strmid(srs[i],indx[2],4)

        yr = fix(strYr)
        print, yr
        srHt[yr] = srs[i]

    endfor

    past = ''
    current = ''

    plyr = ''
    clyr = ''

    cmg=''
    pmg =''
    pns= ''
    pnl=''

    for i = 0 , n_elements(TARGET_YEARS )-2  do begin
       yr = TARGET_YEARS[i]
       print , yr
```

```
if i EQ 0 then begin
   fin = srHt[yr]
   past = FILEPATH(fin,ROOT_DIR = BASE_DIR)

   ENVI_OPEN_FILE, past, r_fid=p_fid, /NO_REALIZE
   ENVI_FILE_QUERY, p_fid, ns=pns, nl=pnl, nb=pnb, dims=pdims, BBL=pbbl

   pmg  = make_array(prns,prnl,2 , /uint, value = 0 )

   print , 'done  phase 1'
   cmg = make_array(prns,prnl,2 , /uint, value = 0 )
   print , 'done  phase 2'
   rmg = make_array(prns,prnl,2 , /integer, value = 0 )
   print , 'done  phase 3'

   xf1 = [0,pns-1]
   yf1 = [0,pnl-1]

   envi_convert_file_coordinates, p_fid, xf1, yf1, wkg_xmap, wkg_ymap , /to_map
   envi_convert_file_coordinates,pr_fid, wkg_xf1, wkg_yf1, wkg_xmap, wkg_ymap


   pmg[wkg_xf1[0]:wkg_xf1[1],wkg_yf1[0]:wkg_yf1[1],0] = uint(ENVI_GET_DATA( fid=p_fid ,
dims=pdims, pos = 3 ))
   pmg[wkg_xf1[0]:wkg_xf1[1],wkg_yf1[0]:wkg_yf1[1],1] = uint(ENVI_GET_DATA( fid=p_fid ,
dims=pdims, pos = 5 ))


   denom = float(pmg[*,*,0])-float(pmg[*,*,1])
   numer = float(pmg[*,*,0])+float(pmg[*,*,1])

   pnbr = (float(denom)/float(numer))*1000.0
   print , 'done  phase 4'
endif else begin
   past = current
   pmg = cmg
   pnbr = cnbr
endelse

current = FILEPATH(srHt[TARGET_YEARS[i+1]],ROOT_DIR = BASE_DIR)
ENVI_OPEN_FILE, current, r_fid=c_fid, /NO_REALIZE
ENVI_FILE_QUERY, c_fid, ns=cns, nl=cnl, nb=cnb, dims=cdims, BBL=cbbl
xf1 = [0,cns-1]
yf1 = [0,cnl-1]

envi_convert_file_coordinates, c_fid, xf1, yf1, wkg_xmap, wkg_ymap , /to_map
envi_convert_file_coordinates,pr_fid, wkg_xf1, wkg_yf1, wkg_xmap, wkg_ymap
```

```
        cmg[wkg_xf1[0]:wkg_xf1[1],wkg_yf1[0]:wkg_yf1[1],0] = uint(ENVI_GET_DATA( fid=c_fid ,
dims=cdims, pos = 3 ))
        cmg[wkg_xf1[0]:wkg_xf1[1],wkg_yf1[0]:wkg_yf1[1],1] = uint(ENVI_GET_DATA( fid=c_fid ,
dims=cdims, pos = 5 ))

       print, "Past " + past
       print, "Current " + current

        wkg_mask = cmg[*,*,0] NE 0 and cmg[*,*,1]NE 0
        cdenom = float(cmg[*,*,0])*wkg_mask -float(cmg[*,*,1])*wkg_mask
        cnumer = float(cmg[*,*,0])*wkg_mask +float(cmg[*,*,1])*wkg_mask

        print , 'getting nbr'
        cnbr = (float(cdenom)/float(cnumer))*1000.0
        fdnbr = pnbr-cnbr
        dnbr = fix(fdnbr)

        rmg[*,*,0] = fix(cnbr)
        rmg[*,*,1] = dnbr
        print , 'writing '
        ndbr_path  = FILEPATH("dNBR_"+PROV+"_"+strtrim(TARGET_YEARS[i+1],2)+".dat",ROOT_DIR =
'c:\deleteme')
        ENVI_WRITE_ENVI_FILE, rmg, DATA_TYPE= 2 , NB= 2, NL= cnl, NS=cns,  $
            OFFSET=0, INTERLEAVE=0 ,OUT_NAME=ndbr_path,  R_FID=outfid
        ENVI_WRITE_FILE_HEADER, outfid


        res = do_set_inheritance(current, ndbr_path, 2, 2 )
    endfor

    print , 'all done'

 end
```

Appendix D. build_burn_mask.pro

This script takes 25 years dNBR masks and creates a single byte layer where the most significant digit represents the year and the least significant digit represents the level of burn severity observed.

```
pro build_burn_mask

    compile_opt idl2
    ;inpath = 'V:\Landsat\scripts\batch\epoch2_2010.txt'
    RT_DIR = 'f:'
    PROV = 'PAL'
    dirHt = hash()
    BASE_DIR = 'F:\Landsat_BAP'; FILEPATH('',ROOT_DIR = RT_DIR, SUBDIRECTORY= [dir_list.toArray()])
    TARGET_YEARS = indgen(22)+1990
    print, TARGET_YEARS
    debug =1
    SC_DIR = 'F:\PAL\scenes'
    SC_DIR = 'F:\RS2'
    cd , SC_DIR
    srs = file_search('ALPSRP*.dat')
    srs= list('RS2_footprint.dat')
    BR_DIR = 'F:\dNBR'
    cd , BR_DIR
    brs = file_search('dNBR_PAL_*.dat', count=count, /test_read)
    brHt = hash()
    for i= 0, n_elements(brs)-1 do begin
        sc = brs[i]
        print, sc
        indx = strsplit(sc,'_')
        strYr = strmid(sc,indx[2],4)
        yr = fix(strYr)
        print, yr
        brHt[yr] = sc

    endfor



    numyr = n_elements(TARGET_YEARS)

    for i= 0, n_elements(srs)-1 do begin
        tgt =filepath(srs[i],root_dir=sc_dir)
        print, tgt
        envi_open_file, tgt, r_fid=t_fid , /NO_REALIZE
        ENVI_FILE_QUERY, t_fid, ns=tns, nl=tnl, nb=tnb, dims=tdims, BBL=tbbl
        tgt_proj = envi_get_projection(fid=t_fid, pixel_size=tps)
```

```
wkg_xf1 = ''
wkg_yf1 = ''

br_image = make_array( tns,tnl ,1, /byte, value = 0 )
bandNames = list()
for j = 0 , n_elements(TARGET_YEARS)-1  do begin

 yr = TARGET_YEARS[j]
 bandNames.add,strtrim(yr,2)
 print , yr
 cbr = filepath(brHt[yr], ROOT_DIR = BR_DIR)
 flist = list(tgt,cbr)
 tmp_pth = FILEPATH("wkg_"+strtrim(yr,2)+'_'+srs[i] ,ROOT_DIR = SC_DIR )
 ;if file_test(tmp_pth, /read) NE 1 then begin
     build_multi_file_stack_excl,flist , tmp_pth ,tgt
 ;endif

 print ,cbr
 envi_open_file, tmp_pth, r_fid=b_fid , /NO_REALIZE

 wkg_lyr =  ENVI_GET_DATA( fid=b_fid ,  dims = tdims, pos = 2 )

 brn_mask = wkg_lyr GE 100
 update_mask = wkg_lyr GE 100

 wkg_dnbr = fix(wkg_lyr*brn_mask)- 100
 sev_scale = wkg_dnbr/150
 ovr_sev = sev_scale GT 9
 sev_scale = sev_scale*(ovr_sev eq 0)+sev_scale*(ovr_sev)*9


  updt_vals = sev_scale + byte((j+1)*10)*update_mask
  cmplt_image = br_image GT 0

 br_image = br_image*(cmplt_image) + updt_vals*update_mask*(cmplt_image EQ 0)


endfor

print , 'writing '
br_path  = FILEPATH('BAR_fire_map_'+srs[i],ROOT_DIR =
'F:\RS2\RS2_RESULTS\RS2_results\Burn_maps')
;br_path = 'F:\RS2\BAP_KegRiver_year_fire_map.dat'
ENVI_WRITE_ENVI_FILE, br_image, DATA_TYPE= 1 , NB= 1, NL= tnl, NS=tns,  $
   OFFSET=0, INTERLEAVE=0 ,OUT_NAME=br_path,  R_FID=outfid
ENVI_WRITE_FILE_HEADER, outfid
```

```
        res = do_set_inheritance(tgt, br_path, 1, 1 )
    endfor

    print , 'all done'
end
```

Appendix E. Environment Canada Weather Data from Nearby Stations

ID			High Level			Fort St. John				Closest Weather Station		
	Palsar Scene Name	Date	Mean Temp (°C)	Snow (cm)	Percip (mm)	Mean Temp (°C)	Snow (cm)	Percip (mm)	Station	Mean Temp (°C)	Snow (cm)	Percip (mm)
1	ALPSRP062601190	Mar 29,2007	3.1	0	0	3.2	0	0	Mildred Lake	1.7	0	0
2	ALPSRP147501140	Oct 30,2008	-5.3	0	0	0.5	0	0				
3	ALPSRP167631140	Mar 18,2009	-22	0.2	0	-12	0.2	0				
4	ALPSRP167921150	Mar 20,2009	-14.2	0	0	-10.6	8.2	0				
5	ALPSRP168651150	Mar 25,2009	-13.3	5.4	0	-13.4	4.2	0				
6	ALPSRP169381140	Mar 30,2009	-1.7	0	0	1	0	0				
7	ALPSRP170401150	Apr 06,2009	4.8	0	0	5	0	0				
8	ALPSRP171131210	Apr 11,2009	3.4	0	0	5.1	0	0	Trout Lake	-1.3	0	0
9	ALPSRP171131220	Apr 11,2009	3.4	0	0	5.1	0	0	Trout Lake	-1.3	0	0
10	ALPSRP171711140	Apr 15, 2009	3	0	0	5	0	0	Fort McMurray	3.3	0	0
11	ALPSRP174921180	May 07,2009	10.1		0.2	7.8	0	0.4	Mildred Lake	7.1	0	0
12	ALPSRP175361150	May 10,2009	10.2	0	0	10.8	0	0				
13	ALPSRP176091160	May 15,2009	4.4	0	0	7.1	0	0				
14	ALPSRP176091140	May 15,2009	4.4	0	0	7.1	0	0				
15	ALPSRP177261180	May 23,2009	11.4	0	0	12.5	0	0	Watson Lake	12.8	0	1
16	ALPSRP179151180	Jun 05,2009	7.3	0	0	11.4	0	0	Mildred Lake	7	0	0
17	ALPSRP179301140	Jun 06,2009	7.3	0	0	8.8	0	0				

18	ALPSRP179591150	Jun 08,2009	12.2	0	0	11.6	0	0				

Appendix F. Results of linear regression for various Polarimetric SAR parameters versus field measured Composite Burn Index (CBI)

R^2 results of CBI for both 2005 Peace Point Wildfire Event and CBI 2007 Boyer Rapids Wildfire verses the radar decomposition parameters. CBI values range from [0,3] with 3 being the highest level of burn severity.

	S1-CBI	S2-CBI	S3-CBI	S4-CBI	S5-CBI	Weighted CBI	CBI total	CBI overstory	CBI understory	Max Y (CBI) Standard Error
Pedestal	0.07	0.01	0.06	0.38	0.48	0.14	0.23	0.46	0.78	0.77
RVI	0.07	0.02	0.07	0.38	0.47	0.14	0.23	0.45	0.78	0.76
Polarisation Fraction	0.07	0.02	0.07	0.38	0.47	0.14	0.23	0.45	0.77	0.76
p3	0.07	0.02	0.07	0.38	0.47	0.14	0.23	0.45	0.82	0.76
SERD	0.06	0.01	0.04	0.35	0.47	0.14	0.22	0.45	0.78	0.77
p1	0.05	0.00	0.03	0.34	0.45	0.11	0.20	0.44	0.79	0.78
Entropy	0.04	0.01	0.04	0.33	0.44	0.11	0.19	0.43	0.74	0.78
Anisotropy Luneburg	0.05	0.00	0.03	0.33	0.44	0.10	0.19	0.43	0.76	0.78
Entropy Shannon	0.03	0.01	0.05	0.30	0.40	0.10	0.18	0.40	0.76	0.82
Anisotropy 12	0.04	0.00	0.02	0.29	0.40	0.09	0.16	0.39	0.76	0.79
l3	0.20	0.11	0.22	0.43	0.38	0.29	0.35	0.38	0.78	0.74
p2	0.03	0.00	0.01	0.27	0.37	0.08	0.14	0.36	0.79	0.79
Combination H1mA	0.06	0.02	0.08	0.32	0.38	0.13	0.21	0.36	0.77	0.77
l2	0.17	0.07	0.12	0.34	0.32	0.21	0.27	0.32	0.69	0.78
Alpha	0.00	0.02	0.00	0.30	0.33	0.01	0.06	0.31	0.81	0.82
Combination 1mH1mA	0.01	0.00	0.02	0.21	0.30	0.05	0.10	0.29	0.77	0.81
Combination 1mHA	0.07	0.03	0.05	0.32	0.27	0.12	0.17	0.27	0.83	0.81

R^2 results of CBI 2005 Peace Point Wildfire Event verses the radar decomposition parameters. CBI values range from [0,3] with 3 being the highest level of burn severity.

	S1-CBI	S2-CBI	S3-CBI	S4-CBI	S5-CBI	Weighted CBI	CBI total	CBI overstory	CBI understory	Max Y (CBI) Standard Error
p1	0.08	0.35	0.19	0.45	0.48	0.47	0.43	0.48	0.25	0.71
Anisotropy Luneburg	0.09	0.37	0.18	0.45	0.47	0.48	0.43	0.48	0.26	0.72
Pedestal	0.11	0.27	0.20	0.41	0.49	0.45	0.42	0.47	0.25	0.68
Alpha	0.04	0.28	0.23	0.44	0.46	0.43	0.39	0.46	0.21	0.76
Entropy	0.06	0.30	0.19	0.41	0.45	0.43	0.40	0.45	0.23	0.70
Anisotropy 12	0.07	0.36	0.16	0.43	0.44	0.44	0.40	0.45	0.23	0.74
l3	0.19	0.36	0.39	0.42	0.46	0.48	0.47	0.45	0.39	0.74
Polarisation Fraction	0.09	0.22	0.20	0.37	0.46	0.42	0.39	0.43	0.24	0.68
RVI	0.09	0.22	0.20	0.37	0.46	0.42	0.39	0.43	0.24	0.68
p3	0.09	0.22	0.20	0.37	0.46	0.42	0.39	0.43	0.24	0.68
l2	0.17	0.47	0.29	0.43	0.41	0.48	0.45	0.42	0.38	0.80
p2	0.06	0.36	0.15	0.41	0.41	0.42	0.38	0.42	0.22	0.75
SERD	0.07	0.22	0.12	0.37	0.43	0.38	0.34	0.42	0.17	0.64
Entropy Shannon	0.03	0.24	0.17	0.35	0.40	0.37	0.34	0.39	0.19	0.83
Combination 1mH1mA	0.03	0.31	0.15	0.36	0.37	0.37	0.33	0.37	0.18	0.79
Combination H1mA	0.07	0.13	0.17	0.26	0.35	0.30	0.28	0.32	0.17	0.72
Delta1	0.11	0.20	0.14	0.32	0.31	0.31	0.31	0.32	0.21	0.91
Asymmetry	0.03	0.30	0.08	0.29	0.24	0.28	0.25	0.27	0.14	0.85

R square results of CBI 2007 Boyer Rapids Wildfire Event northern sampling area verses the radar decomposition parameters. CBI values range from [0,3] with 3 being the highest level of burn severity.

	S1-CBI	S2-CBI	S3-CBI	S4-CBI	S5-CBI	Weighted CBI	CBI total	CBI understory	CBI overstory	Max Y (CBI) Standard Error
Entropy Shannon	0.22	0.00	0.01	0.46	0.61	0.14	0.30	0.04	0.63	0.86
Entropy	0.22	0.00	0.01	0.43	0.60	0.13	0.29	0.04	0.62	0.77
SERD	0.29	0.01	0.05	0.44	0.60	0.21	0.37	0.10	0.61	0.78
RVI	0.22	0.01	0.06	0.54	0.57	0.16	0.34	0.08	0.59	0.76
Polarisation Fraction	0.22	0.01	0.06	0.54	0.57	0.16	0.34	0.08	0.59	0.76
p3	0.22	0.01	0.06	0.54	0.57	0.16	0.34	0.08	0.59	0.76
Pedestal	0.22	0.00	0.04	0.46	0.56	0.14	0.31	0.07	0.57	0.74
Alpha	0.22	0.00	0.02	0.47	0.55	0.15	0.30	0.05	0.57	0.76
p1	0.22	0.01	0.00	0.35	0.54	0.11	0.26	0.03	0.55	0.75
Anisotropy Luneburg	0.20	0.01	0.00	0.29	0.50	0.09	0.22	0.02	0.50	0.75
Combination H1mA	0.17	0.03	0.10	0.55	0.46	0.16	0.31	0.10	0.48	0.84
Combination 1mH1mA	0.15	0.02	0.00	0.26	0.48	0.08	0.19	0.01	0.48	0.83
l3	0.32	0.01	0.00	0.48	0.45	0.19	0.29	0.09	0.47	0.76
Anisotropy 12	0.18	0.02	0.00	0.22	0.46	0.08	0.19	0.01	0.45	0.78
p2	0.17	0.02	0.00	0.18	0.44	0.07	0.17	0.01	0.43	0.80
Combination 1mHA	0.15	0.02	0.03	0.54	0.28	0.11	0.21	0.07	0.30	0.89

Appendix G. Temporal comparison of Overlapping PALSAR decomposition parameters between June 8 and April 6 images acquired in 2009.

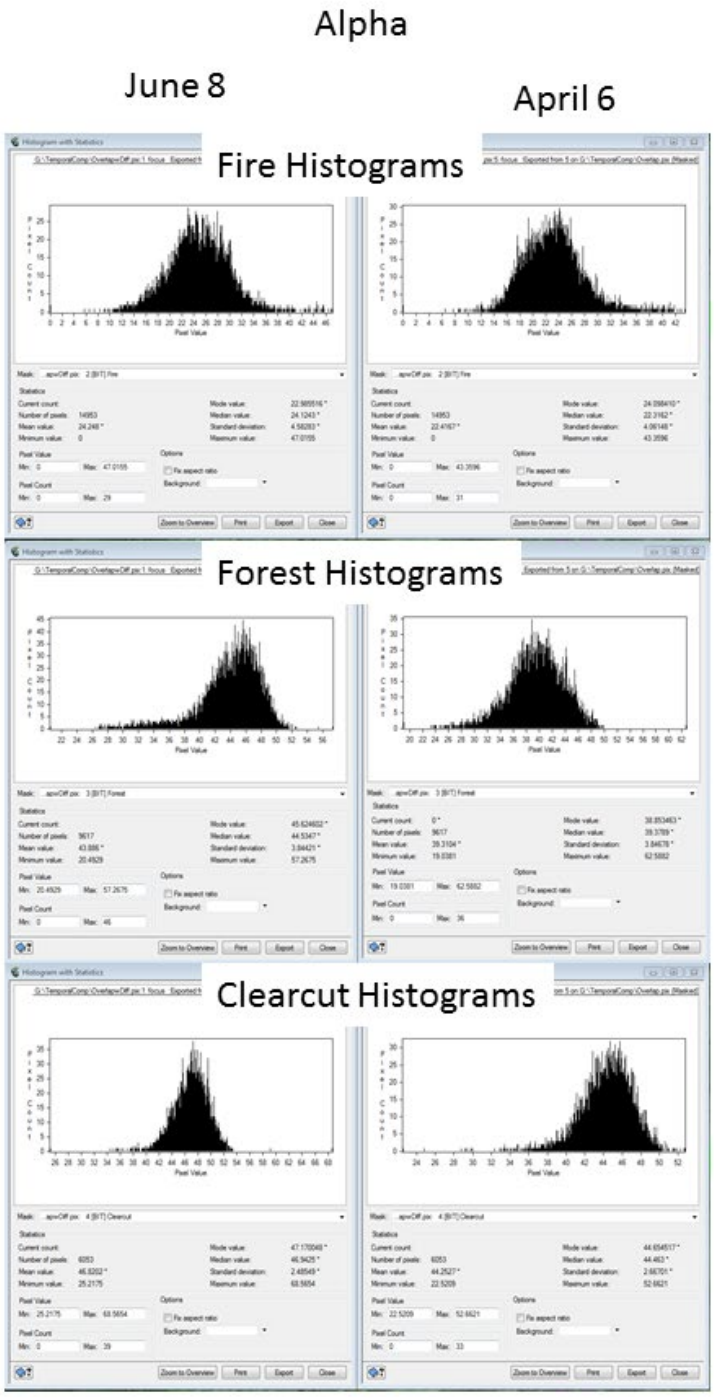

Entropy

June 8 April 6

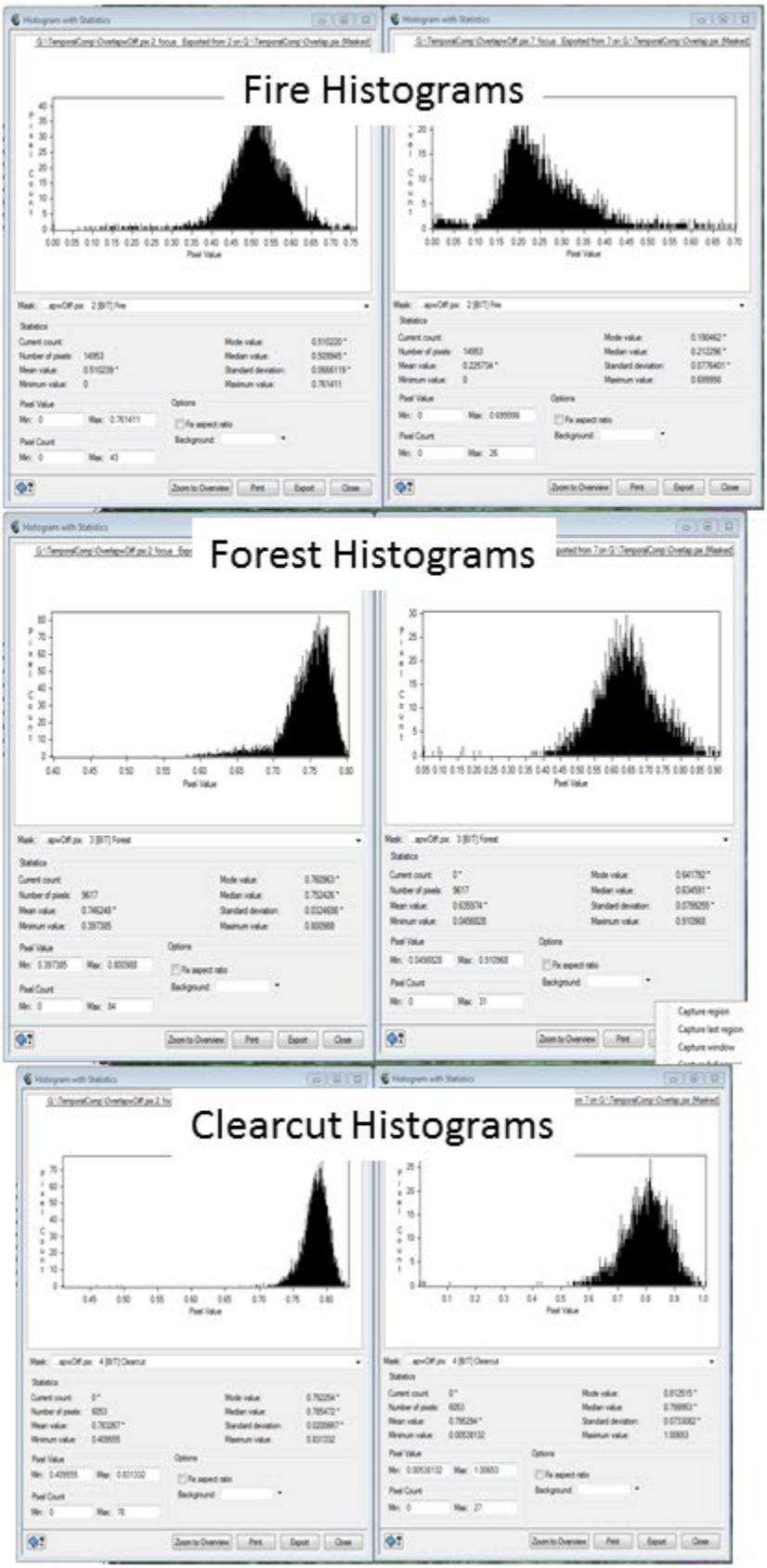

RVI

June 8 April 6

Fire Histograms

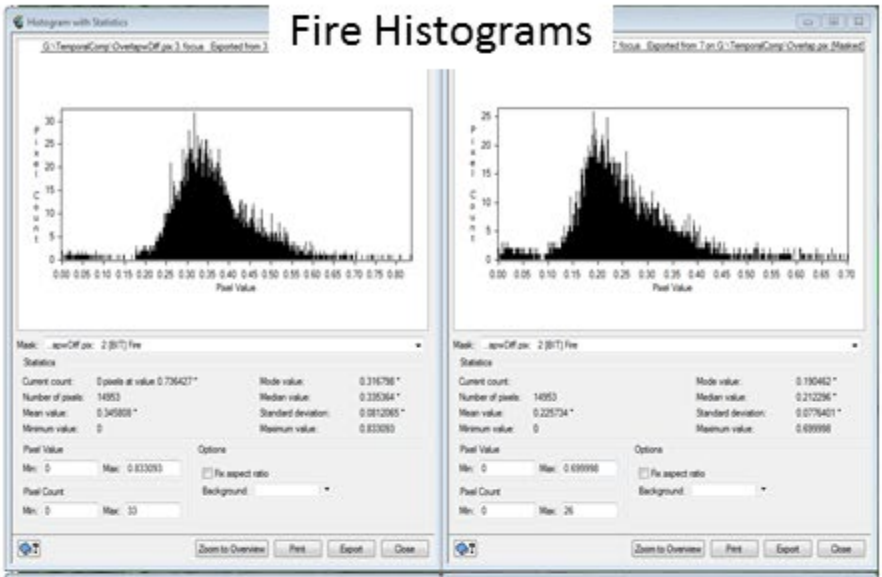

Forest Histograms

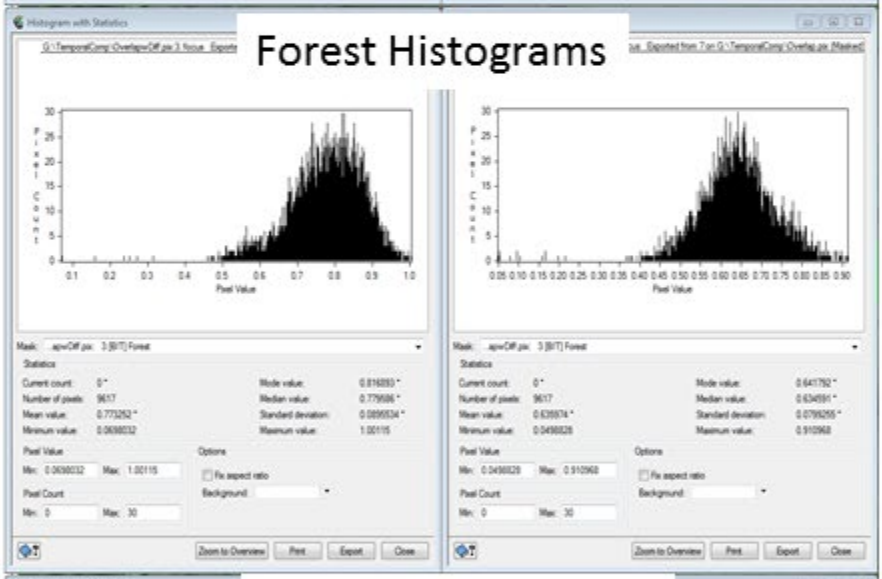

Clearcut Histograms

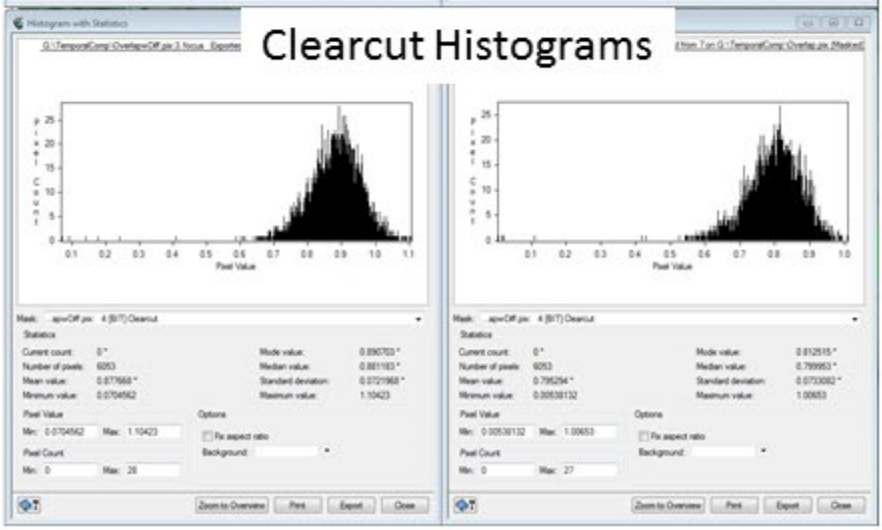

Luneburg Anisotropy

June 8

April 6

Fire Histograms

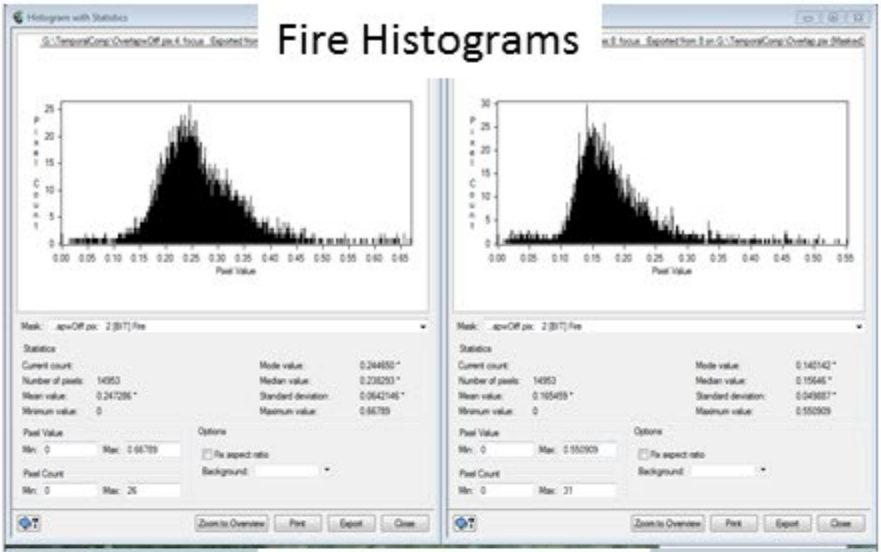

Forest Histograms

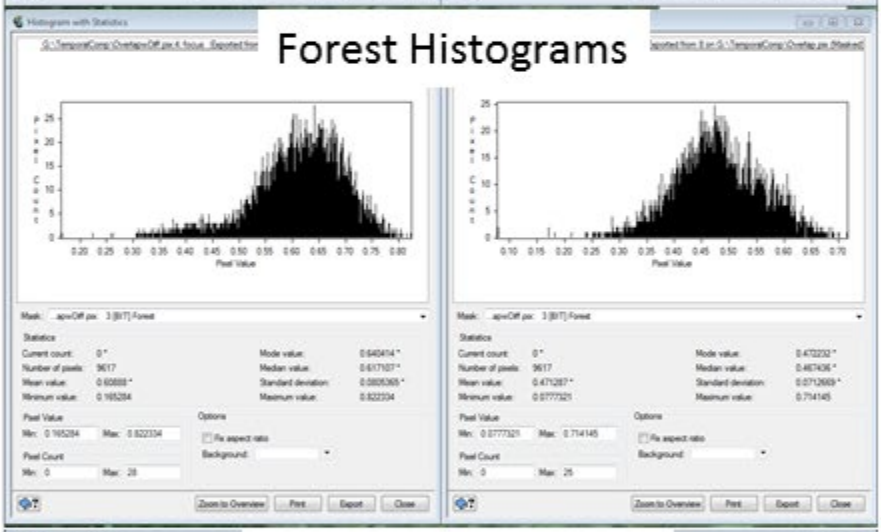

Clearcut Histograms

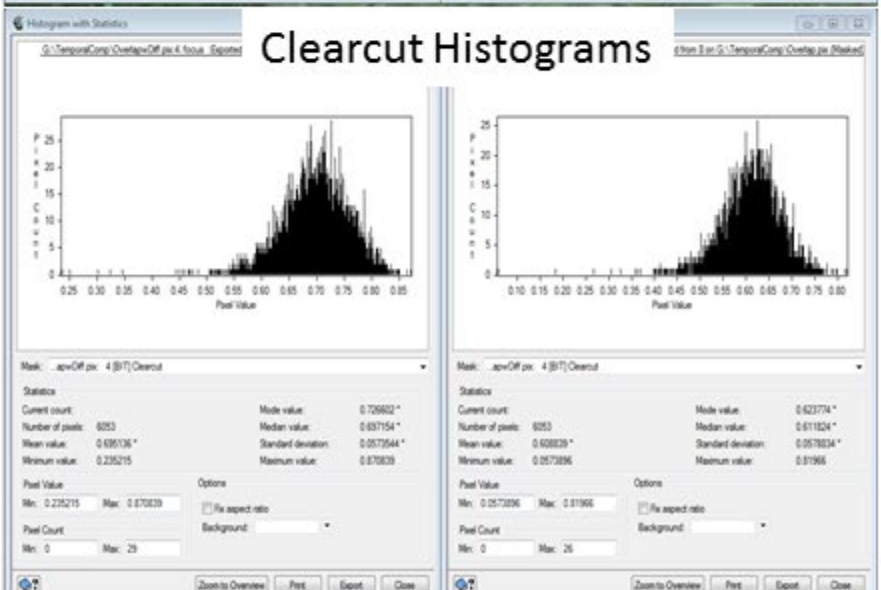

Appendix H. Maximum Likelihood Classification results for June 6, 2009 PALSAR image.

MLC Alpha Entropy RVI

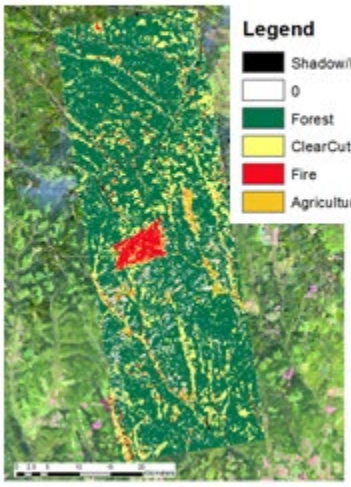

Code	Pixels	0	Forest	Clearcut	Fire	Agriculture
Forest	2752	0.44	97.6	1.96	0	0
Clearcut	1106	0	0.09	92.77	7.14	0
Fire	1814	3.53	0	2.43	93.94	0.11
Agriculture	236	2.12	0	3.81	0	94.07
Average	accuracy	=	94.59	%		
Overall	accuracy	=	95.43	%		

Kappa	Coefficient	=	0.931		
Standard	Deviation	=	0.004		
Confidence	Level	99%	0.931	+/-	0.011
		95%	0.931	+/-	0.008
		90%	0.931	+/-	0.007

MLC Alpha Entropy Luneburg Anisotropy

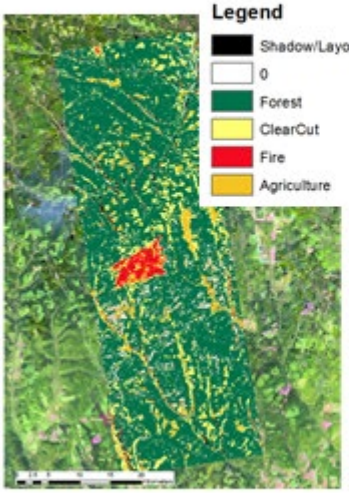

			Forest	Clearcut	Fire	Agriculture
Forest	2752	1.6	96.69	1.71	0	0
Clearcut	1106	0.36	0	84.36	0.45	14.83
Fire	1814	3.97	0	1.49	85.34	9.21
Agriculture	236	0	0	11.02	0.85	88.14
Average	accuracy	=	88.63	%		
Overall	accuracy	=	90.56	%		

Kappa	Coefficient	=	0.86		
Standard	Deviation	=	0.005		
Confidence	Level	99%	0.86	+/-	0.014
		95%	0.86	+/-	0.011
		90%	0.86	+/-	0.009

MLC Alpha Entropy RVI
Luneburg Anisotropy

Code	Pixels	Forest	Clearcut	Fire	Agriculture
Forest	2752	98	2	0	0
Clearcut	1106	0.18	96.84	2.98	0
Fire	1814	0	1.16	98.46	0.39
Agriculture	236	0	1.69	0	98.31
Average	Accuracy	=	97.9	%	
Overall	Accuracy	=	97.94	%	

Kappa	Coefficient	=	0.96845	
Standard	Deviation	=	0.00282	
Confidence	Level			
	99%	0.968	+/-	0.007
	95%	0.968	+/-	0.006
	90%	0.968	+/-	0.005

Appendix I. LOGIT Classification results for June 6, 2009 PALSAR image.

Logit Alpha Entropy RVI

Name	Pixels	Forest	Clearcut	Fire	Agriculture
Forest	2752	99.1	0.9	0	0
Clearcut	1106	33.9	63.1	3	0
Fire	1814	0.2	0.7	99.1	0
Agriculture	236	1.7	0	11.9	86.4
Average	accuracy	=	86.93%		
Overall	accuracy	=	91.84%		

Kappa	Coefficient	=		0.87122	
Standard	Deviation	=		0.00554	
Confidence	Level		99%	0.87122	0.01
			95%	0.87122	0.01
			90%	0.87122	0.01

Logit Alpha Entropy Luneburg Anisotropy

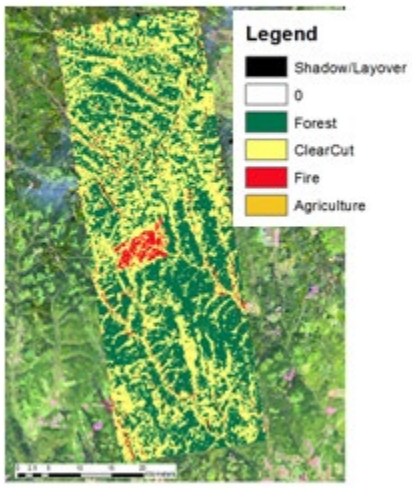

Name	Pixels	Forest	Clearcut	Fire	Agriculture
Forest	2752	69.1	30.8	0	0.1
Clearcut	1106	0	99.9	0.1	0
Fire	1814	1.5	11.2	87.2	0.1
Agriculture	236	5.9	88.1	5.9	0
Average	accuracy	=	64.05%		
Overall	accuracy	=	77.67%		

Kappa	Coefficient	=		0.67587	
Standard	Deviation	=		0.00757	
Confidence	Level		99%	0.67587	0.02
			95%	0.67587	0.01
			90%	0.67587	0.01

Logit Alpha Entropy RVI
Luneburg Anisotropy

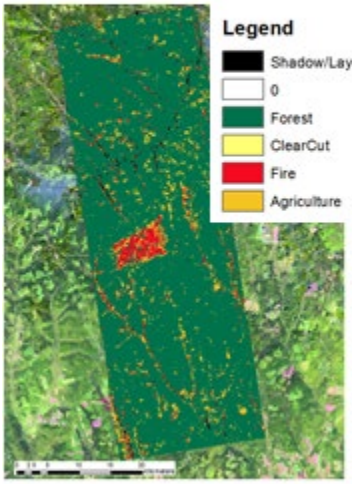

Name	Pixels	Forest	Clearcut	Fire	Agriculture
Forest	2752	99.6	0	0	0.4
Clearcut	1106	26.7	31.6	0.5	41.1
Fire	1814	12.2	0	86.8	1
Agriculture	236	37.3	16.5	1.3	44.9
Average	accuracy	=	65.73%		
Overall	accuracy	=	80.75%		

Kappa	Coefficient	=		0.69817
Standard	Deviation	=		0.00732
Confidence Level		99%	0.698	0.01888
		95%	0.698	0.01434
		90%	0.698	0.01204

Appendix J. MLC and LOGIT results for June 8, 2009 PALSAR image.

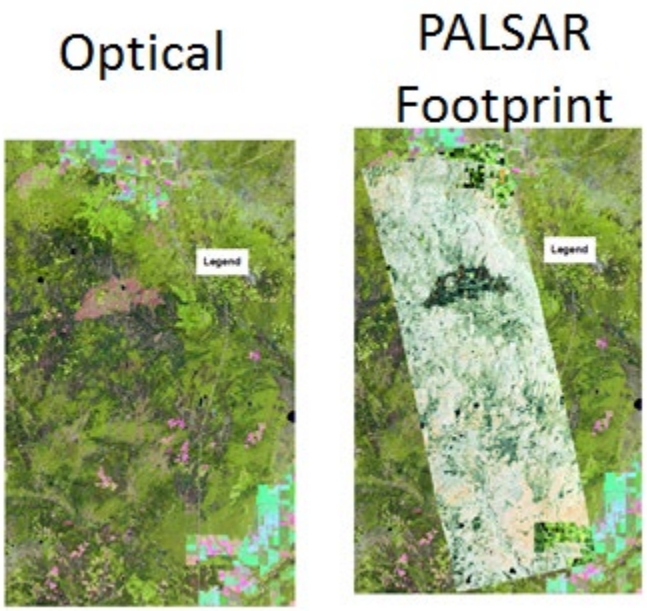

MLC Alpha Entropy RVI

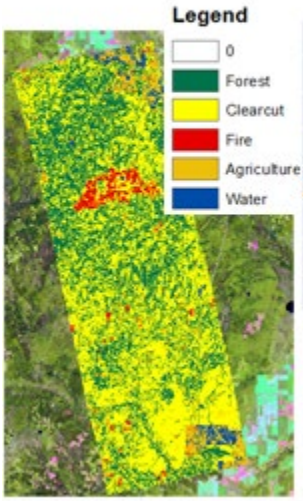

Code	Pixels	Forest	Clearcut	Fire	Agriculture	Water
Forest	760	96.32	3.68	0	0	0
Clearcut	1544	37.5	54.66	7.84	0	0
Fire	834	0	0.12	99.04	0.84	0
Agriculture	9037	0.73	2.28	2	65.36	29.62
Water	611	0	0	0	10.64	89.36
Average	accuracy	=	80.95	%		
Overall	accuracy	=	69.26	%		

Kappa	Coefficient	=	0.51591	
Standard	Deviation	=	0.00639	
	Confidence	Level	:	
	99%	0.516	+/-	0.016
	95%	0.516	+/-	0.013
	90%	0.516	+/-	0.011

MLC Alpha Entropy Luneburg Anisotropy

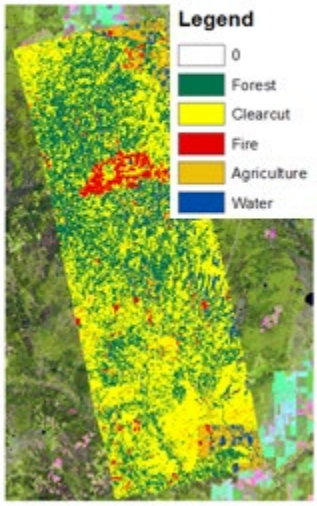

Code	Pixels	Forest	Clearcut	Fire	Agriculture	Water
Forest	760	95.66	3.42	0	0.26	0.66
Clearcut	1544	35.62	42.88	20.34	1.17	0
Fire	834	0	0.96	94.36	4.68	0
Agriculture	9037	0.76	4.01	9.16	76.04	10.03
Water	611	0	0.16	0	59.08	40.75
Average	accuracy	=	69.94	%		
Overall	accuracy	=	72.71	%		

Kappa	Coefficient	=	0.51829	
Standard	Deviation	=	0.00645	
	Confidence	Level	:	
	99%	0.518	+/-	0.017
	95%	0.518	+/-	0.013
	90%	0.518	+/-	0.011

MLC Alpha Entropy RVI Luneburg Anisotropy

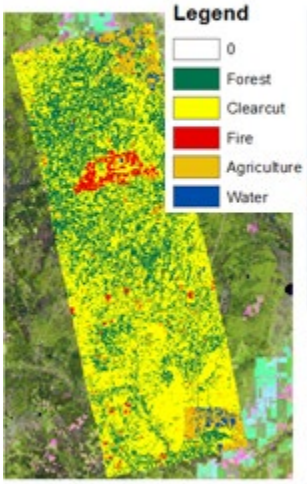

Code	Pixels	Forest	Clearcut	Fire	Agriculture	Water
Forest	760	94.87	5.13	0	0	0
Clearcut	1544	33.23	55.83	10.82	0.13	0
Fire	834	0	0.12	97	2.88	0
Agriculture	9037	0.46	2.52	2.2	77.35	17.46
Water	611	0	0	0	23.24	76.76
Average	accuracy	=	80.36	%		
Overall	accuracy	=	77.05	%		

Kappa	Coefficient	=	0.60014	
Standard	Deviation	=	0.00617	
	Confidence	Level	:	
	99%	0.6	+/-	0.016
	95%	0.6	+/-	0.012
	90%	0.6	+/-	0.01

Logit Alpha Entropy RVI

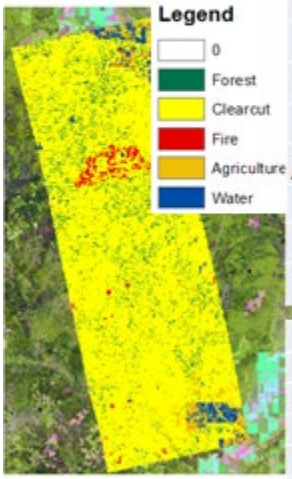

Code	Pixels	Forest	Clearcut	Fire	Agriculture	Water
Forest	760	28.7	71.3	0	0	0
Clearcut	1544	5.7	93.5	0.7	0.1	0
Fire	834	0	7.9	90.8	1.3	0
Agriculture	9037	0.4	3.6	0.8	54.6	40.7
Water	611	0	0	0	5.6	94.4
Average	accuracy	=	72.39%			
Overall	accuracy	=	61.99%			

Kappa	Coefficient	=	0.44163
Standard	Deviation	=	0.00671
Confidence	Level	:	
99%	0.44163	+/-	0.0173
95%	0.44163	+/-	0.01314
90%	0.44163	+/-	0.01103

Logit Alpha Entropy Luneburg Anisotropy

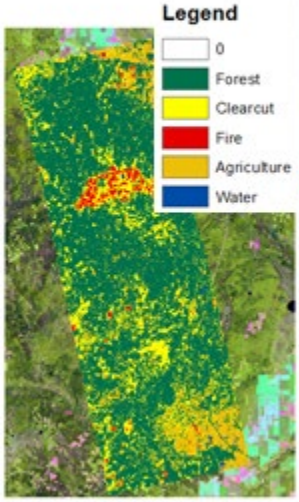

	Pixels	Forest	Clearcut	Fire	Agriculture	Water
Forest	760	98.3	0.1	0	1.6	0
Clearcut	1544	58.4	38.7	2.6	0.4	0
Fire	834	0	4.2	84.3	11.5	0
Agriculture	9037	1.9	11.2	6.9	78.9	1.1
Water	611	0	7.4	0	68.9	23.7
Average	accuracy	=	64.78%			
Overall	accuracy	=	72.94%			

Kappa	Coefficient	=	0.50237
Standard	Deviation	=	0.00656
Confidence	Level	:	
99%	0.50237	+/-	0.01693
95%	0.50237	+/-	0.01286
90%	0.50237	+/-	0.0108

Logit Alpha, RVI, Entropy, Luneburg Anisotropy

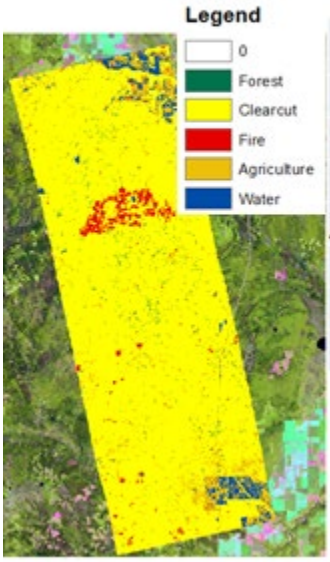

	Pixels	Forest	Clearcut	Fire	Agriculture	Water
Forest	760	12.1	87.9	0	0	0
Clearcut	1544	0	97.2	2.7	0.1	0
Fire	834	0	1.4	95.2	3.4	0
Agriculture	9037	0.1	2.8	1.7	53.7	41.8
Water	611	0	0	0	1.6	98.4
Average	accuracy	=	71.32%			
Overall	accuracy	=	61.32%			

Kappa	Coefficient	=	0.43516
Standard	Deviation	=	0.00671
Confidence	Level	:	
99%	0.43516	+/-	0.01731
95%	0.43516	+/-	0.01315
90%	0.43516	+/-	0.01104

Appendix K. MLC and LOGIT results for May 15, 2009 South PALSAR image

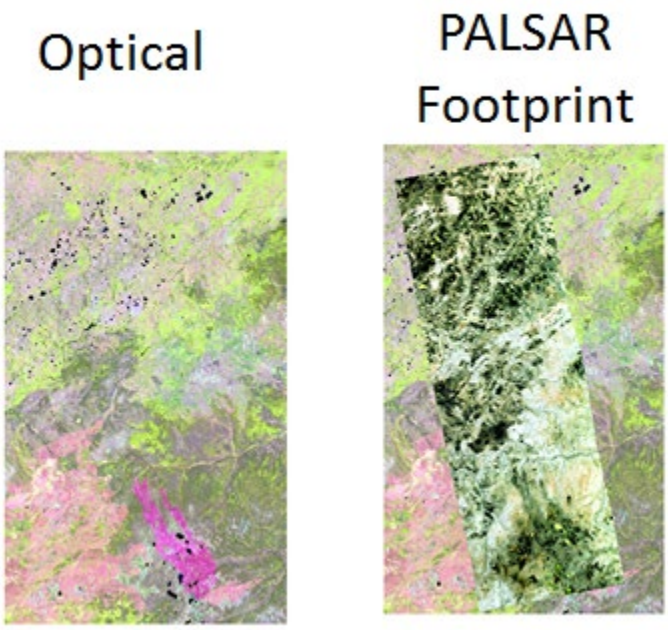

MLC Alpha Entropy RVI

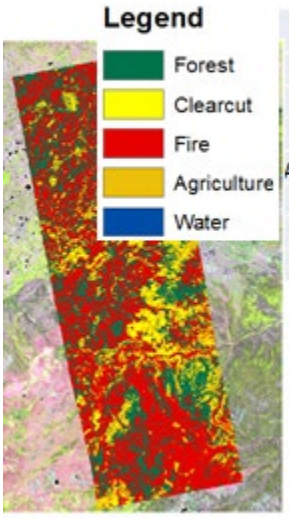

Code	Pixels	Forest	Clearcut	Fire	Agriculture	Water
Forest	3875	82.04	0	17.26	0	0.7
Clearcut	1007	0	100	0	0	0
Fire	2179	11.93	0	88.07	0	0
Agriculture	0	0	0	0	0	0
Water	266	0	0	0	0	100
Average	accuracy	=	92.53	%		
Overall	accuracy	=	86.95	%		

Kappa	Coefficient	=	0.7917	
Standard	Deviation	=	0.00645	
	Confidence	Level	:	
	99%	0.7917	+/-	0.01665
	95%	0.7917	+/-	0.01265
	90%	0.7917	+/-	0.01061

MLC Alpha Entropy Luneburg Anisotropy

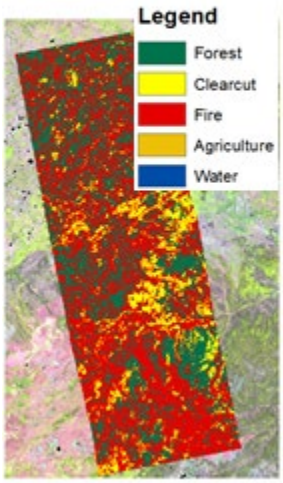

Code	Pixels	Forest	Clearcut	Fire	Agriculture	Water
Forest	3875	64.62	0	34.14	0	1.24
Clearcut	1007	0	98.51	0	0	1.49
Fire	2179	10.46	0	85.59	0	3.95
Agriculture	0	0	0	0	0	0
Water	266	0	0	0	0	100
Average	accuracy	=	87.18	%		
Overall	accuracy	=	76.8	%		

Kappa	Coefficient	=	0.64455	
Standard	Deviation	=	0.00787	
	Confidence	Level	:	
	99%	0.64455	+/-	0.0203
	95%	0.64455	+/-	0.01542
	90%	0.64455	+/-	0.01294

MLC Alpha Entropy RVI Luneburg Anisotropy

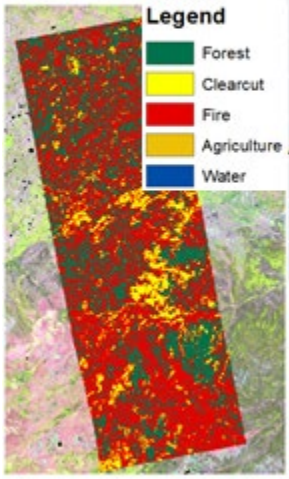

	Pixels	Forest	Clearcut	Fire	Agriculture	Water
Forest	3875	81.73	0	17.55	0	0.72
Clearcut	1007	0	100	0	0	0
Fire	2179	11.11	0	88.89	0	0
Agriculture	0	0	0	0	0	0
Water	266	0	0	0	0	100
Average	accuracy	=	92.66	%		
Overall	accuracy	=	87.03	%		

Kappa	Coefficient	=	0.79333	
Standard	Deviation	=	0.00642	
	Confidence	Level	:	
	99%	0.79333	+/-	0.01656
	95%	0.79333	+/-	0.01258
	90%	0.79333	+/-	0.01056

Logit Alpha Entropy RVI

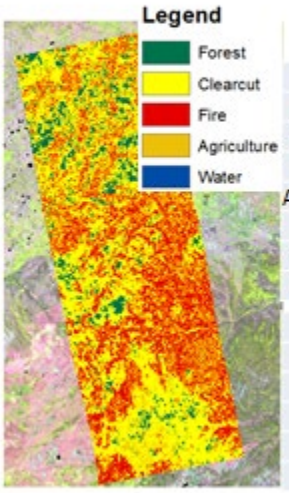

Name	Pixels	Forest	Clearcut	Fire	Agriculture	Water
Forest	3875	17.6	7.8	63.8	0	10.7
Clearcut	1007	0	78.6	0	0	21.4
Fire	2179	4.2	0.5	94.7	0	0.6
Agriculture	0	0	0	0	0	0
Water	266	0	63.9	0	0	36.1
Average	accuracy	=	56.77%			
Overall	accuracy	=	49.61%			

Kappa	Coefficient	=	0.31196
Standard	Deviation	=	0.00961
	Confidence	Level	:
	99%	0.31196	0.02479
	95%	0.31196	0.01883
	90%	0.31196	0.0158

Logit Alpha Entropy Luneburg Anisotropy

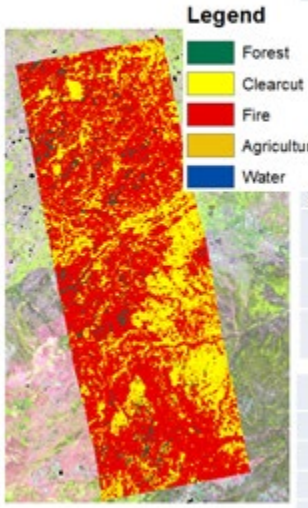

	Pixels	Forest	Clearcut	Fire	Agriculture	Water
Forest	3875	40	37.6	15.8	0	6.6
Clearcut	1007	0	88.5	11.5	0	0
Fire	2179	9.5	73.2	15.1	0	2.1
Agriculture	0	0	0	0	0	0
Water	266	0	6.4	0	0	93.6
Average	accuracy	=	59.32%			
Overall	accuracy	=	41.23%			

Kappa	Coefficient	=	0.21972
Standard	Deviation	=	0.00952
	Confidence	Level	:
	99%	0.21972	0.02457
	95%	0.21972	0.01866
	90%	0.21972	0.01566

Appendix L. MLC and LOGIT results for May 15, 2009 North PALSAR image

Optical

PALSAR Footprint

MLC Alpha Entropy RVI

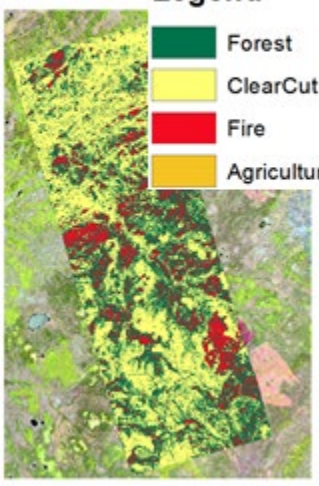

	Pixels	Forest	Clearcut	Fire	Agriculture
Forest	8812	54.12	9.44	36.44	0
Clearcut	1357	3.32	96.54	0.15	0
Fire	2563	27.16	0.31	72.53	0
Agriculture	0	0	0	0	0
Average	accuracy	=	74.4	%	
Overall	accuracy	=	62.35	%	

Kappa	Coefficient	=	0.375	
Standard	Deviation	=	0.008	
	Confidence	Level	:	
	99%	0.375	+/-	0.02044
	95%	0.375	+/-	0.01553
	90%	0.375	+/-	0.01303

MLC Alpha Entropy Luneburg Anisotropy

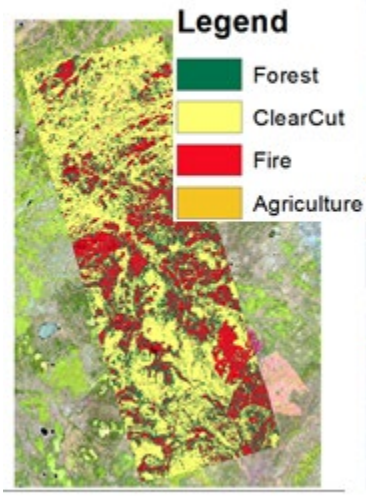

	Pixels	Forest	Clearcut	Fire	Agriculture
Forest	8812	59.92	9.74	30.34	0
Clearcut	1357	3.61	96.24	0.15	0
Fire	2563	30.94	0.23	68.83	0
Agriculture	0	0	0	0	0
Average	accuracy	=	75	%	
Overall	accuracy	=	65.58	%	

Kappa	Coefficient	=	0.405	
Standard	Deviation	=	0.008	
	Confidence	Level	:	
	99%	0.405	+/-	0.02003
	95%	0.405	+/-	0.01522
	90%	0.405	+/-	0.01277

MLC Alpha Entropy RVI Luneburg Anisotropy

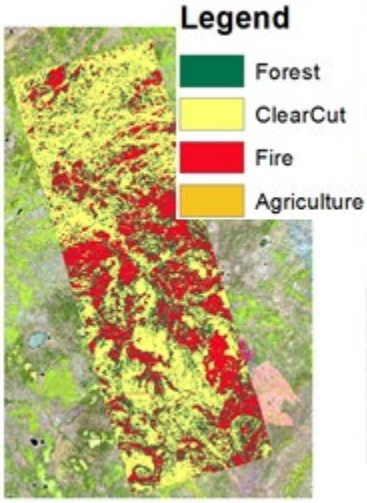

Code	Pixels	Forest	Clearcut	Fire	Agriculture
Forest	8812	21.28	9.74	68.99	0
Clearcut	1357	2.65	96.83	0.52	0
Fire	2563	6.55	0.31	93.13	0
Agriculture	0	0	0	0	0
Average	accuracy	=	70.41	%	
Overall	accuracy	=	43.8	%	

Kappa	Coefficient	=	0.235	
Standard	Deviation	=	0.01	
	Confidence	Level	:	
	99%	0.235	+/-	0.02504
	95%	0.235	+/-	0.01902
	90%	0.235	+/-	0.01597

Logit Alpha Entropy RVI

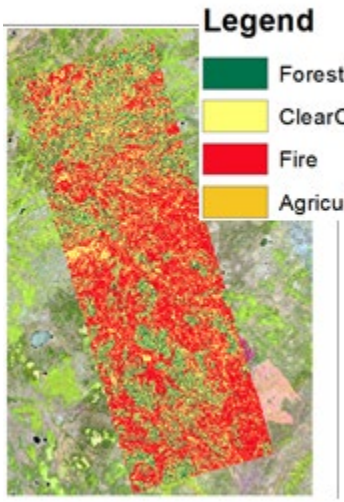

Name	Pixels	Forest	Clearcut	Fire	Agriculture
Forest	8812	1.3	27.9	70.8	0
Clearcut	1357	43	49.4	7.7	0
Fire	2563	0	35.4	64.6	0
Agriculture	0	0	0	0	0
Average	accuracy	=	38.42%		
Overall	accuracy	=	19.16%		

Kappa	Coefficient	=	-0.008
Standard	Deviation	=	0.0114
	Confidence	Level	:
	99%	-0.01	0.0295
	95%	-0.01	0.0224
	90%	-0.01	0.0188

Logit Alpha Entropy Luneburg Anisotropy

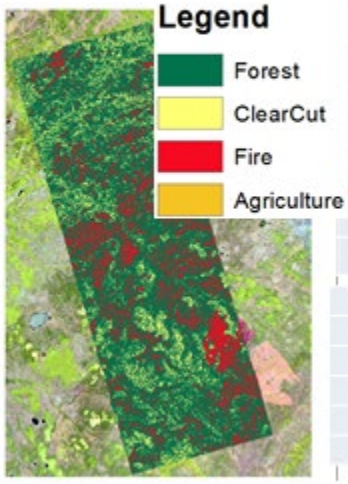

Name	Pixels	Forest	Clearcut	Fire	Agriculture
Forest	8812	53.5	0.3	46.2	0
Clearcut	1357	56.8	42.8	0.4	0
Fire	2563	22.2	0	77.8	0
Agriculture	0	0	0	0	0
Average	accuracy	=	58.06%		
Overall	accuracy	=	57.28%		

Kappa	Coefficient	=	0.2502
Standard	Deviation	=	0.0091
	Confidence	Level	:
	99%	0.25	0.0235
	95%	0.25	0.0179
	90%	0.25	0.015

Logit Alpha Entropy RVI
Luneburg Anisotropy

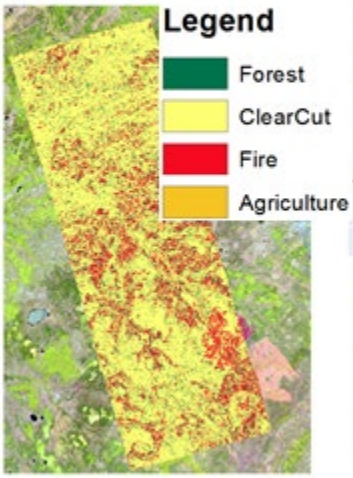

Name	Pixels	Forest	Clearcut	Fire	Agriculture
Forest	8812	16.8	42.9	40.3	0
Clearcut	1357	3.5	96.1	0.4	0
Fire	2563	7.3	40.7	52	0
Agriculture	0	0	0	0	0
Average	accuracy	=	54.95%		
Overall	accuracy	=	32.33%		

Kappa	Coefficient	=	0.1303
Standard	Deviation	=	0.0091
	Confidence	Level	:
	99%	0.13	0.0235
	95%	0.13	0.0178
	90%	0.13	0.015

Appendix M. PALSAR May15 North Classification Results for 4 Fire Classes

MLC Alpha Entropy RVI

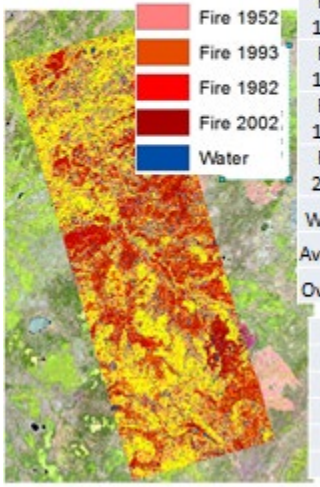

Code	Pixels	Forest	Clearcut	Fire 1952	Fire 1993	Fire 1982	Fire 2002	Water
Forest	5936	4.35	20.81	22.12	24.53	2.85	15.52	9.84
Clearcut	1985	2.72	57.53	14.31	17.93	2.42	1.61	3.48
Fire 1952	3651	3.29	34.48	28.51	16.63	2.41	3.37	11.31
Fire 1993	1898	2.42	6.64	3.58	52.95	3.9	27.24	3.27
Fire 1982	6926	1.76	15.13	11.33	29.8	10.92	25.22	5.83
Fire 2002	2541	1.61	0.2	0.79	20.35	4.25	67.73	5.08
Water	450	6.67	9.33	7.78	1.11	4	11.11	60
Averageaccuracy		=	40.28	%				
Overall accuracy		=	26.48	%				

Kappa	Coefficient	=	0.17325	
Standard	Deviation	=	0.00357	
	Confidence	Level	:	
	99%	0.173	+/-	0.00921
	95%	0.173	+/-	0.007
	90%	0.173	+/-	0.00587

MLC Alpha Entropy Luneburg Anisotropy

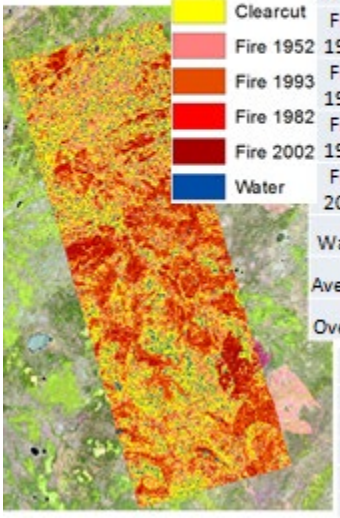

Code	Pixels	Forest	Clearcut	Fire 1952	Fire 1993	Fire 1982	Fire 2002	Water
Forest	5936	1.31	23.58	24.65	29.9	1.97	14.66	3.93
Clearcut	1985	0.45	47.91	17.03	27.2	0.2	1.21	5.99
Fire 1952	3651	1.45	33.22	34.95	23.14	0.9	3.1	3.23
Fire 1993	1898	0.21	3.79	4.95	63.33	1.69	25.97	0.05
Fire 1982	6926	0.71	15.61	12.59	36.63	5.18	27.36	1.92
Fire 2002	2541	0.55	0.12	1.53	26.76	2.2	68.24	0.59
Water	450	1.33	23.56	3.78	1.56	8	10.44	51.33
Averageaccuracy		=	38.89	%				
Overall accuracy		=	24.93	%				

Kappa	Coefficient	=	0.16002	
Standard	Deviation	=	0.00365	
	Confidence	Level	:	
	99%	0.16	+/-	0.00942
	95%	0.16	+/-	0.00716
	90%	0.16	+/-	0.00601

MLC Alpha Entropy RVI Luneburg Anisotropy

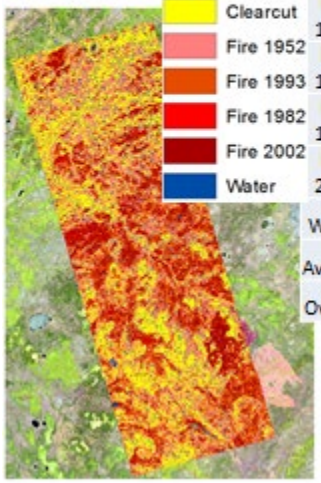

Code	Pixels	Forest	Clearcut	Fire 1952	Fire 1993	Fire 1982	Fire 2002	Water
Forest	5936	0.57	15.21	31.01	23.47	1.23	23.2	0
Clearcut	1985	0.25	47.76	21.86	22.57	1.01	2.87	0
Fire 1952	3651	0.22	23.17	44.92	20.27	0.96	6.08	0
Fire 1993	1898	0.11	3.64	4.64	49.1	0.68	40.99	0
Fire 1982	6926	0.17	9.95	17.35	28.66	7.87	33.54	0
Fire 2002	2541	0.24	0.04	2.01	13.07	1.77	81.86	0
Water	450	1.11	8.22	12.89	1.56	0.67	15.11	0
Averageaccuracy	=	41.79	%					
Overall accuracy	=	27.58	%					

Kappa	Coefficient	=	0.18504	
Standard	Deviation	=	0.00364	
	Confidence	Level	:	
	99%	0.185	+/-	0.00938
	95%	0.185	+/-	0.00713
	90%	0.185	+/-	0.00598

Logit Alpha Entropy RVI

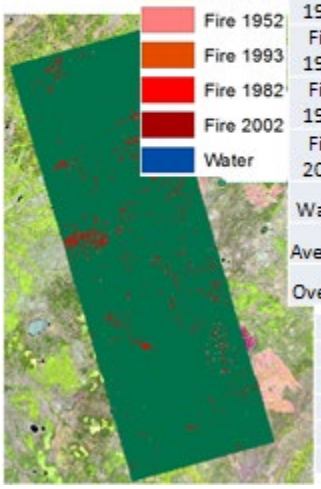

	Pixels	Forest	Clearcut	Fire 1952	Fire 1993	Fire 1982	Fire 2002	Water
Forest	5936	97.7	0	0	0	2.2	0	0.1
Clearcut	1985	99.9	0	0	0	0.1	0	0
Fire 1952	3651	99.8	0	0	0	0.2	0	0
Fire 1993	1898	97.2	0	0	0	2.7	0	0.1
Fire 1982	6926	83.4	0	0	0	16.5	0	0.1
Fire 2002	2541	85.2	0	0	0	12.2	0	2.6
Water	450	84	0	0	0	13.3	0	2.7
Averageaccuracy	=	29.21%						
Overall accuracy	=	45.45%						

Kappa	Coefficient	=	0.32338
Standard	Deviation	=	0.01449
	Confidence	Level	:
	99%	0.323	0.03739
	95%	0.323	0.0284
	90%	0.323	0.02384

Logit Alpha Entropy Luneburg Anisotropy

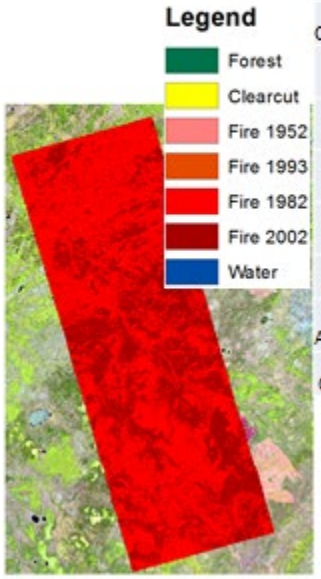

Name	Pixels	Forest	Clearcut	Fire 1952	Fire 1993	Fire 1982	Fire 2002	Wate
Forest	5936	0	0	0	0	50.7	49.3	0
Clearcut	1985	0	0	0	0	74.4	25.6	0
Fire 1952	3651	0	0	0	0	67.2	32.8	0
Fire 1993	1898	0	0	0	0	10.4	89.6	0
Fire 1982	6926	0	0	0	0	34.3	65.7	0
Fire 2002	2541	0	0	0	0	1.3	98.7	0
Water	450	0	0	0	0	72.4	27.6	0
Average accuracy	=	26.61%						
Overall accuracy	=	25.04%						

Kappa	Coefficient	=	-0.0268
Standard	Deviation	=	0.00808
	Confidence	Level	:
	99%	-0.027	0.02084
	95%	-0.027	0.01583
	90%	-0.027	0.01328

Logit Alpha Entropy Luneburg Anisotropy

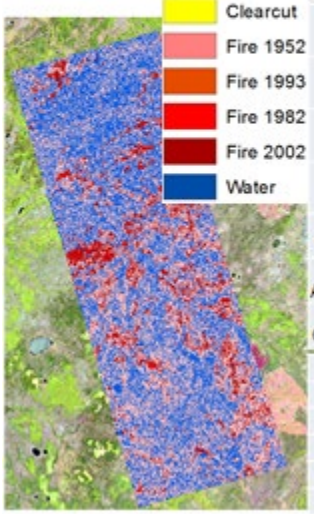

		Forest	Clearcut	Fire 1952	Fire 1993	Fire 1982	Fire 2002	Water
Forest	5936	0	0	46.5	0	0.2	13.2	40
Clearcut	1985	0	0	64.7	0	0	1.7	33.6
Fire 1952	3651	0	0	50.6	0	0	2.4	47
Fire 1993	1898	0	0	68.3	0	0.2	23.8	7.6
Fire 1982	6926	0	0	45.2	0	6.7	27.8	20.2
Fire 2002	2541	0	0	46.4	0	1.3	47.2	5
Water	450	0	0	8.2	0	6.4	12.9	72.4
Averageaccuracy	=	35.40%						
Overall accuracy	=	19.68%						

Kappa	Coefficient	=	0.10173
Standard	Deviation	=	0.00582
	Confidence	Level	:
	99%	0.102	0.01501
	95%	0.102	0.0114
	90%	0.102	0.00957

Appendix N. PALSAR May15 North Classification Results for 2 Fire Classes with Additional Input Channels

Optical

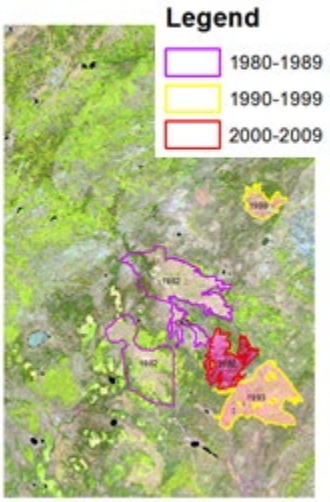

Palsar Footprint

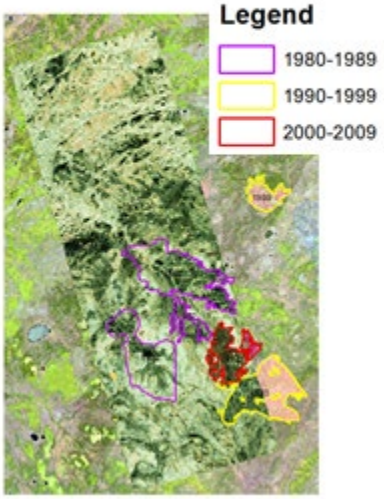

MLC Alpha Entropy RVI

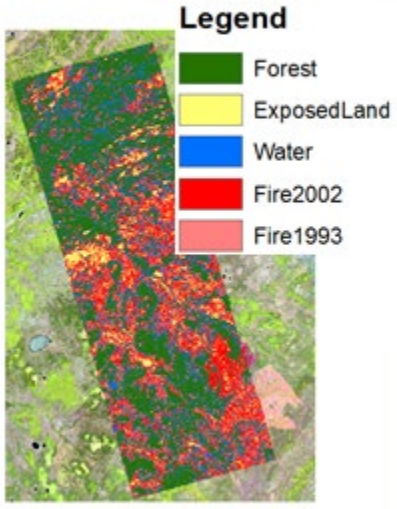

	Pixels	Forest	ExposedLand	Water	Fire2002	Fire1993
Forest	1371	88.91	0	10.8	0.22	0.07
ExposedLand	483	0	89.03	0	9.11	1.86
Water	533	7.5	0	90.24	0.38	1.88
Fire2002	1386	0	17.82	0.29	77.42	4.47
Fire1993	784	1.4	4.21	3.06	15.69	75.64
Average	accuracy	=	84.25	%		
Overall	accuracy	=	83.3	%		

Kappa	Coefficient	=	0.7843	
Standard	Deviation	=	0.00707	
	Confidence	Level	:	
	99%	0.7843	+/-	0.018
	95%	0.7843	+/-	0.014
	90%	0.7843	+/-	0.012

MLC Alpha, Pedestal Height, RCS

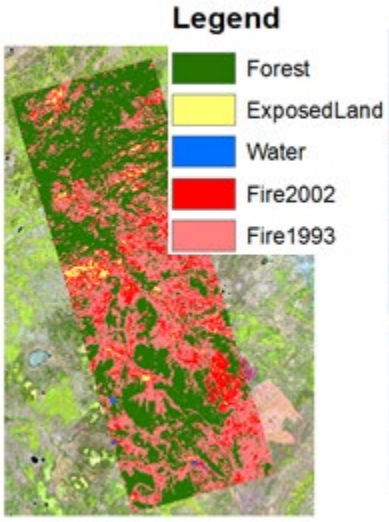

	Pixels	Forest	ExposedLand	Water	Fire 2002	Fire 1993
Forest	1371	100	0	0	0	0
ExposedLand	483	0	92.96	0	7.04	0
Water	533	0	0	100	0	0
Fire2002	1386	0	3.32	0	92.64	4.04
Fire1993	784	0	0	0	1.91	98.09
Average	accuracy	=	96.74	%		
Overall	accuracy	=	96.69	%		

Kappa	Coefficient	=	0.95664	
Standard	Deviation	=	0.00347	
	Confidence	Level	:	
	99%	0.957	+/-	0.009
	95%	0.957	+/-	0.007
	90%	0.957	+/-	0.006

MLC Alpha, Entropy, Luneburg Anisotropy

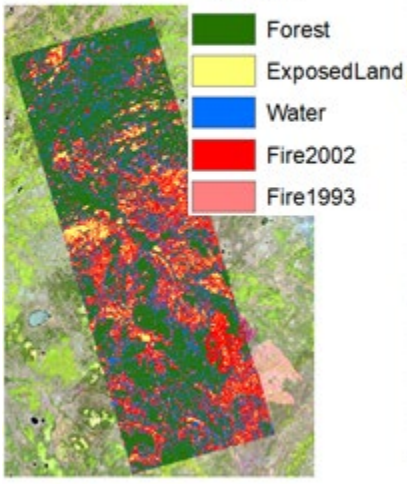

	Pixels	Forest	ExposedLand	Water	Fire 2002	Fire 1993
Forest	1371	90.96	0	8.83	0.22	0
ExposedLand	483	0	91.3	0	7.45	1.24
Water	533	11.63	0	87.24	0	1.13
Fire2002	1386	0	19.84	0.36	77.27	2.53
Fire1993	784	1.28	4.72	4.08	20.28	69.64
Average	accuracy	=	83.28	%		
Overall	accuracy	=	82.73	%		

Kappa	Coefficient	=	0.77639	
Standard	Deviation	=	0.00717	
	Confidence	Level	:	
	99%	0.776	+/-	0.018
	95%	0.776	+/-	0.014
	90%	0.776	+/-	0.012

MLC Alpha, Entropy, RVI, Luneburg Anisotropy

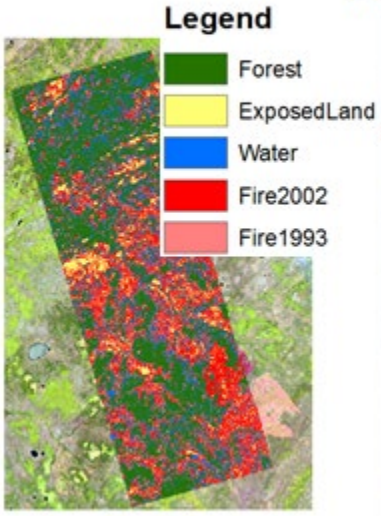

	Pixels	Forest	Exposed Land	Water	Fire 2002	Fire 1993
Forest	1371	89.57	0	9.92	0.07	0.44
Exposed Land	483	0	90.06	0	8.7	1.24
Water	533	7.88	0	90.43	0.19	1.5
Fire2002	1386	0	18.25	0.43	79	2.31
Fire1993	784	1.15	4.34	2.81	17.09	74.62
Average	accuracy	=	84.74	%		
Overall	accuracy	=	83.94	%		

Kappa	Coefficient	=	0.79224	
Standard	Deviation	=	0.00697	
	Confidence	Level	:	
	99%	0.792	+/-	0.018
	95%	0.792	+/-	0.014
	90%	0.792	+/-	0.011

MLC Alpha, Entropy, RVI, Luneburg Anisotropy, Pedestal Height, RCSmax

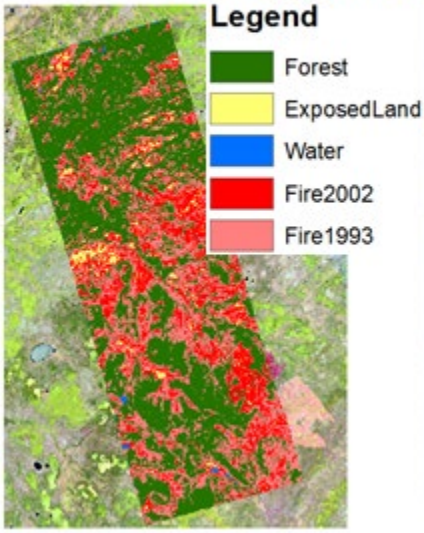

	Pixels	Forest	ExposedLand	Water	Fire 2002	Fire 1993
Forest	1371	100	0	0	0	0
ExposedLand	483	0	94.62	0	5.38	0
Water	533	0	0	100	0	0
Fire2002	1386	0	4.55	0	95.02	0.43
Fire1993	784	0.51	0	0	1.66	97.83
Average	accuracy	=	97.49	%		
Overall	accuracy	=	97.54	%		

Kappa	Coefficient	=	0.96782	
Standard	Deviation	=	0.003	
	Confidence	Level	:	
	99%	0.968	+/-	0.008
	95%	0.968	+/-	0.006
	90%	0.968	+/-	0.005

Appendix O. PALSAR May15 North Classification Results for 3 Fire Classes with Additional Input Channels

Optical

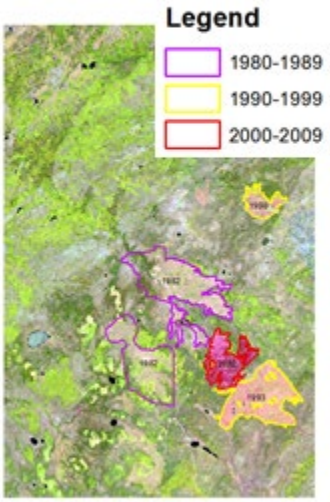

PALSAR Footprint

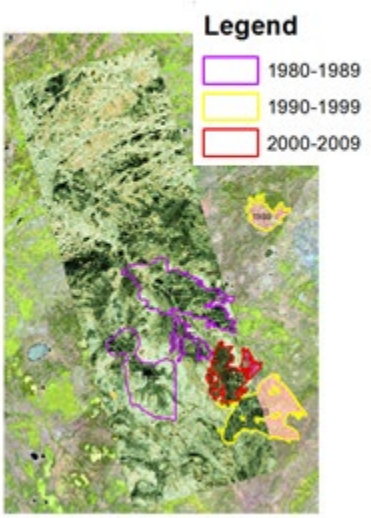

MLC Alpha Entropy RVI

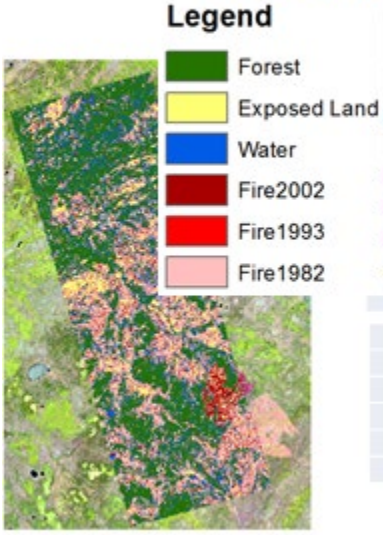

Code	Pixels	Forest	ExposedLand	Water	Fire 2002	Fire 1993	Fire 1982
Forest	1371	88.91	0	10.72	0.07	0	0.29
posedLand	483	0	84.89	0	2.69	1.45	10.97
Water	533	7.5	0	88.74	0	0.38	3.38
Fire2002	1386	0	14.29	0.29	54.33	1.44	29.65
Fire1993	784	1.28	3.19	2.42	3.19	63.65	26.28
Fire1982	1232	1.79	21.83	2.19	14.45	0.65	59.09
Average	accuracy	=	73.27	%			
Overall	accuracy	=	70.51	%			

Kappa	Coefficient	=	0.63982	
Standard	Deviation	=	0.0073	
	Confidence	Level	:	
	99%	0.64	+/-	0.019
	95%	0.64	+/-	0.014
	90%	0.64	+/-	0.012

MLC Alpha, Pedestal Height, RCS

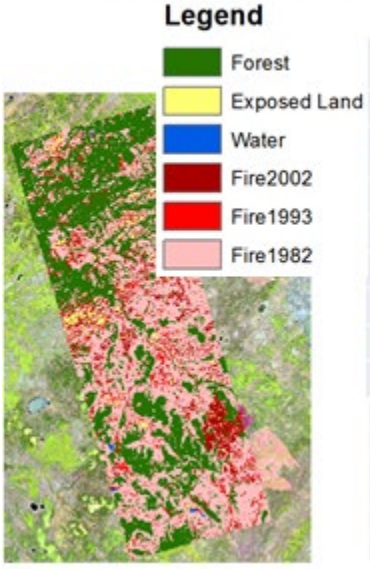

	Pixels	Forest	ExposedLand	Water	Fire 2002	Fire 1993	Fire 1982
Forest	1371	99.64	0	0	0	0	0.36
Exposed Land	483	0	92.75	0	6.21	0	1.04
Water	533	0	0	100	0	0	0
Fire2002	1386	0	3.17	0	81.1	1.08	14.65
Fire1993	784	0	0	0	1.15	74.62	24.23
Fire1982	1232	0	1.14	0	30.93	4.71	63.23
Average	accuracy	=	85.22	%			
Overall	accuracy	=	83.52	%			

Kappa	Coefficient	=	0.79545	
Standard	Deviation	=	0.0061	
	Confidence	Level	:	
	99%	0.795	+/-	0.016
	95%	0.795	+/-	0.012
	90%	0.795	+/-	0.01

MLC Alpha, Entropy, RVI, Luneburg Anisotropy, Pedestal Height, RCSmax

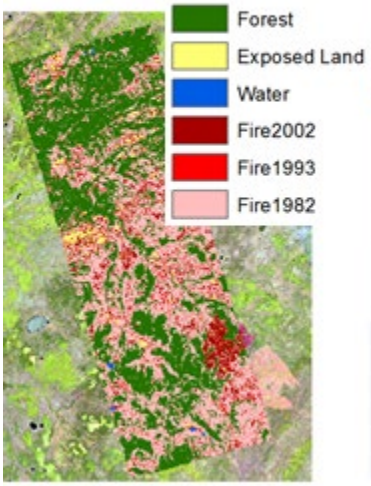

Code	Pixels	Forest	ExposedLand	Water	Fire 2002	Fire 1993	Fire 1982
Forest	1371	99.93	0	0	0	0	0.07
ExposedLand	483	0	93.37	0	4.76	0	1.86
Water	533	0	0	100	0	0	0
Fire2002	1386	0	4.4	0	85.35	0	10.25
Fire1993	784	0.38	0	0	0.26	74.23	25.13
Fire1982	1232	0.08	1.54	0	34.66	0.41	63.31
Average	accuracy	=	86.03	%			
Overall	accuracy	=	84.63	%			

Kappa	Coefficient	=	0.80897	
Standard	Deviation	=	0.00592	
	Confidence	Level	:	
	99%	0.809	+/-	0.015
	95%	0.809	+/-	0.012
	90%	0.809	+/-	0.01

Appendix P. PALSAR May 15 South Classification Results for 4 Fire Classes

MLC Alpha, Entropy, RVI

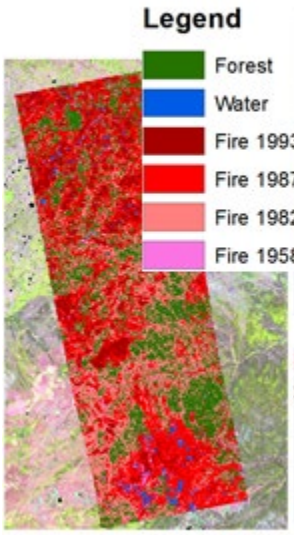

Code	Pixels	Forest	Water	Fire 1993	Fire 1987	Fire 1982	Fire 1958
Forest	1714	71.47	0	0	5.13	23.1	0.29
Water	557	0	98.38	0	0	0	1.62
Fire 1993	248	0	0	85.89	14.11	0	0
Fire 1987	2632	1.48	0.19	15.46	71.12	11.7	0.04
Fire 1982	841	18.55	0	0	3.69	77.65	0.12
Fire 1958	1081	39.22	0	0	0.46	6.38	53.93
Average	accuracy	=	76.41	%			
Overall	accuracy	=	72.02	%			

Kappa	Coefficient	=	0.643	
Standard	Deviation	=	0.007	
	Confidence	Level	:	
	99%	0.643+/-		0.01736
	95%	0.643+/-		0.01319
	90%	0.643+/-		0.01107

MLC Alpha, Pedestal Height, RCS Max

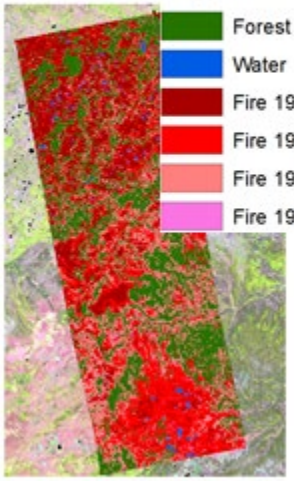

Code		Forest	Water	Fire 1993	Fire 1987	Fire 1982	Fire 1958
Forest	1714	77.36	0	0.82	5.54	15.81	0.47
Water	557	0	96.77	0	0	0	3.23
Fire 1993	248	0	0	95.16	4.84	0	0
Fire 1987	2632	0.46	0	11.63	77.85	8.7	1.37
Fire 1982	841	16.77	0	0	8.68	74.2	0.36
Fire 1958	1081	36.26	0	0	0.74	9.07	53.93
Average	accuracy	=	79.21	%			
Overall	accuracy	=	75.74	%			

Kappa	Coefficient	=	0.687	
Standard	Deviation	=	0.006	
	Confidence	Level	:	
	99%	0.687	+/-	0.01674
	95%	0.687	+/-	0.01272
	90%	0.687	+/-	0.01067

MLC Alpha, Entropy, Pedestal Height, RCS Max

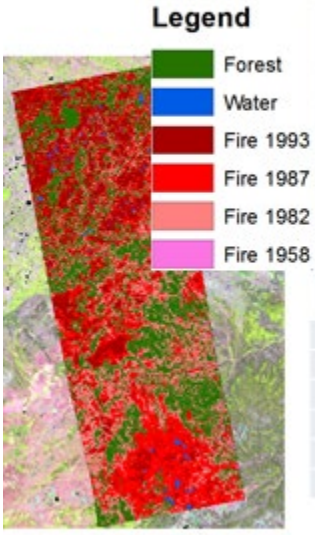

		Forest	Water	Fire 1993	Fire 1987	Fire 1982	Fire 1958
Forest	1714	77.48	0	0.82	1.34	19.31	1.05
Water	557	0	100	0	0	0	0
Fire 1993	248	0	0	94.76	5.24	0	0
Fire 1987	2632	0.84	0	14.82	70.17	14.13	0.04
Fire 1982	841	16.29	0	0	4.88	78.48	0.36
Fire 1958	1081	37.65	0	0	0	8.14	54.21
Average	accuracy	=	79.18	%			
Overall	accuracy	=	73.7	%			

Kappa	Coefficient	=	0.666	
Standard	Deviation	=	0.007	
	Confidence	Level	:	
	99%	0.666	+/-	0.01692
	95%	0.666	+/-	0.01285
	90%	0.666	+/-	0.01078

MLC Alpha, Entropy, RVI, Polarization Fraction

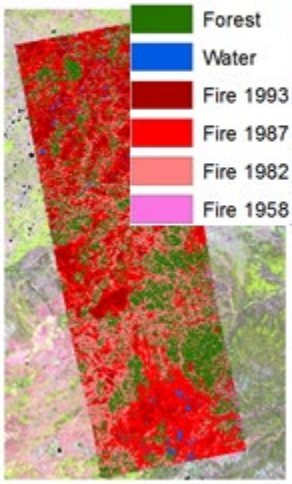

Code	Pixels	Forest	Water	Fire 1993	Fire 1987	Fire 1982	Fire 1958
Forest	1714	73.8	0	0	4.49	20.54	1.17
Water	557	0	100	0	0	0	0
Fire 1993	248	0	0	88.3 1	11.69	0	0
Fire 1987	2632	1.22	0.04	12.2	74.73	11.82	0
Fire 1982	841	19.14	0	0	3.33	76.93	0.59
Fire 1958	1081	36.82	0	0	0.65	7.59	54.95
Average	accuracy	=	78.12	%			
Overall	accuracy	=	74.21	%			

Kappa	Coefficient	=	0.669	
Standard	Deviation	=	0.007	
	Confidence	Level	:	
	99%	0.669	+/-	0.017
	95%	0.669	+/-	0.01291
	90%	0.669	+/-	0.01084

MLC Alpha, Entropy, RVI, RCS Max

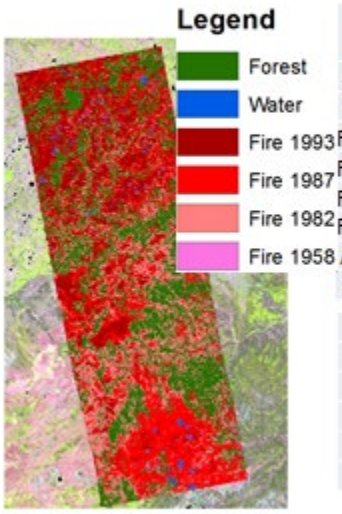

Code		Forest	Water	Fire 1993	Fire 1987	Fire 1982	Fire 1958
Forest	1714	78.82	0	0.47	2.92	16.74	1.05
Water	557	0	100	0	0	0	0
Fire 1993	248	0	0	94.35	5.65	0	0
Fire 1987	2632	2.32	0	9.04	76.03	12.58	0.04
Fire 1982	841	18.07	0	0	4.16	77.76	0
Fire 1958	1081	36.73	0	0	0.09	9.16	54.02
Average accuracy		=	80.17	%			
Overall accuracy		=	76.08	%			

Kappa	Coefficient	=	0.692	
Standard	Deviation	=	0.006	
	Confidence	Level	:	
	99%	0.692	+/-	0.01663
	95%	0.692	+/-	0.01263
	90%	0.692	+/-	0.0106

MLC Alpha, Entropy, RVI, Pedestal Height,

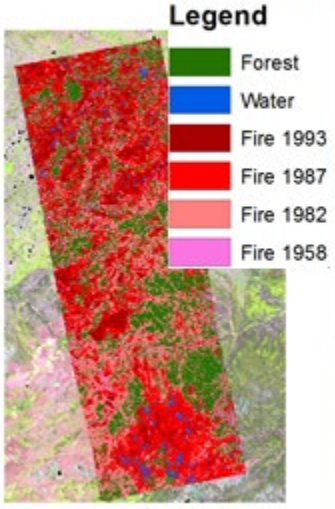

Code	Pixels	Forest	Water	Fire 1993	Fire 1987	Fire 1982	Fire 1958
Forest	1714	71.82	0	0	3.27	22.17	2.74
Water	557	0	99.28	0	0	0	0.72
Fire 1993	248	0	0	87.1	12.9	0	0
Fire 1987	2632	0.99	0.19	17.02	69.22	11.66	0.91
Fire 1982	841	16.41	0	0	4.04	76.93	2.62
Fire 1958	1081	36.73	0	0	0.65	7.31	55.32
Average accuracy		=	76.61	%			
Overall accuracy		=	71.64	%			

Kappa	Coefficient	=	0.64	
Standard	Deviation	=	0.007	
	Confidence	Level	:	
	99%	0.64	+/-	0.01733
	95%	0.64	+/-	0.01316
	90%	0.64	+/-	0.01105

MLC Entropy, Pedestal Height, RCS Max, Polarization Fraction

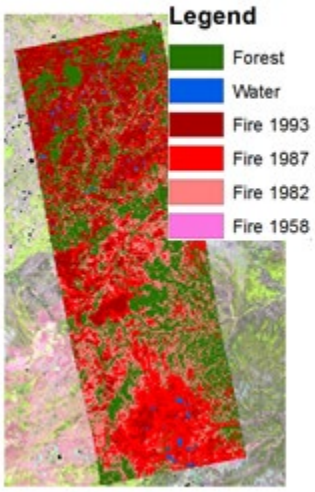

Code	Pixels	Forest	Water	Fire 1993	Fire 1987	Fire 1982	Fire 1958
Forest	1714	75.73	0	0.76	2.16	21.35	0
Water	557	0	100	0	0	0	0
Fire 1993	248	0	0	95.56	4.44	0	0
Fire 1987	2632	0.23	0	12.61	74.16	12.99	0
Fire 1982	841	12.13	0	0	3.8	84.07	0
Fire 1958	1081	27.66	0	0	2.22	16.19	53.93
Average	accuracy	=	80.58	%			
Overall	accuracy	=	75.41	%			

Kappa	Coefficient	=	0.687	
Standard	Deviation	=	0.006	
	Confidence	Level	:	
	99%	0.687	+/-	0.01656
	95%	0.687	+/-	0.01258
	90%	0.687	+/-	0.01056

MLC Alpha, Pedestal Height, RCS Max, Polarization Fraction

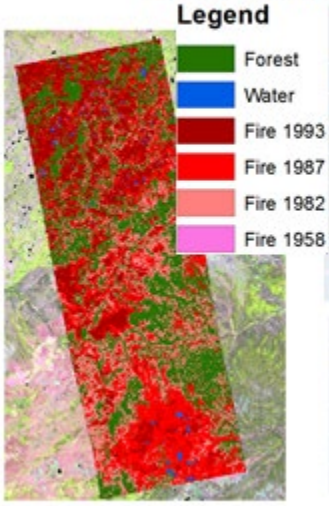

	Pixels	Forest	Water	Fire 1993	Fire 1987	Fire 1982	Fire 1958
Forest	1714	81.97	0	0.82	6.77	10.44	0
Water	557	0	100	0	0	0	0
Fire 1993	248	0	0	95.56	4.44	0	0
Fire 1987	2632	0.11	0	12.16	77.36	10.37	0
Fire 1982	841	11.77	0	0	6.78	81.45	0
Fire 1958	1081	32.56	0	0	0.37	13.14	53.93
Average	accuracy	=	81.71	%			
Overall	accuracy	=	77.8	%			

Kappa	Coefficient	=	0.714	
Standard	Deviation	=	0.006	
	Confidence	Level	:	
	99%	0.714	+/-	0.01622
	95%	0.714	+/-	0.01232
	90%	0.714	+/-	0.01034

Appendix Q. Radarsat-2 Sept. 22 Classification Results

MLC Alpha, Entropy, Lambda 2+3

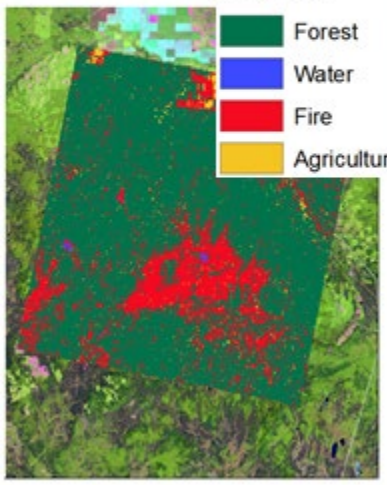

	Pixels	Forest	Water	Fire	Agriculture
Forest	3192	94.45	0	5.01	0.53
Water	2699	0	99.52	0.48	0
Fire	13562	8.06	0	87.65	4.29
Agriculture	14448	3.5	0	11.84	84.66
Average	accuracy	=	91.57	%	
Overall	accuracy	=	87.96	%	

Kappa	Coefficient	=	0.817	
Standard	Deviation	=	0.003	
	Confidence	Level	:	
	99%	0.817	+/-	0.007
	95%	0.817	+/-	0.005
	90%	0.817	+/-	0.004

MLC Alpha, Entropy, Luneburg Anisotropy, Lambda 2+3

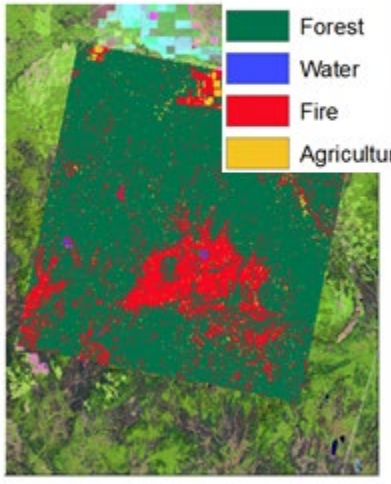

	Pixels	Forest	Water	Fire	Agriculture
Forest	3192	94.89	0	4.42	0.69
Water	2699	0	100	0	0
Fire	13562	8.17	0	87.81	4.02
Agriculture	14448	3.34	0	10.72	85.94
Average	Accuracy	=	92.16	%	
Overall	Accuracy	=	88.65	%	

Kappa	Coefficient	=	0.827	
Standard	Deviation	=	0.003	
	Confidence	Level	:	
	99%	0.827	+/-	0.007
	95%	0.827	+/-	0.005
	90%	0.827	+/-	0.004

MLC Alpha, Entropy, RVI, Luneburg Anisotropy, Lambda 2+3

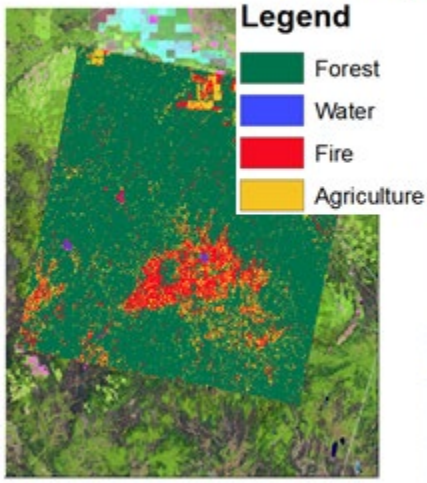

Code	Pixels	Forest	Water	Fire	Agriculture
Forest	3192	95.65	0	0.81	3.54
Water	2699	0	99.89	0.11	0
Fire	13562	11.24	0	49.18	39.57
Agriculture	14448	3.63	0	2.59	93.78
Average	accuracy	=	84.63	%	
Overall	accuracy	=	76.6	%	

Kappa	Coefficient	=	0.644	
Standard	Deviation	=	0.004	
	Confidence	Level	:	
	99%	0.644	+/-	0.009
	95%	0.644	+/-	0.007
	90%	0.644	+/-	0.006

MLC Alpha, Entropy, RVI, Luneburg Anisotropy

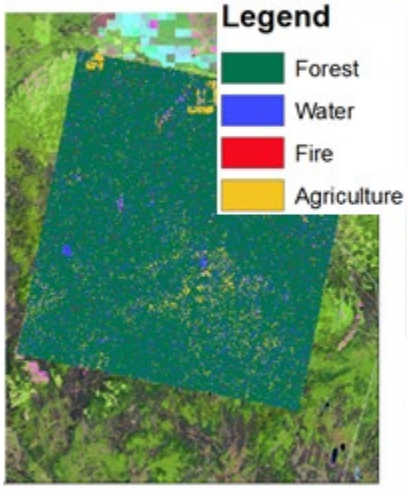

Code	Pixels	Forest	Water	Fire	Agriculture
Forest	3192	84.71	10.15	0.85	4.29
Water	2699	3.3	90.81	0.26	5.63
Fire	13562	51.04	12.46	1.43	35.07
Agriculture	14448	6.8	4.21	0.48	88.52
Average	accuracy	=	66.37	%	
Overall	accuracy	=	53.5	%	

Kappa	Coefficient	=	0.364	
Standard	Deviation	=	0.004	
	Confidence	Level	:	
	99%	0.364	+/-	0.01
	95%	0.364	+/-	0.01
	90%	0.364	+/-	0.01

MLC Alpha, Entropy, Luneburg Anisotropy

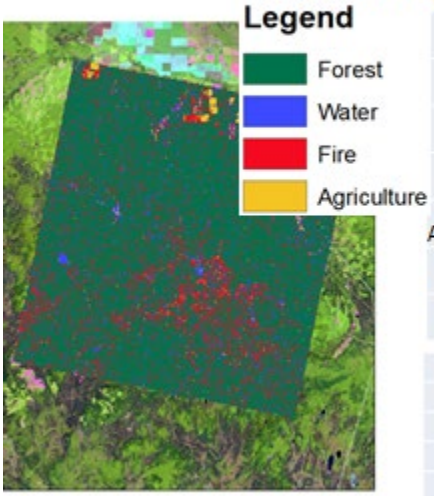

Code	Pixels	Forest	Water	Fire	Agriculture
Forest	3192	77.73	4.54	17.73	0
Water	2699	6.04	87.48	1.22	5.26
Fire	13562	38.79	5.64	51.04	4.53
Agriculture	14448	4.91	3.32	8.46	83.32
Average	accuracy	=	74.89	%	
Overall	accuracy	=	70.21	%	

Kappa	Coefficient	=	0.576	
Standard	Deviation	=	0.003	
	Confidence	Level	:	
	99%	0.576	+/-	0.009
	95%	0.576	+/-	0.007
	90%	0.576	+/-	0.006

MLC Alpha, Entropy, RVI

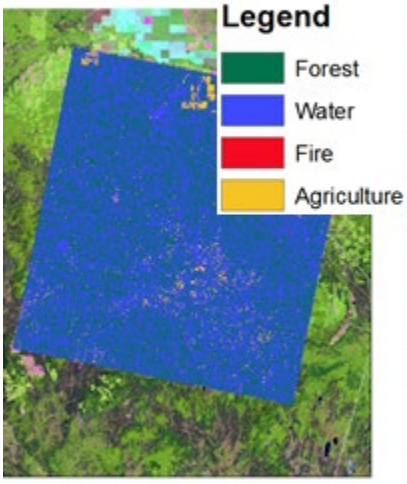

Code	Pixels	Forest	Water	Fire	Agriculture
Forest	3192	39.44	59.02	0.53	1
Water	2699	6.26	87.14	0.07	6.52
Fire	13562	13.97	64.42	0.41	21.19
Agriculture	14448	2.03	11.16	0.44	86.37
Average	accuracy	=	53.34	%	
Overall	accuracy	=	47.63	%	

Kappa	Coefficient	=	0.309	
Standard	Deviation	=	0.004	
	Confidence	Level	:	
	99%	0.309	+/-	0.01
	95%	0.309	+/-	0.01
	90%	0.309	+/-	0.01

MLC Entropy, RVI, Luneburg Anisotropy

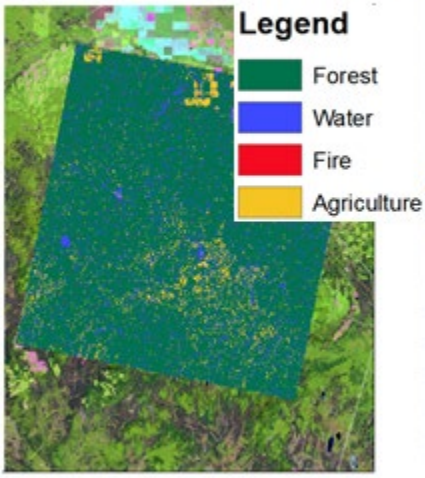

Code	Pixels	Forest	Water	Fire	Agriculture
Forest	3192	84.12	10.31	0.53	5.04
Water	2699	3.37	90.7	0.15	5.78
Fire	13562	49.52	11.87	0.5	38.11
Agriculture	14448	7.14	4.7	0.5	87.66
Average	accuracy	=	65.74	%	
Overall	accuracy	=	52.7	%	

Kappa	Coefficient	=	0.351	
Standard	Deviation	=	0.004	
	Confidence	Level	:	
	99%	0.351	+/-	0.01
	95%	0.351	+/-	0.01
	90%	0.351	+/-	0.01

MLC Alpha, RVI, Luneburg Anisotropy

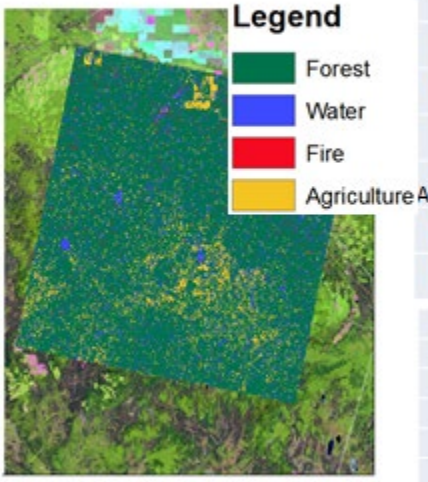

Code	Pixels	Forest	Water	Fire	Agriculture
Forest	3192	79.98	8.65	0.72	10.65
Water	2699	3.52	90.96	0.26	5.26
Fire	13562	47.08	9.68	0.91	42.33
Agriculture	14448	7.12	11.6	0.55	80.73
Average	accuracy	=	63.14	%	
Overall	accuracy	=	49.54	%	

Kappa	Coefficient	=	0.31	
Standard	Deviation	=	0.004	
	Confidence	Level	:	
	99%	0.31	+/-	0.01
	95%	0.31	+/-	0.01
	90%	0.31	+/-	0.01